REPORT DOCUMENTATION PAGE

Form Approved
OMB No. 0704-0188

1. AGENCY USE ONLY (Leave blank)	2. REPORT DATE September 18, 1996	3. REPORT TYPE AND DATES COVERED Final Technical Report 01Oct92-30Sept95

4. TITLE AND SUBTITLE
Novel Materials and Devices From Self-Assembled Periodic Structures

5. FUNDING NUMBERS
F49620-93-1-0008

Hugh C. De Long, Capt.

6110ᒏF
2303/BS

6. AUTHOR(S)
Sanford A. Asher

7. PERFORMING ORGANIZATION NAME(S) AND ADDRESS(ES)
University of Pittsburgh
Department of Chemistry
Pittsburgh, PA 15260

8. PERFORMING ORGANIZATION
AFOSR-TR-96

0478

9. SPONSORING/MONITORING AGENCY NAME(S) AND ADDRESS(ES)
AFOSR/NL
110 Duncan Avenue Suite B115
Bolling AFB, DC 20332-0001

CAPT Hugh C. De Long

AGENCY REPORT NUMBER

19961015 010

11. SUPPLEMENTARY NOTES

12a. DISTRIBUTION/AVAILABILITY STATEMENT

12b. DISTRIBUTION CODE

13. ABSTRACT (Maximum 200 words)

The research program developed novel mesoscopically periodic materials for use in novel optical devices such as optical limiters (OL) and switches. These materials are fabricated using the crystalline colloidal array (CCA) self assembly motif. We developed methods to polymerize CCA into hydrogel matrices to form rugged mesoscopic periodic arrays. We developed novel strategies to incorporate monodisperse CdS quantum dots in monodisperse ca. 100 nm colloidal spheres of SiO_2 to form nonlinear materials for use in OL. This work also resulted in new high surface area porous SiO_2 colloids with voids and chambers which should be useful in applications such as catalysis. We also developed a synthesis of monodisperse polymethylmethacrylate (PMMA) colloids containing covalently bound dye. These colloids form CCA which we polymerized in a hydrogel matrix. We matched the real part of the medium refractive index to that of the PMMA particles to form a periodic array which shows variations only in the imaginary part of the refractive index. We are utilizing this material for optical switching devices.

14. SUBJECT TERMS

15. NUMBER OF PAGES
117

16. PRICE CODE

17. SECURITY CLASSIFICATION OF REPORT	18. SECURITY CLASSIFICATION OF THIS PAGE	19. SECURITY CLASSIFICATION OF ABSTRACT	20. LIMITATION OF ABSTRACT
U	U	U	U

2 5 SEP

Final Technical Report
AIR FORCE OFFICE OF SCIENTIFIC RESEARCH
Grant F49620-93-1-0008

NOVEL MATERIALS AND DEVICES FROM SELF-ASSEMBLED
PERIODIC STRUCTURES

Sanford A. Asher
Department of Chemistry
University of Pittsburgh
Pittsburgh, PA 15260

Final Technical Report
Sanford A. Asher
F49620-93-1-0008

Participants:

Graduate Students

John Holtz
Lei Liu
Shalabh Tandon
Zhijun Wu

Postdoctral Students

Seshadri Jagannathan
Rasu Kesavamoorthy
Song-yuan Chang
Albert Tse

Publications:

1. "Self-Assembly and Ordering of Electrostatically Stabilized Silica Suspensions",
   R. Kesavamoorthy, S. Tandon, S. Xu, S. Jagannathan, and S. A. Asher, J. Coll. Int. Sci. <u>153</u>, 188-198 (1992).
2. "Self Assembly Motif for Creating Submicron Periodic Materials. Polymerized Crystalline Colloidal Arrays",
   S. A. Asher, J. Holtz, L. Liu, and Z. Wu, J. Am. Chem. Soc. <u>116</u>, 4997-4998 (1994).
3. "Preparation and Properties of Tailored Morphology, Monodisperse Colloidal Silica-Cadmium Sulfide Nanocomposites",
   S.-Y. Chang, L. Liu, and S. A. Asher, J. Am. Chem. Soc. <u>116</u>, 6739-6744 (1994).
4. "Preparation and Processing of Monodisperse Colloidal Silica-Cadmium Sulfide Nano-composites",
   S.-Y. Chang, L. Liu, and S. A. Asher, Mat. Res. Soc. Symp. Proc. Vol. 346, 875-880 (1994).
5. "Creation of Templated Complex Topological Morphologies in Colloidal Silica",
   S.-Y. Chang, L. Liu, and S. A. Asher, J. Am. Chem. Soc. <u>116</u>, 6745-6747 (1994).
6. "Synthesis of Dyed Monodisperse Poly(methyl methacrylate) Colloids for the Preparation of Submicron Periodic Light Absorbing Arrays",
   A. Tse, Z. Wu, and S. A. Asher, Macromolecules <u>28</u>, 6533-6538 (1995).

Table of Contents

List of Tables

List of Figures

1.0 Introduction

This report discusses the development of novel enabling materials for use in optical devices, based on self-assembling arrays of colloidal particles called crystalline colloidal arrays (CCA)[1-3]. These spherical particles self assemble into body centered cubic (BCC), or face centered cubic (FCC) arrays depending on the colloid properties and concentration (Figure 1.1)[2,3]. The spheres are highly charged due to ionizable surface groups. The charge may be positive or negative, depending on the nature of the surface ionizable groups. Counterions screen the Coulombic repulsive interactions, but at high sphere concentrations and low ionic impurity concentrations, sufficient repulsive interactions are present to cause the array to self-assemble [2-5].

The CCA diffracts wavelengths of light that meet the Bragg condition, but freely transmits other wavelengths. The attenuation of light meeting the Bragg condition can be close to 100% for a few hundred micron thick crystal [1-6]. The magnitude of attenuation of light meeting the Bragg condition depends upon the sphere diameter and the refractive index mismatch between the sphere and the suspending medium [2-5]. The wavelength diffracted can be continuously tuned between the near UV and the near IR by changing the colloid concentration.

The colloids comprising the array may be made from a variety of organic or inorganic polymers such as polystyrene, poly(methylmethacrylate), polyN-isopropylacrylamide, polyfluorinated materials, and silica. The optical properties of the

Crystalline Colloidal Arrays
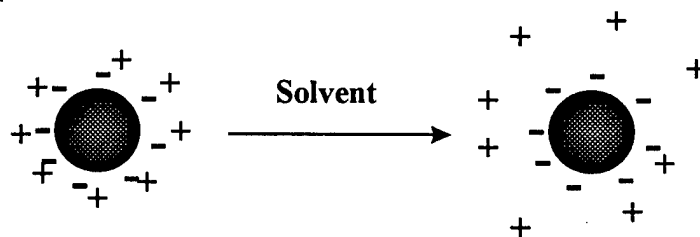
1. Ionization of surface charges on the colloidal particles.
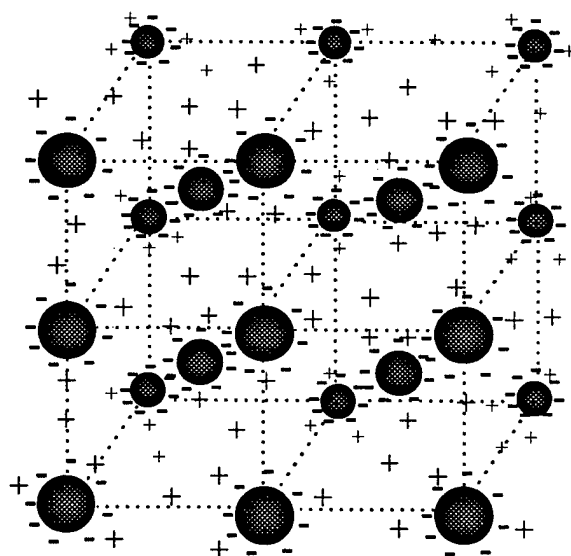
2. Particles self-assemble into 3-D ordered arrays.

Figure 1.1 Crystalline Colloidal Array

array can be tailored to a specific application by changing the suspending medium and the colloid composition.

The liquid CCA can be disordered by thermal and physical shocks, as well as ionic impurities, which screen the repulsive interaction [2-5]. We developed a method to polymerize the CCA in a hydrogel matrix to make it impervious to ionic impurities and thermal or physical shocks [6].

The ability of the CCA to reject a narrow wavelength band and pass the rest of the spectrum makes them ideal for use as notch filters and other optical devices. The present report describes the work to fabricate novel colloidal materials for use in CCA based optical limiters, notch filters, and non-linear optical devices. The purpose of the work under this contract was to prepare self-assembling, highly charged colloidal particles from a variety of materials suitable for use in optical devices, to study the self assembly process of the CCA, and to develop a methodology for locking those arrays in a hydrogel matrix without increasing the diffraction bandwidth, or decreasing the diffraction intensity, of the CCA.

This report is a summary of our progress toward these goals. Chapter 2 describes our studies of the self-assembly process of highly charged silica spheres, which we synthesized using a modification of the Stöber process.

Chapter 3 describes the synthesis of highly charged, monodisperse silica colloids (*ca.* 40 - 300 nm diameter) containing CdS quantum dots (*ca.* 2.4 nm diameter). Careful control in real time of the synthesis procedure permitted the creation of nanocomposites containing complex CdS nanoscale morphologies in the mesoscale silica colloids. TEM

and SEM micrographs show that the CdS was present as a homogenous dispersion of small quantum dots in the larger silica particle ("raisin bread" morphology), or as large inclusions, surface caps, the central core of a silica particle, or layered shells of CdS between layered shells of silica. These silica particles with the CdS quantum dot inclusions show some potential as a non-linear optical material.

Chapter 4 describes further processing of the CdS / silica nanocomposites to form colloidal silica particles with complex morphologies. After fabrication of the CdS /silica nanocomposite, the CdS inclusions were etched away with strong acid, leaving voids in the silica particles. The etched silica particles have 2.4 nm spherical voids, hollow cores, or layers of concentric shells, depending upon the morphology of the parent nanocomposite. These high surface area particles may be of use as catalytic supports.

Chapter 5 describes the incorporation of a CCA into a hydrogel matrix. Monomers and crosslinkers are dissolved into the fluid CCA and photopolymerized to yield a complex composite network with a mesoscale periodicity. The polymerization process can be controlled so that the diffraction efficiency is only minimally affected by the formation of the network.

Chapter 6 details the preparation of dyed monodisperse Poly(methyl methacrylate) (PMMA) colloids. The dyed spheres were then locked in the hydrogel matrix described in chapter 4. The solvent in the gel was indexed matched to the refractive index of PMMA, leaving a periodic array of absorbers. The body centered cubic array of absorbers interacted with incident electromagnetic radiation with little or no absorption or scattering

of the incident light. This array of absorbers may be useful in non-linear switching and limiting applications.

Chapter 7 summarizes the work detailed in this report and details some of the possible applications of these materials. The technology described in this report has numerous applications in optical device fabrication, catalysis, and display device fabrication.

1.1 References.

1. S.A. Asher, Crystalline Colloidal Array Filters, U.S. Patents # 4,627,689 and 4,632,517, **1986.**

2. Carlson, R.; Asher, S. *Appl. Spectrosc.* **1984,** 38, 297.

3. Spry, R.; and Kosan, D. *Appl. Spectrosc.* **1986**, 40, 782.

4. Flaugh, P.L.; O'Donnell, S.E.; Asher, S.A. *Appl. Spectrosc.* **1984**, 38, 847.

5. Asher, S.A.; Flaugh, P.L.; Washinger, G.; Spectroscopy, **1986**, 1, 26.

6. Asher, S. A.; Holtz, J.; Liu, L.; Wu, Z. J. Am. Chem. Soc. **1994**, 116, 4997.

2.0 Self Assembly and Ordering of Electrostatically Stabilized Silica Suspensions

2.1 Executive Summary

We use optical attenuation spectral measurements and diffraction measurements to examine the structural time evolution of aqueous suspensions of negatively charged colloidal silica particles in a thin quartz cell. The ionic strength in the suspension is monotonically decreased in time by ion-exchange resin. At high ionic strengths, two-dimensional hexagonal order nucleates near the surface of the cell walls while the regions away from the walls show liquid like order. At lower ionic strengths, regions near the wall show three-dimensional order while the interior region shows two-dimensional crystalline order. At the lowest ionic strengths, the entire suspension shows three-dimensional crystalline order.

2.2 Introduction

Concentrated colloidal suspensions show colloidal particle ordering which resembles the gas, liquid, glass and crystalline phases of atomic and molecular systems [1,2,3,4,5]. Colloidal silica particles can acquire a net negative charge when dispersed in water due to the ionization of the surface hydroxyl or other functional groups [6]. The resultant repulsive interactions[7] between the negatively charged particles depend on the particle surface charge, the particle concentration, the impurity concentration, the temperature and the medium dielectric constant [8,9,10]. Depending on the extent of the interparticle interactions, these suspensions will self-assemble into gas, liquid, crystalline and glass phases [1,2,3,4].

The long range ordering of these suspensions is also influenced by the walls of the container[11,12,13,14,15]. The self assembly of colloidal crystalline suspensions orients the highest density planes parallel to the walls of the container (the BCC (110) or FCC (111) planes)[16]. This phenomenon

can be used to orient and form single crystal colloidal arrays for use as narrow band optical rejection filters[4,17]. The orientation of colloidal crystalline suspensions is likely to be sensitive to various properties of the container walls; for example, it was recently suggested that the formation of an image charge in the wall is energetically of major importance for orientation of colloidal suspensions [12,13].

The time evolution of the ordering proceeds by the way of many intermediate steps, as has been recently demonstrated by the Kossel ring pattern analysis by Sogami and Yoshiyama [15]. They concluded that ordering of the monodisperse colloidal suspension contained in a quartz cell evolved from two-dimensional (2-D) hcp structure to normal FCC structure (volume fraction, $N > 2\%$) or normal BCC structure ($N < 2\%$) through many intermediate steps. Clark et al [11] investigated shear induced melting of colloidal crystals ($N \sim 1\%$) and subsequent reordering on removing the shear. They reported that 2-D HCP layer array structure precedes the formation of the ultimate BCC structure.

The structure, orientation and the lattice parameters of ordered colloidal crystalline suspensions can be determined by laser diffraction [18,19,20] or Kossel-ring analysis [11,14,15,16,21,22,23]. If the crystal contains numerous defects, Kossel-ring and diffraction spots may not be sharp enough to characterize the crystal structure. These defects, which often arise during the transition from the liquid to the crystal phase [9,24,25,26,27] may necessitate the use of additional techniques to determine the crystal structure, orientation and lattice parameters. Optical Attenuation Spectroscopy has been used to investigate the ordering in colloidal crystals.[8,22,28] We demonstrate here that angle dependent Optical Attenuation Spectroscopy can be easily used to characterize crystal structure even for crystals with numerous defects.

We examine the structural evolution of an aqueous suspension of negatively charged silica

particles in a thin quartz cell using Optical Attenuation Spectroscopy and diffraction measurements. The diffraction pattern of the suspension indicates liquid-like order at high ionic strength. The regions near the walls of the container appear to be liquid-like while the regions away from the surface appear gas-like (complete disorder). As the ionic strength of suspension is decreased by the use of ion-exchange resin, 2-D crystalline order develops near the walls, while liquid-like order is observed in regions away from the walls. Upon further deionization, the suspension shows three-dimensional crystalline order near the walls while regions away from the wall show 2-D order. We demonstrate that the structure, orientation and the lattice parameter of poorly ordered colloidal suspensions can be unambiguously determined using angle resolved Optical Attenuation Spectroscopy in conjunction with laser diffraction.

2.3 Experimental

Colloidal silica particles (145-250 nm in diameter) were synthesized using a modified Stöber process ([29,30]). Spectroscopic grade ammonium hydroxide (29.2% Mallinckrodt), tetraethyl orthosilicate (Petrarch) and 2-(4-chlorosulfonylphenyl)-ethyltrimethoxysilane (Petrarch) were used as supplied. The concentration of ammonia was determined by titration with standardized HCl solution, using methyl red as the indicator. A typical experimental procedure is: 44.2 ml of water (24.43M), 15.5 ml of 14.10M ammonium hydroxide (1.75 M) and 58.0 ml of methanol (11.57M) are mixed in a clean, dry 250 ml Erlenmeyer flask. The mixture is sonicated using an ultrasonic bath as 7.5 ml of tetraethyl orthosilicate (TEOS, 0.29M) is added rapidly to the flask. The reaction mixture shows opalescence about a minute after the addition of TEOS, indicating the initiation of the precipitation reaction. The reaction mixture is vigorously stirred for about 12 hours yielding a turbid suspension of colloidal silica. To remove excess TEOS, the suspension was washed with methanol at least three

times and redispersed in 20 ml of methanol. These silica particles were functionalized using 2-(4-chlorosulfonylphenyl)-ethyltrimethoxysilane (CETS) according to the following procedure. A 20 ml alcoholic solution of CETS (1/20:v/v) is added to the silica suspension and stirred vigorously for *ca.* 4 hours. The resulting suspension was centrifuged, washed with methanol several times and redispersed in deionized water. The suspension was then dialyzed for at least three days against deionized water containing mixed bed ion-exchange resin using 50,000 MWCO Spectra/Por 6 dialysis tubing (Fisher); the water was changed every 24 hrs. Finally, the suspension was mixed with ion-exchange resin and gently agitated for 48 hrs using a mechanical shaker.

The particle diameter was determined by quasi-elastic light scattering (QELS, Langley Ford 1096) and by transmission electron microscopy (TEM). The particle size obtained from these two methods agreed to within ~3%; the monodispersity in size was also better than ~3%. We utilized 245 nm and 140 nm particles in the present study. The concentration (n_p) of silica particles was measured by gravimetry (19) by assuming the density of silica to be 2.1 (6).

The laser diffraction measurements were made on suspensions contained in a quartz cell, (2.5 X 2.5 X .01 cm^3) mounted on a calibrated rotation stage. The incidence angles (in air) were measured relative to the cell surface normal; i.e. the angle of incidence is defined as 0° when the cell plane normal is parallel to the incident beam direction. The angle measurements are accurate to ±0.5°. The angles in the crystal were calculated from the measured angles (in air) using Snell's law. The diffraction angles were measured by rotating the detector about a vertical axis passing through the cell. The diffracted angle was also measured in some cases by placing a screen in the path of the forward diffracted beams (plane of the screen being perpendicular to the transmitted beam) and measuring the

distance between the transmitted and diffracted spots on the screen. Laser excitation was obtained using argon ion and He-Ne lasers.

The optical attenuation spectra were recorded using a Perkin Elmer Lambda 9 UV/VIS/NIR spectrophotometer. A rotating stage was placed in the sample compartment of the spectrometer and the quartz cell was mounted such that the beam was focussed onto the center of the suspension. The cell was rotated about the vertical axis from the normal incidence (0°). The refractive index, n, of the suspension was measured using a temperature controlled Abbe' refractometer (Bausch and Lomb).

2.4 Results and Discussion
Structural evolution of a 245 nm silica particle suspension:

The silica suspension (n_p=1.67 x 10^{12}/ cm^3, n=1.338) was introduced into a quartz cell, and the suspension in the cell was in contact with a reservoir of mixed bed ion-exchange resin. The suspension initially showed iridescence under white light illumination. When illuminated by the 514.5 nm beam of argon-ion laser at normal incidence, intense forward scattering (a Debye Scherrer ring) was observed at a small angle (θ_2) centered around the incident beam (Figure 2.1a). Speckle fluctuations (*ca.* 0.5 sec) were observed in this broad halo (Figure 2.1b).

Debye Scherrer ring diffraction from colloidal suspensions having liquid-like order is well known [31,32,33]. However, Debye Scherrer rings [34] are also observed for polycrystalline colloids as well as randomly stacked 2-D colloidal crystals [35]. Thus, the broad diffuse ring observed for our suspension could derive from any of these three structures. However, the particle motion in liquid structures will be larger than that in the polycrystalline or the 2-D random stacked structures. Speckle fluctuation results from particle movement, and fast fluctuations results from fast particle movement. The observed
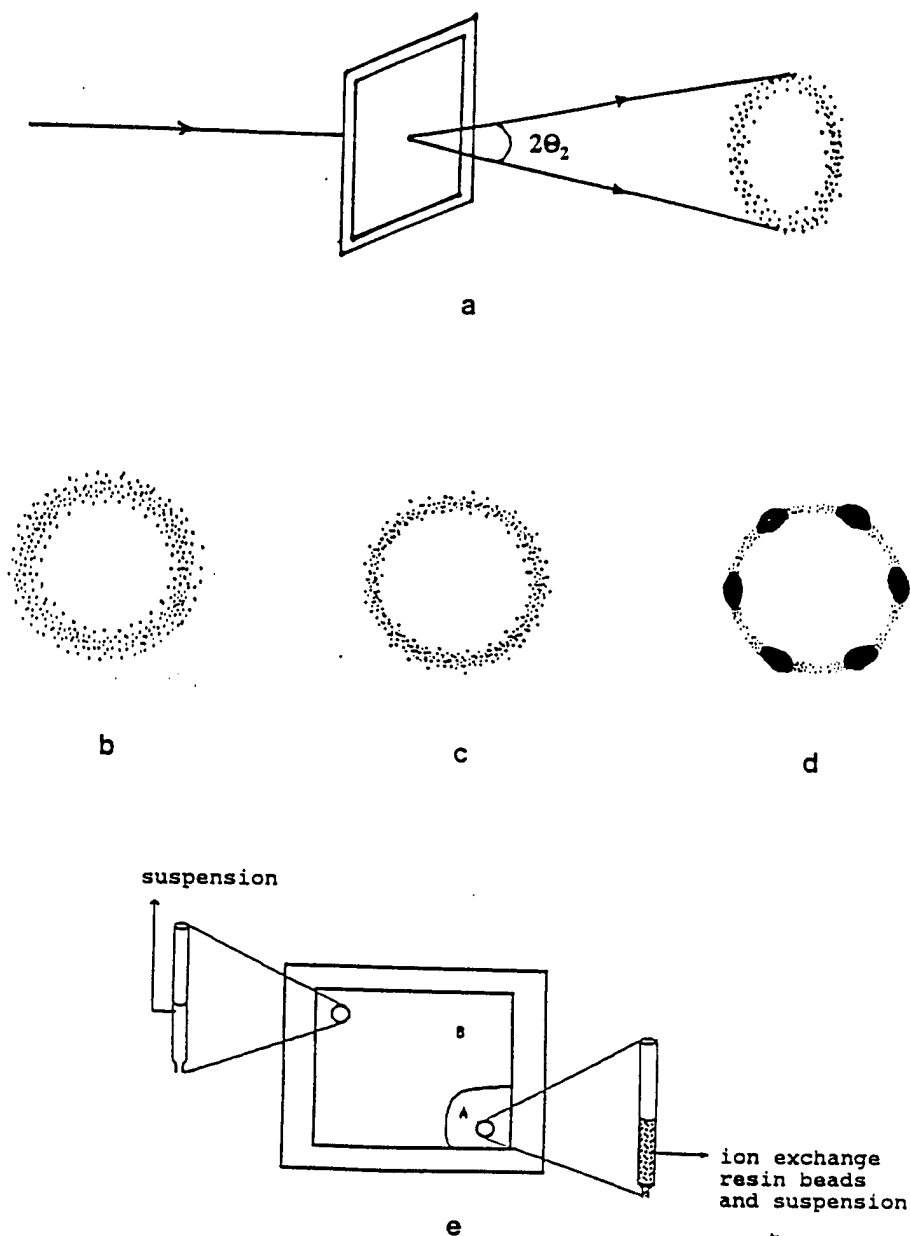
Figure 2.1   The scattered intensity pattern of the 245 nm silica particle suspension with $n_p = 1.67 \times 10^{12} / cm^3$ for $\theta = 0°$ and $\lambda = 514.5$ nm. (a) Schematic representation of the optical geometry. (b) One hr, (c) 6 hr., (d) 2 days after cell preparation. (e) Schematic representation of the cell, showing regions A and B.

speckle fluctuation in the broad diffuse ring which was rapid (periodicity ≈ 0.5 sec), slowed down and eventually disappeared after one day due to an increased structural ordering. It is likely that the initial broad diffuse ring was produced by liquid-like ordering.

The scattering wavevector, q, is given by Eq. [2.1]

$$q = \frac{4\pi n}{\lambda} \sin\left(\frac{\left(\theta_2^{xtl}\right)}{2}\right) \quad [2.1]$$

where θ_2^{xtl} is the diffraction angle in the crystal which is obtained from θ_2 using Snell's law. The diffracted intensity from a liquid-like order is maximum for a value of q which is close to that for the first allowed reciprocal lattice vector present when the liquid freezes into a crystalline order [32]. Using the experimental value of q and assuming an FCC structure, we calculate a particle concentration (n_p) of $4.7 \times 10^{12}/cm^3$ ($n_p = 4/a^3$, $a = \sqrt{3}d$, and d is the (111) interplanar spacing). If the liquid crystallized into a BCC lattice, the calculated n_p would be 8% lower. In either case, this calculated particle concentration is three-fold larger than that measured by gravimetry ($1.67 \times 10^{12}/cm^3$). This discrepancy in the particle concentration obtained from the two techniques (gravimetry and diffraction) indicates a large inhomogeneity in particle concentration. The region that dominates the diffraction must have the high particle concentration. By conservation of particle number only a small portion of the sample can show this concentration enrichment. Thus, it is likely that the diffraction observed is dominated by a thin (< 1 μm) film of liquid-like ordered colloids at the wall (*vide infra*). For example, we can easily observe diffraction from the thin films of ordered colloid which coat the walls of a sample vial containing a crystalline colloid.

Kesavamoorthy *et al* ,[12,13] in a previous study of colloidal polystyrene suspensions using optical microscopy, observed an increased particle concentration and an increased particle ordering near the

walls of the container compared to the cell interior. They attributed this particle concentration increase to the presence of an attractive potential at the container walls due to image charges induced by the charged colloidal particles on the container walls. The attraction of the colloidal particles by the image charge would result in an increased concentration of the particles adjacent to the walls. Our diffraction measurements indicate that this region of increased particle concentration initially has a liquid-like order. Since a decreased ordering of colloidal suspensions accompanies a particle concentration decrease, we expect that the lowered particle concentration in the cell interior is correlated with a non diffracting gas-like disorder.

As the suspension ionic impurity concentration decreased (due to the presence of ion-exchange resin), the width of the ring decreased (Figure 2.1c) and the speckle fluctuation slowed down (*ca.* 3 sec). One day after filling the cell a six-fold pattern of bright spots was observed (superimposed on the diffuse ring). The six-fold pattern was not sharp but was spread over a *ca.* 10° width along the ring as shown in Figure 2.1d. The pattern did not show speckle fluctuation.

This pattern of spots indicates the existence of a 2-D hexagonal array of particles [15,18,35,36] in which the hexagonal 2-D arrays randomly stack in the third dimension with no correlation between the position of a particle in one layer and that in an adjacent layer.[15] This 2-D hexagonal array stacking was previously observed in the structural evolution of colloidal suspensions by Sogami and Yoshiyama [15]. We did not observe any diffraction spots which could derive from three-dimensional crystalline structure. [19,21,35] The six-fold pattern when the incident beam was translated across the cell surface, confirming the existence of 2-D crystalline order along the entire cell surface. Table 2.1 lists the measured diffraction angles of the circular rings and the six-fold pattern as well as the average

interparticle separation distance (D) calculated using the 2-D Bragg diffraction equation 18

$$D=\frac{2\lambda}{\sqrt{3}\left(\sin\theta_1 +\sin\theta_2\right)} \quad \textbf{[2.2]}$$

where λ is the incident wavelength, θ_1 is the incidence angle ($\theta_1=0°$) and θ_2 is the measured diffraction angle. Table 2.1 also lists the interparticle spacing calculated using Eq. [2.2] and the gravimetrically determined particle concentration for both a FCC and BCC structure.

The value of D (670 nm) obtained from Eq. [2.2] corresponds to a particle concentration of $4.7 \times 10^{12}/cm^3$, which is identical to that calculated from the diffuse Debye-Scherrer type rings. It, thus, appears that the original liquid-like film at the wall crystallizes into a 2-D crystal.

Three days after filling the cell the suspension became inhomogeneous and iridescence of the region close to the ion-exchange reservoir (region A) differed in color from the rest of the cell (region B, Figure 2.1e). The interparticle spacing (D) was calculated from the 2-D diffraction patterns (Eq. [2.2]) to be 948 nm in region A and 812 nm in region B. These values of D (948 nm, 812 nm) are larger than the values of 670 nm obtained one day after filling the cell. This D value increase could be due to the increased interparticle repulsive interactions at reduced n_i. The interparticle spacing in region A (948 nm) represents the spacing expected for a FCC crystal with the expected average originally present in the dispersion having a particle concentration of $1.67 \times 10^{12}/cm^3$ and indicates that similar particle concentrations occur near the wall and the interior in region A in a structure where the 2-D hexagonal layers randomly stack. In region B, the particle concentration calculated from the measured values of D is $2.6 \times 10^{12}/cm^3$, which is greater than the average particle concentration, but is less than that present when the 2-D crystal just-forms ($4.7 \times 10^{12}/cm^3$). Thus, the particle

Table 2.1

The measured diffraction angles from the suspension of 245 nm silica particles ($n_p = 1.67 \times 10^{12}/$ cm^3) and the calculated interparticle separation distance (D = 2 λ/(√3(sin θ$_1$ + sin θ$_2$)) over a period of 9 days. λ = 514.5 nm and θ$_1$ = 0°.

Time elapsed (days)	θ$_2$			D(nm)			structure
	homogeneous	region A	region B	homogeneous	region A	region B	
1 hr	56.2*						*liquid-like
6 hrs	62.4+			670			2-D
1	54			734			2-D
3		38.8	47		948	812	2-D
4		41.4	54.4		898	731	2-D
5		58	65.8		700	651	2-D
8	63.5+			664			2-D
9	57.4*						*liquid-like

*fast speckle fluctuation
+slow speckle fluctuation
2-D = two-dimensional
D in the (111) plane of a FCC crystal = 946 nm
D in the (110) plane of a BCC crystal = 920 nm

concentration near the wall remains higher than the interior, but the concentration gradient decreases as the ordering increases. The better ordering of region A presumably derives from the lower ionic strength present due to the proximity of region A to the ion exchange resin.

The optical attenuation spectra at normal incidence from the two regions (A and B) did not show sharp peaks, indicating the absence of 3-D crystalline order. Table I lists the interparticle spacing (D) in the two regions at various times after filling the cell. The "diffraction observed" interparticle spacing initially increases in the period between 6 hours and three days of filling the sample. This initial increase probably results from a decreasing ionic strength which results in increased interparticle repulsion. In addition, the thickness of the ordered film may increase. After day three the "diffraction observed" interparticle spacing decreases, probably due to an increased ionic strength as the ion exchange resin is exhausted and the ionic impurity content of the suspension rises.

Structural characterization of the 140 nm silica particle suspension:

A quartz cell filled with 140 nm silica particle suspension (n_p= 1.43 X 10^{13}/cm³, n=1.339) showed iridescence under white light illumination and a six-fold diffraction pattern similar to that of Figure 2.1d. Figure 2.2 shows the optical attenuation spectrum of the silica suspension at normal incidence, where a well defined diffraction peak was absent but the attenuation increased rapidly for θ < 510 nm. For diffraction from a 2-D crystal, with excitation at normal incidence [18]

$$\lambda = \frac{\sqrt{3}}{2} nD \sin\theta_2^{xtl} \quad [2.3]$$

For λ greater than a critical value (λ_c = √3nD/2), no Bragg diffraction occurs. However, for $\lambda < \lambda_c$,
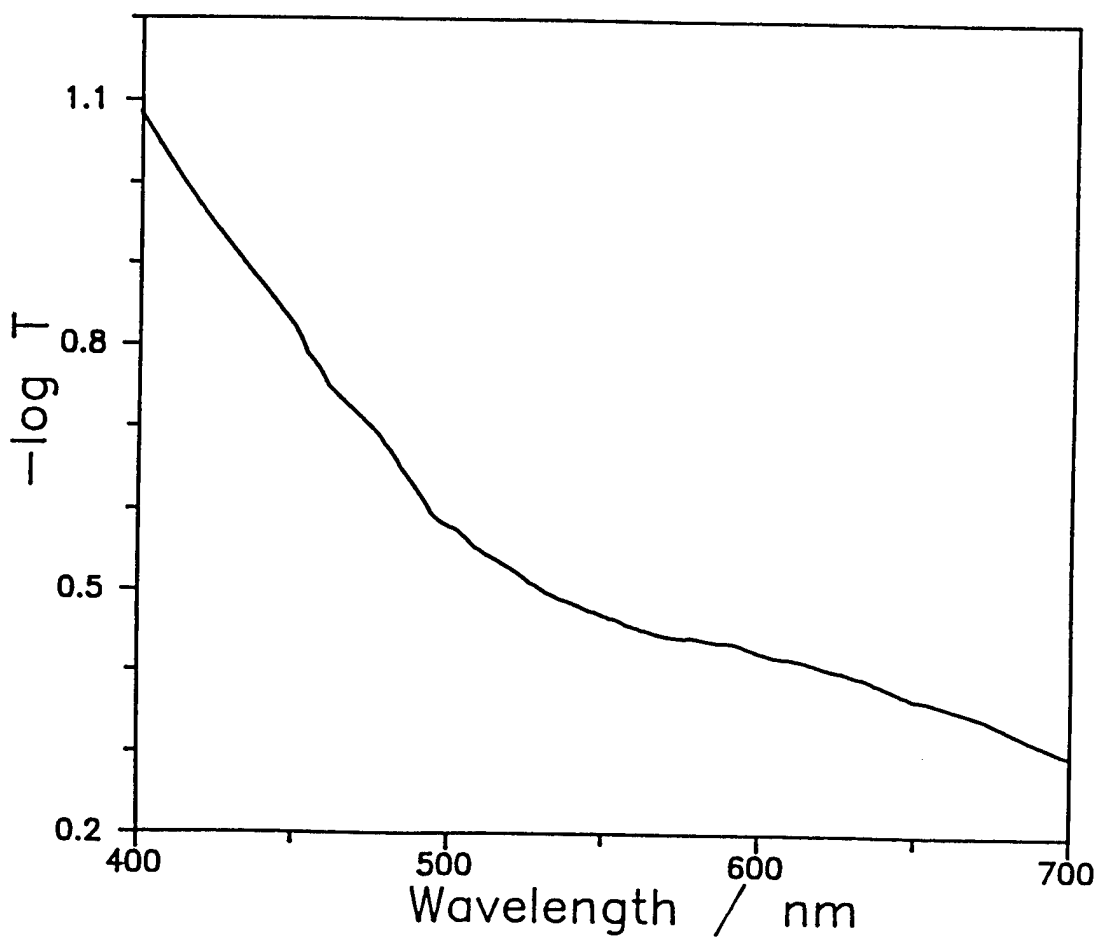
Figure 2.2   The optical attenuation spectrum of the 140 nm silica particle suspension *ca.* 1 hr. after cell preparation, $n_p = 1.43 \times 10^{13}$ / cm^3 and $\theta = 0°$. T is transmittance.

light is two-dimensionally Bragg diffracted away from the incident beam. λ_c is obtained from Figure 2.2 by intersecting the straight lines passing through high and low λ regions of the optical attenuation spectrum. λ_c is determined to be 510 nm, which gives a D value of 439 nm corresponding to a particle concentration of $1.67 \times 10^{13}/$ cm^3, slightly higher than the value ($1.43 \times 10^{13}/$ cm^3) determined by gravimetry. This result is consistent with the behavior of the 245 nm particle suspension discussed above. Thus, we observe for the 140 nm suspension that the region nearest the wall has the highest particle concentration, and is ordered into random stacked 2-D hexagonal layers.

After three days, the diffraction measurements showed a single Bragg diffraction spot (Figure 2.3a). The diffracted spot was spread over a solid angle of *ca.* 0.04 steradians around the Bragg angle of 71° (θ) for 488 nm incident radiation (see Figure 2.3a). When the angle of incidence (θ_i) was changed to 42°, a bright, diffuse elliptical spot was seen for forward diffraction (Figure 2.3b) at $\theta_2 = 33.5°$ (angles measured in air). Upon translating the cell parallel to its face, θ_2 remained constant but the width of the diffraction spot changed. The intensity of the spot decreased as θ_i was varied away from 42°. Table 2.2 lists the angles measured for several excitation wavelengths along with the interparticle spacing (D) calculated using Eq. [2.2] and the interplanar spacing (d) calculated using [4]

$$d = \frac{m\lambda}{2n\sin\phi^{xtl}} \quad [2.4]$$

where n is the refractive index of the suspension, θ^{xtl} is the Bragg angle for diffraction from a 3-D lattice and m is the order of diffraction. Optical attenuation spectra of this suspension (Figures 2.4 and 2.5; discussed in the next section) show peaks corresponding to different sets of planes indicating the formation of 3-D crystal structure. The value of D listed in Table 2.2 corresponds to the particle
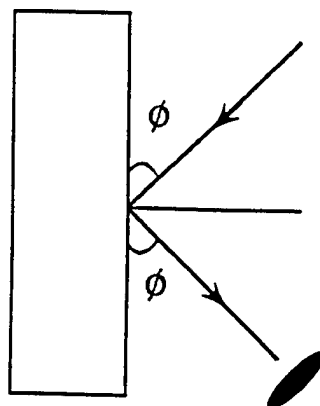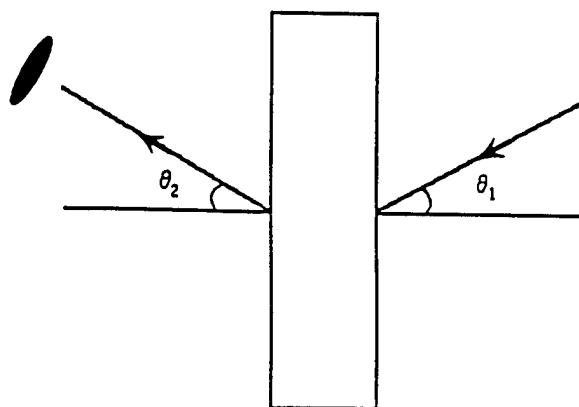
Figure 2.3   A schematic representation of the diffraction measurements. (a)
Diffraction from a three-dimensional crystal in the reflection geometry.
(b) Diffraction from a two-dimensional crystal showing forward
diffraction.

Table 2.2

The measured angles of diffraction, ϕ, θ_1, θ_2, in the suspension of 140 nm silica particles with $n_p = 1.43 \times 10^{13}/$ cm^3 for different wavelengths (λ) and the calculated interplanar separation (d = $(2\lambda/(2n\sin\phi^{xt1}))$) and interparticle separation distance (D = $2\lambda/(\sqrt{3}(\sin\theta_1 + \sin\theta_2))$).

λ	ϕ	θ_1	θ_2	d	D	d/D experimental
457.9	56	38.5	29.5	376	474	0.8
476.5	63	41	31.5	378	468	0.808
488	71	42	33.5	375.4	462	0.812
514.5	87	44.5	34	384	472	0.813

d/D, expected for FCC = 0.816, for BCC = 0.793

28
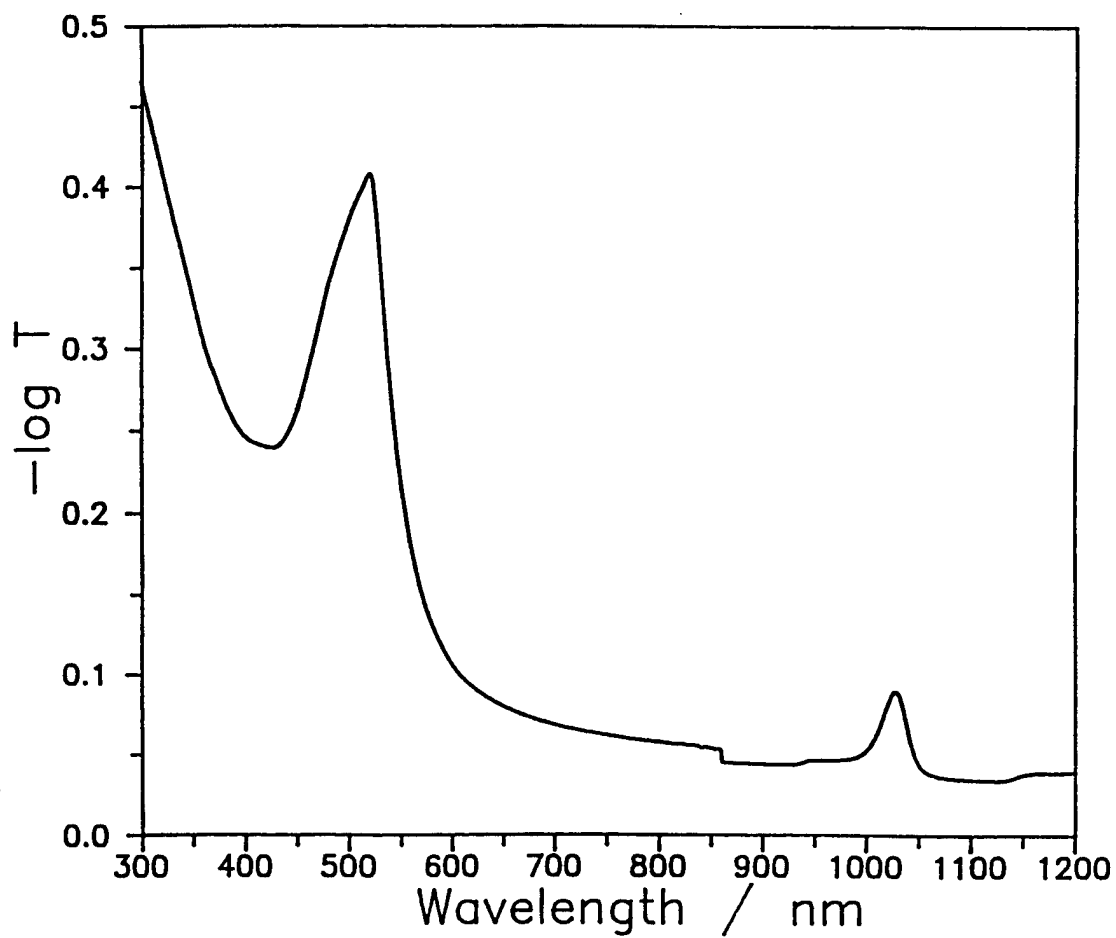
Figure 2.4   The optical attenuation spectrum of the 140 nm silica particle suspension with $n_p = 1.43 \times 10^{13}$ / cm^3 and $\theta = 0°$, three days after cell preparation. T is transmittance.
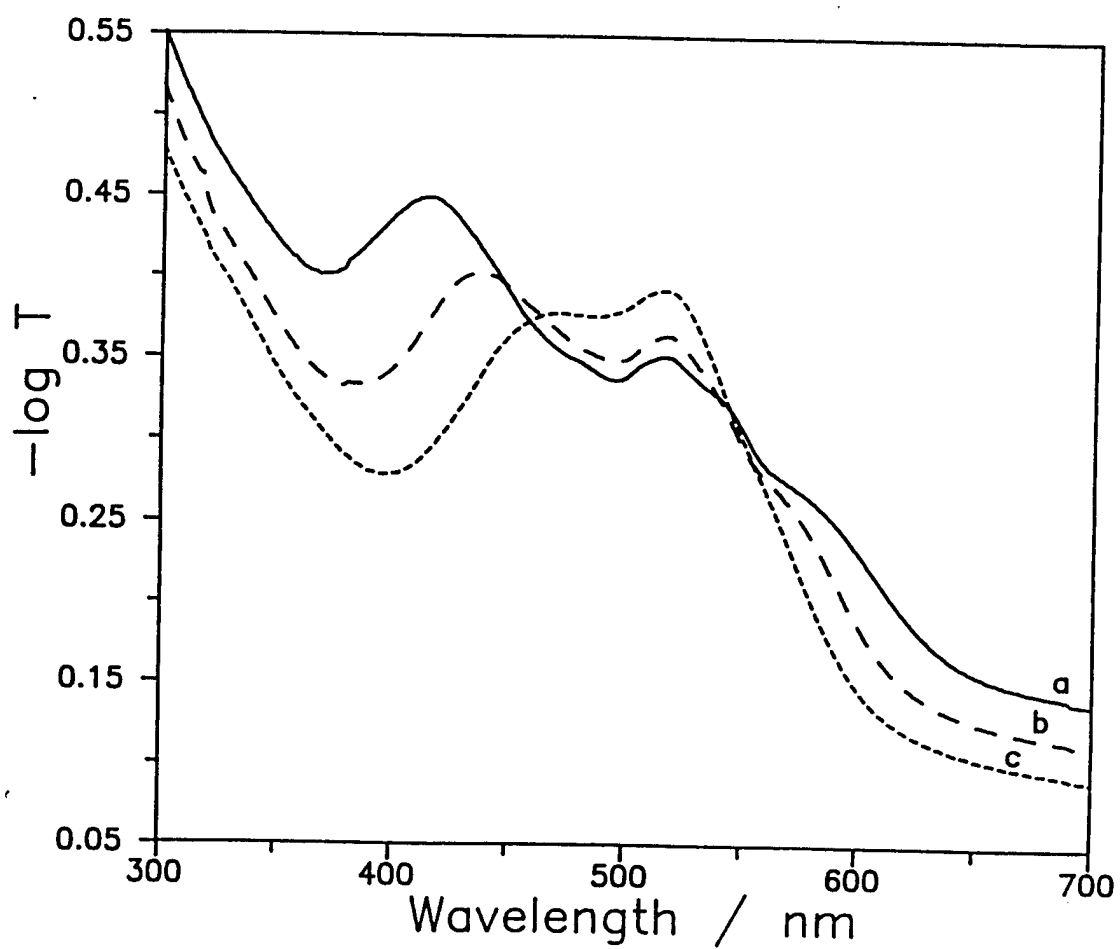
Figure 2.5   The optical attenuation spectrum of the 140 nm silica particle suspension
with $n_p = 1.43 \times 10^{13}$ / cm^3: (a) $\theta = 8°$ (b) $\theta = 6°$ (c) $\theta = 4°$. T is
transmittance.

concentration of *ca.* 1.43 x 10^{13} cm^{-3}, which is the same as that gravimetrically determined. The same particle concentration is obtained from d. In the previous section we reported that the suspension near the wall is more ordered than that in the interior and the particle concentration in the cell becomes uniform with improved ordering. The present result in 140 nm silica suspension suggests that 3-D order develops near the wall while 2-D order exists at the interior after the particle concentration becomes uniform in the cell.

The ion exchange reservoir was removed from the cell on day three. On day six, the sample became inhomogeneous and different regions in the suspension showed different iridescence colors under white light illumination. The 3-D Bragg diffraction spot (*vide infra*) observed in the reflection geometry became very diffuse which the 2-D Bragg spot (in the transmission geometry) became brighter. The intensity of the 2-D Bragg spot decreased slightly upon rotation of the cell around θ_1 (θ_1=42° for the 488 nm beam), but the diffracted spot occurred at an angle satisfying eqn. 2.2. The θ_1 intensity dependence on day six is smaller than that for day three. The 2-D diffraction was seen over a wide range of incident angles (17° to 67°). Figure 2.4 shows the optical attenuation spectrum of this suspension where the peaks correspond to 3-D Bragg diffraction *(vide infra)*. The observed decrease in the ordering on day six presumably derives from an increasing n_i due to leaching of ions from the sample cell.

These observations of an increased concentration of 245 nm and 140 silica particle near the wall agree with Kesavamoorthy *et al* (12,13) who observed that the particle concentration and the degree of order showed a maximum at the cell container walls. We conclude that an initial 2-D structure with a higher particle concentration nucleates adjacent to the container walls, while the

interior regions of the cell remain either gas or liquid-like. With decreasing n_i the particle concentration difference between the wall vicinity and the interior decreases, the two-dimensionally ordered region near the wall crystallizes into a 3-D FCC crystal while the interior disordered region becomes a 2-D crystal. The appearance of 2-D hexagonal layered structure in the evolution of the colloidal crystal ordering is consistent with the recent investigations (11,15,16). The entire suspension crystallizes into a 3-D crystal if the impurity concentration decreases further.

Determination of 3-D crystal structure from angle dependent optical attenuation spectra of 140 nm silica particle suspension.

Figures 2.4 and 2.5 show the optical attenuation spectra of the 140 nm silica suspension at various incidence angles recorded on day six. Figure 2.4 shows a sharp peak at 1051 nm and a broad peak around 525 nm. The *ca.* 1051 nm attenuation peak shifts to shorter wavelengths and broadens when the incident angle increases from 0° to 10°, while the broad peak at *ca.* 525 nm becomes better resolved. Since first order 3-D Bragg diffraction from the planes parallel to the quartz plate gives rise to the longest wavelength peak (1051 nm), the peaks around 525 nm should derive from second order 3-D Bragg diffraction. The peaks at 525 nm will also have contributions from first order Bragg diffraction from planes with smaller spacings than those giving rise to the 1051 nm peak. This suspension showed 3-D diffraction as well as 2-D diffraction as discussed above and the 3-D crystal near the container wall coexists with 2-D hexagonal layered structure in the interior.

In order to resolve the diffraction contributions from various planes to the 525 nm peak, we fit the optical attenuation spectra for various incidence angles to a sum of three Gaussian bands and a linear base line. The experimental spectra are shown in Figures 2.4 and 2.5 and Table 2.3 lists the best

Table 2.3

Parameters used to simulate the experimental optical attenuation spectra for the 140 nm silica particle suspension for various angles of incidence (θ). The experimental data was best fit to the sum of a linear base line (y = a - bx) and three Gaussians with peak heights A_1, A_2, A_3, peak positions x_1, x_2, x_3, and widths σ_1, σ_2, σ_3.

θ	a	b (nm^{-1})	A_1	A_2	A_3	x_1 nm	x_2 nm	x_3 nm	σ_1 nm	σ_2 nm	σ_3 nm
0	.53	700	.19	.095	--	525[+]	480[*]	--	22	22	--
4	.545	673	.183	.135	.044	522	463.5	563	24	27	17.1
5	.601	760	.155	.125	.053	522	453	566	25.5	27.5	18.1
6	.62	763	.135	.118	.05	522	441	573	27	27.5	18.1
7	.654	783	.11	.107	.045	521.5	430	578	27	27	19.9
8	.714	856	.08	.09	.04	521	419.5	583	24	24	22.6
10	.864	1080	.04	.063	.03	520	395	600	22	22	30

[+]This peak splits into three peaks at x_1, x_2, and x_3 when the incident angle is changed.

[*]This peak for normal incidence derives from the (311) set of planes.

fit parameters. Obviously, more than three diffraction peaks contribute to the broad 525 nm peak. However, even using three components allows us to unambiguously establish the dominant structure, orientation and crystal lattice parameter.

The two crystal structures observed in colloidal crystals (body centered cubic, BCC and face centered cubic, FCC) self assemble such that the highest density planes (BCC (110) or FCC (111)) lie parallel to the container walls. When the FCC (111) or the BCC (110) plane is normal to the incident radiation, the second order diffraction will overlap with the first order diffraction wavelengths from the corresponding (200) planes. The angle (β) between two planes in a crystal, (h_1,k_1,l_1) and (h_2,k_2,l_2), is given by Eq. [2.5] (23)

$$\cos\beta = \frac{h_1 h_2 + k_1 k_2 + l_1 l_2}{\sqrt{\left(h_1^2 + k_1^2 + l_1^2\right)\left(h_2^2 + k_2^2 + l_2^2\right)}} \quad \text{[2.5]}$$

Using Eqs. [4] and [5], we find that the broad peak centered at *ca.* 525 nm will have contributions from first order diffraction of the (002), (020) and (200) planes (λ_{max} = 526 nm), the (220), (202) and (022) planes (λ_{max} = 525 nm), the (311), (131) and (113) planes (λ_{max} = 478 nm) and the (222) planes (λ_{max} = 525.5 nm) as well as from the second order diffraction from the (111) planes (λ_{max} = 525.5 nm) of FCC.

The values of x_2 (nm) found from the fits (Table 2.3) were used to calculate the angles between the putative (200) plane and the incident beam (θ_{200}). The correlation between θ_{200} and the angle of rotation of the sample (Table 2.4) was excellent and proves the existence of an FCC structure. We were also able to account for the angular dependence of the diffraction from the individual (020) and (002) planes as the cell was rotated. We were able to use the fitted x_2 values to uniquely specify the

Table 2.4

The calculated θ_{200} from the experimental peak positions (x_2) of the attenuation spectra of the 140 nm diameter silica particle suspension with $n_p = 1.67 \times 10^{12}/$ cm^3 for various angles of incidence (θ) for FCC and BCC structures using the Bragg law. The calculated θ_{020} and θ_{002} from the geometrical considerations and the corresponding expected Bragg wavelength (λ_3) for various θ for FCC and BCC structures. The experimentally fitted peak position x_3 compares well with λ_3 for FCC structure.

θ	FCC				BCC			
	x_2 nm	θ_{200}	$\theta_{020}-\theta_{002}$	λ_3 nm	θ_{200}	θ_{020}	λ_3 nm	x_3 nm
0	525	35.3	35.3	525	45	45	525	525
4	463.5	30.7	37.4	551.7	38.5	51.5	577	563
5	453	29.9	38	559.6	37.6	52.4	585	566
6	441	29	38.6	567	36.4	53.6	593	573
7	430	28.2	39.2	574.5	35.3	54.7	600	578
8	419.5	27.5	39.8	581	34.4	55.6	608	583
10	395	25.8	41.1	597.2	32.1	57.9	629	600

crystal orientation about the (111) direction. From this crystal orientation we determined the angle between the (020) plane and the incident beam (θ_{020}) and that between (002) plane and the beam (θ_{002}) and we calculated the expected peak positions, λ_3 (Table 2.4) which agreed well with the experimentally determined x_3 values.

The values of λ_3 calculated assuming a BCC structure are also listed in Table 2.4, but deviate unacceptably from the experimentally determined x_3 values. We also examined the possibility that x_2 derives from diffraction from the (211) BCC planes (the only other possible diffracting plane in BCC). The differences were too great between λ_3 and x_3 for this to be likely.

To obtain further supporting evidence for the FCC structure we determined the ratio of the peak areas at *ca.* 525 nm and *ca.* 1051 nm in the attenuation spectrum. The Bragg diffracted intensity from a set of planes in a 3-D crystal, integrated over the wavelength, is given by [37]:

$$\mathbf{I_D = I_0 Q V} \quad \textbf{[2.6]}$$

where I_0 is the incident intensity, V is the illuminated crystal volume, and Q is a scattering function

$$Q = \frac{4\pi^4 \alpha^2 n^2 f^2 A}{\lambda^2 v^2} \left(\frac{1 + \cos^2 2\phi^{xtl}}{\sin^2 \phi^{xtl}} \right) \quad \textbf{[2.7]}$$

defined by Eq. [2.7] [37]

where α is the polarizability of the particle, n is the refractive index of the suspension, v is the volume of the unit cell, λ is the peak position, ϕ^{xtl} is the Bragg angle, A is a constant (4 for BCC and 16 for

$$f^2 = \left[\frac{3(\sin qa - qa\cos qa)}{q^3 a^3} \right] \quad \textbf{[2.8]}$$

36

Table 2.5

The calculated three dimensional diffraction angles (ϕ^{xtl}), the peak positions in the optical attenuation spectra (λ), the particle structure factor (f^2), the diffracted intensity from several FCC and BCC planes and the calculated integrated intensities along with the experimental ratio of integrated intensities for the suspension of 140 nm silica particles.

Structure	planes (2hkl)	$\phi^{xtl} = 90-\alpha$	$\lambda = 2nd_{hkl}\sin\phi^{xtl}$	f^2	$I_D/B \times 10^6$ for each set of planes	Ratio of integrated intensities at 525 and 1051 nm	
						Calculated	Experimental
FCC	(111)	90	1051	0.588	1.065		
	(200),(020),(002)	35.3	526	0.328	3.957		
	(220),(202),(022)	54.7	525	0.082	0.4945	13.7	
	(311),(131),(113)	60.5	478	0.044	0.3195		
	(222)	90	525.5	0.037	0.2651		14.0
BCC	(110)	90	1051	0.588	1.065		
	(200),(020)	45	526	0.148	1.067		
	(211),(121)	30	525	0.588	10.646	22.2	
	(220)	90	525.5	0.037	0.2651		

FCC) (23) and f^2 is the particle structure factor given by Eq. [2.8]

where a is the particle radius and q is the scattering vector

$$q = \frac{4n\pi \sin \phi^{xtl}}{\lambda} \quad \text{[2.9]}$$

The integrated diffracted intensity which is a function of the peak position λ and the Bragg angle ϕ can be rewritten as Eq. [2.10]

$$I_D = B \left(\frac{1 + \cos^2 2\phi xtl}{\sin^2 \phi^{xtl}} \right) \frac{f^2}{\lambda^2} \quad \text{[2.10]}$$

The attenuation at 1051 nm and 525 nm is small. Hence, the ratio of integrated diffraction intensities at 1051 and 525 nm is approximately equal to the ratio of the areas of the absorption peaks at the respective wavelengths. The ratio of the sum of the first order integrated diffracted intensities at 525 nm from the (200), (220), (311) and (222) family of planes compared to that for the (111) plane at 1051 nm for a FCC structure was 13.7. This agrees extremely well with the experimental value of 14, confirming the initial crystal structure assignment. Table 2.5 lists the calculated integrated diffraction intensities for all the relevant planes of a FCC crystal.

A similar calculation was carried out for a BCC crystal, but the peak area ratio of 22.2 is too large. Table 2.5 also lists the diffraction wavelength that can be expected in the optical attenuation spectrum for normal incidence, from a FCC and a BCC crystal. A comparison of Tables 2.3 and 2.5 shows that all the expected peaks for a FCC crystal are observed. In contrast, the BCC (310) and (130) planes should show peaks at *ca.* 420 nm which are not observed.

2.5 Conclusion:

We have studied the time dependence of the crystallization of order within a colloidal silica suspension. We find that the formation of a randomly stacked 2-D crystal is an intermediate stage in the formation of a 3-D crystal. Nucleation occurs at the walls of the container, possibly due to the attraction of image charges. We demonstrate that optical attenuation spectroscopy can be used to unambiguously determine the structure of colloidal suspensions.

2.6 References:

1. Russel, W.B., Saville, D.A. and Schowalter, W.R., "Colloidal Dispersions", Cambridge Unive. Press, NY, **1989**.

2. Robbins, M.O., Kremer, K. and Grest, G.S., *J. Chem. Phys.* **1988**, 88, 3286.

3. Kesavamoorthy, R., Sood, A.K., Tata, B.V.R. and Arora, A.K., *J. Phys. C: Solid State Phys.* **1988**, 21, 4737.

4. Asher, S.A., Flaugh, P.L. and Washinger, G., *Appl. Spectrosc.* **1986**, 1, 26.

5. Hone, D., Alexander S., Chaikin, P.M., and Pincus, P., *J. Chem. Phys.* **1983**, 79, 1474.

6. Iler, R.K., "The Chemistry of Silica", Chap.3, Wiley, New York, **1979**.

7. Verwey, E.J.W. and Overbeek, J. Th.G., "Theory of the Stability of Lyophobic Colloids", Elsevier, Amsterdam, **1948**.

8. Okubo, T., *J. Chem. Soc., Faraday Trans. I*, **1986**, 82, 3185.

9. Kesavamoorthy, R., Tata, B.V.R., Arora, A.K. and Sood, A.K., *Phys. Lett. A*, **1989**, 130, 208.

10. Gruner, F. and Lehmann, W.P., *J. Phys. A: Math. Gen.* **1982**, 15, 2847.

11. Clark, N.A., Hurd, A.J. and Ackerson, B.J., *Nature*, **1979**, 281, 57.

12. Kesavamoorthy, R., Rajalakshmi, M. and Babu rao, C., *J. Phys: Condens. Matter*, **1989**, 1,

7149.

13. Kesavamoorthy, R., Babu Rao, C. and Tata, B.V.R., *J. Phys: Condens. Matter*, in press.

14. Pieranski, P., *Contemp. Phys.* **1983**, 24, 25.

15. Sogami, I.S., Yoshiyama, T., *Phase Transitions*, **1990**, 21, 171.

16. Monovoukas, Y. and Gast, A.P., *J. Colloid Interface Sci.* **1989**, 128, 533.

17. Asher, S.a., U.S. Paternts Nos. 4,627,689 and 4,632,517.

18. Krieger, I.M. and O'Neill, F.M., *J. Am. Chem. Soc*, **1968**, 90, 3114.

19. Udo, M.K. and de Souza, M.F., *Solid State Commu.* **1980**, 35, 907.

20. Hiltner, P.A. and Krieger, i.M., *J.Chem. Phys.* **1969**, 73, 2386.

21. Rundquist, P.a., Jagannathan, S., Kesavamoorthy, R., Brnardic, C., Xu, S. and Asher, S.A., *J. Chem. Phys.* **1991**, 94, 711.

23. Carlson, R.J. and Asher, S.A., *Appl. Spectrosc.* **1984**, 38, 297.

24. Hachisu, S., Kobayashi, Y., and Kose, A., *J. Colloid Interface Sci.* **1973**, 46, 470.

25. Fujita, H., and Amitani K., *Jap. J. Appl. Phys.* **1977**, 16, 1091.

26. Ackerson, B.J. and Clark, N.A., *Phys. Rev. Lett*, **1981**, 46, 123.

27. Schaefer, D.W. ad Ackerson, B.J., *Phys. Rev. Lett*, **35**, 1448 (1975).

28. Okubo, T., *J. Chem. Soc. Faraday Trans. I*, **1988**, 84, 1171.

29. Stober, W., Fink, A. and Bohn, E., *J. Colloid and Inter. Sci.* **1968**, 26, 62.

30. Van Helden, A.K., Jansen, J.W. and Vrij, A., *J. of Colloid and Inter. Sci.* **1981**, 81, 354.

31. Hartl, W. and Versmold, H., *J. Chem. Phys.*, **1984**, 80, 1387.

32. Arora, A.K. and Kesavamoorthy, R., *Solid State Commun.* **1985**, 54, 1047.

33. Hurd, A.J., "The Lattice Dynamics of Colloidal Crystals", PhD. Dissr., University of

3.0 Preparation and Properties of Tailored Morphology, Monodisperse Colloidal Silica-Cadmium Sulfide Nanocomposites

3.1 Executive Summary

We have developed a new synthetic methodology for preparing ca 40-300 nm monodisperse silica-cadmium sulfide nanocomposite spheres. This methodology uses water-in-oil microemulsions in which monodisperse silica colloids are produced by the controlled hydrolysis of tetraethyl orthosilicate (TEOS) in water nanodroplets. The resulting pure silica spheres can be grown to between 40 to 80 nm in diameter and can be used as seed particles for production of larger silica colloids upon further reactions with TEOS in the microemulsion. Cadmium sulfide quantum dots are incorporated into the silica colloids during the silica sphere synthesis, by the simultaneous co-precipitation of cadmium nitrate and ammonium sulfide in the water nanodroplets. The CdS can be introduced as a homogenous dispersion of CdS quantum dots (ca 25 Å diameter), or as large inclusions or as surface caps, or as the central core of a silica particle or as shells of CdS interleaved between silica shells. These different nanoscale complex morphologies in silica are created by controlling the co-precipitation of CdS. Techniques including TEM, SEM/EDS, X-ray diffraction, and light scattering were used to characterize the elemental analysis as well as particle morphology. In addition, we have prepared doublet and triplet spheres which are connected by welds of CdS. This silica-CdS nanocomposite is a new material with potential utility for non-linear optics. Further processing makes this material useful for a new class of high surface area catalytic supporting materials.

3.2 Introduction

Synthetic chemistry is a mature science which has developed a host of successful strategies for fabricating complex molecular structures. For example, methodologies have been developed to make clusters of atoms and molecules such as, for example, buckminsterfullerene[1] and CdS quantum dots.[2-6] The present frontier of chemical synthesis

In an accompanying paper[17] we demonstrate that we can selectively etch out the CdS inclusions to form silica spheres with complex cavities and porosities. These porous systems will be useful for novel supporting materials for catalytic applications.

Our approach for this new synthesis utilizes water-in-oil microemulsions where the silica spheres are synthesized by the hydrolysis of tetraethoxysilane (TEOS), followed by its condensation in the water nanodroplets. This microemulsion method of formation of silica spheres was recently reported by Ossea-Asare and Arriagada.[18] We have combined this method of synthesis of silica spheres with the controlled precipitation of CdS particulates in water nanodroplets in these water-in-oil microemulsions. This work follows previous demonstrations by others that monodisperse CdS quantum dots can also be synthesized in water-in-oil microemulsions.[2-6] We have combined these approaches to, for the first time, prepare monodisperse CdS quantum dot inclusions in monodisperse silica sphere colloids.

Our microemulsion approach, which yields more uniform spheres than the classic Stöber process[19] for the smaller size range (30-150 nm), gives comparable uniformities for larger spheres (150-300 nm). We believe we have developed a simple general approach for creating nanocomposites with complex morphologies which can be used for a variety of materials, such as CdSe, etc. in silica spheres, or for synthesizing spherical colloids made of other materials such as alumina, etc. We also have developed an approach to synthesize doublets and triplets of spheres where the CdS acts as a weld between spheres.

3.3 Experimental

Water-in-oil microemulsions were prepared from non-ionic surfactants using procedures similar to those of Osseo-Asare and Arriagada.[18] We used two ionic surfactants, either polyoxyethylene nonylphenyl ether with an average of 5 oxyethylene groups per molecule (Igepal CO520) from GAF chemical and obtained from Aldrich Chemicals, or Triton N-101 from Rohm and Haas (obtained from Fluka). Both surfactants were used without further purification. The tetraethyl orthosilicate (TEOS, 99%, Fluka) was distilled before use. The other chemicals used, such as cyclohexane (Fisher Scientific), hexyl alcohol (Aldrich),

involves development of strategies to create even larger assemblies, with molecular weights greater than 10^9 gm/mole and of assemblies composed of complex composites of macromolecular size.

In this regard numerous groups have developed synthetic methods to form monodisperse particles of organic polymers[7,8] or of inorganic materials.[9] Generally these particles are spherical and have molecular weights greater than 10^9 gm/mole. In special cases these particles can be non spherical and may have unique materials science applications.

One objective of this work discussed here is to use these monodisperse particles for new ceramics materials or for use as catalyst supports. Our major interest, however, is to use these spherical particles in colloidal self-assembly processes for preparing crystalline colloidal arrays.[10-16] These nanoscale periodic materials are useful for fabricating optical devices because the spherical particles array themselves at the lattice sites of body centered cubic or face centered cubic arrays, which efficiently diffract light in the visible or near IR spectral regions.

It would be desirable to prepare nonlinear crystalline colloidal arrays where the colloidal spheres were prepared from nonlinear materials which change their refractive index such that the diffraction properties of the array change at high incident light intensities. The material could act as an optical limiter or switch. In this regard the refractive indices of the spherical colloidal particles would change as the incident intensity increased. Our choice for the nonlinear material has centered on CdS quantum dots.

CdS quantum dots have among the largest optical nonlinearities known. In this report we describe the fabrication of new nanocomposites composed of CdS quantum dots ($\underline{ca}$ 25 Å) uniformly dispersed in monodisperse silica spheres in the size range of 40-150 nm. In addition, our preparation also can be used to fabricate nanocomposites where the CdS form patches within the spheres and on the surfaces of the spheres, as well as forming a CdS core of the silica spheres. In addition, we can form multidecker shells of silica, CdS, silica, etc.

ammonium hydroxide (29%, Mallinckrodt), cadmium nitrate (certified, Fisher Scientific), ammonium sulfide (22%, Fisher Scientific) and de-ionized water (obtained using a Nanopure water purifier, Barnstead Co.) were used as received.

The microemulsion reaction matrix was prepared using either Igepal CO-520 or Triton N-101. Although different detailed recipes were used for each preparation a typical recipe would involve 270 ml of a microemulsion prepared at ambient temperature in a 500 ml four neck reaction flask stirred by a teflon paddle connected to a high torque stirring motor. The microemulsion reactant concentrations were 5.20 M cyclohexane, 0.72 M H_2O, 0.18 M hexanol, 0.12 M Triton N-101, and 0.094 M NH_4OH. The Igepal CO-520 microemulsions contained a similar surfactant concentration, but contained no hexanol. Ten ml of pure TEOS liquid was injected within 10 min into the stirred microemulsion matrix by using a syringe pump. As the reaction proceeds over a period of 24 hr the TEOS slowly hydrolyses and $Si(OH)_4$ precipitates and condenses within the water nanodroplets to eventually form monodisperse SiO_2 spheres.

The SiO_2 CdS quantum dot sphere composites were made by injecting separate microemulsions containing Cd^{2+} and S^{2-}. To produce 10% (by mole) CdS quantum dot inclusions, we injected approximately 54 ml of two microemulsions containing either $Cd(NO_3)_2$ or $(NH_4)_2S$. These microemulsions contained the following final reactant concentrations: 26.85 M cyclohexane, 1.65 M H_2O, 0.41 M hexanol, 0.275 M Triton N-101, and 4.48 x 10^{-3} M $Cd(NO_3)_2$ or $(NH_4)_2S$. These microemulsions were prepared by the addition of the aqueous salt solutions to the microemulsion.

The order and timing of injection of the TEOS and the $Cd(NO_3)_2$ and $(NH_4)_2S$ microemulsions determine the CdS morphology within the SiO_2 spheres. For example, to make uniformly dispersed CdS quantum dots in the SiO_2 spheres we first injected the TEOS solution within 10 min and 1 hr later began injecting the $Cd(NO_3)_2$ and $(NH_4)_2S$ microemulsions. We simultaneously injected these two solutions over a period of 24 hr. It is important to note that the TEOS reaction rate is much slower in the microemulsions than

occurs in the Stöber process.

The particle morphology was examined by transmission electron microscopy (JEOL 2000FX/LINK AN10000 and Zeiss 902). The micrographs were analyzed by using a digital imaging system (BioScan, Inc. WA). Energy dispersive scanning electron microscopy-x-ray analysis (JEOL 35CF) was employed for semi-quantitative element determinations. The samples were prepared for SEM/EDS, by drying a dispersion of the reaction products on a carbon stage and transferring this stage to the microscope. The colloids were washed, solvent exchanged, and dialyzed before Zeta potential determinations made by using a Malvern Zetasizer 4 electrophoretic light scattering instrument. Particle surface areas were measured by using the BET nitrogen absorption method (Automatic Surface Area Analyzer 4200, Beta Scientific Corp.). The crystal structures were determined by X-ray powder diffraction measurements of freeze-dried nanocomposite particles (Philips X'PERT). Absorption measurements to investigate CdS quantum confinement effects were performed by directly examining the liquid reaction products by using a UV/VIS/NIR spectrometer (Perkin-Elmer, Lambda 9).

3.4 Results and Discussion

Silica Sphere Growth

Previous studies by Arrigada and Osseao-Asare[18] demonstrated that monodisperse, small SiO_2 spheres can be grown in the size range of 40 to 70 nm by controlled hydrolysis and condensation of TEOS within reverse micelles. We have scaled up this synthesis by fifty-fold for preparative purposes and developed new synthetic methods for creating complex nanocomposites. Figure 3.1 shows a TEM micrograph of 41.3 nm SiO_2 spheres prepared by using a microemulsion with Igepal CO-520 surfactant. The reaction utilized a concentration 0.0537 M TEOS, and 0.1269 M NH_3 with a water to surfactant concentration ratio, w, of 5 (w=[water]/[surfactant]), and a water to TEOS concentration ratio, h, of 4.8 (h=[water]/[TEOS]). The silica sphere diameter and the diameter distribution are sensitive to
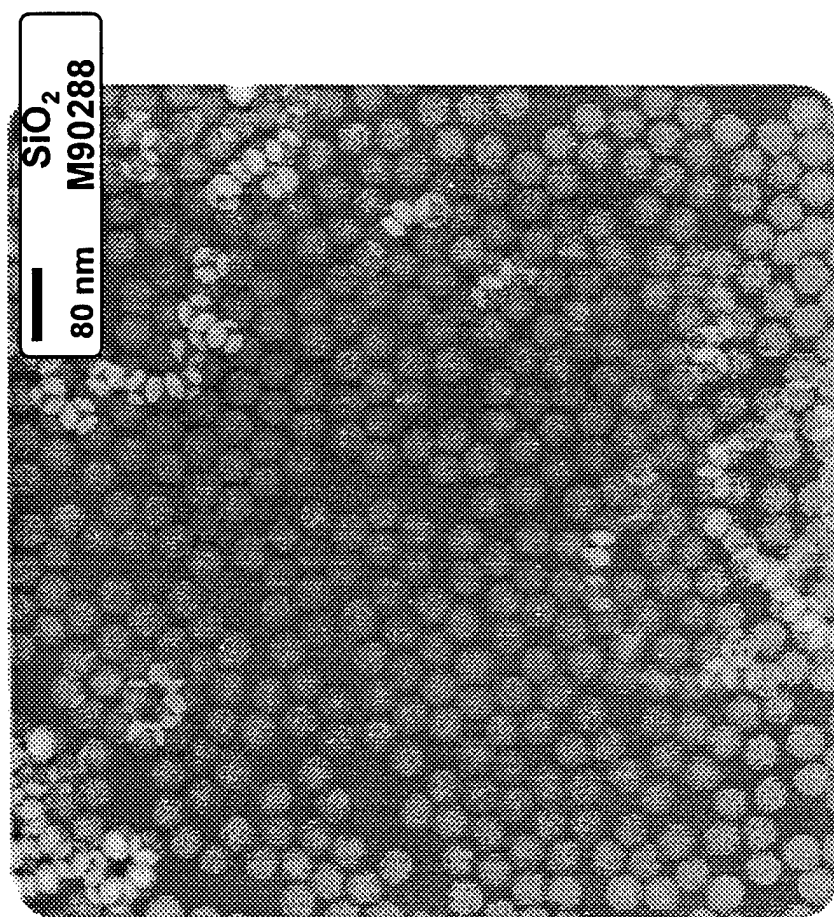
Figure 3.1.   TEM micrograph of monodisperse silica spheres synthesized in an Igepal CO-520 microemulsion with $w = 5$, $h = 4.8$, 0.0537M TEOS, and 0.1269 M NH3   (size relative standard deviation is 4.2%).

reactant concentrations; the w value is most important for determining size. Increasing the alcohol concentration generally increases the polydispersity because of the sensitivity of the microemulsion phase diagram to the alcohol content. This limits the maximum concentration of TEOS which can be used since TEOS hydrolysis and condensation releases ethanol. For example, we find that the relative standard deviation in particle size increases from 5% to 14% as we increase the TEOS concentration from 0.09 M to 0.179 M.

Higher concentrations of TEOS can be utilized in microemulsions containing Triton N-101 because this microemulsion is less sensitive to alcohol content. In this case the presence of hexanol as a co-surfactant improves the uniformity. For example, we synthesized silica particles with an average diameter of 76 nm with a relative standard deviation of 4.8% by using a Triton N-101 microemulsion containing 0.179 M TEOS, 0.15 M NH_3 with $w=6$, $h=6$ and $cs=4$ ($cs=$[water]/[hexanol]).

Arragada and Osseo-Asare have shown for Igepal microemulsions that increasing w decreases the particle size and results in better uniformity. However, we observe that Triton N-101 microemulsions permit higher w values which allow us to double the particle diameter, while allowing us to maintain an excellent uniformity. Although Triton N-101 and Igepal CO-520 have similar chemical structures they have different molecular weights. Our results indicate that Triton N-101 microemulsions can be used to synthesize larger monodisperse silica spheres.

We examined the reaction kinetics by monitoring the time dependence of the particle size by using TEM. Figure 3.2 shows the effects of w and h on particle growth in Igepal CO-520 microemulsions. For a constant ratio of water to TEOS of $h=4.8$, a decrease in the total water content (smaller w) results in a faster growth rate and larger spheres. This is exactly the opposite of what would occur in the Stöber process. A decrease in water concentration is also reported to yield more polydisperse silica spheres.[18] In contrast, we observe little dependence. Our synthesis with $h=4.8$ and $w=5$ gave 46 nm spheres with a size relative standard deviation of 5.2%, while for $h=4.8$ and $w=1$ the 56 nm spheres had a size relative standard
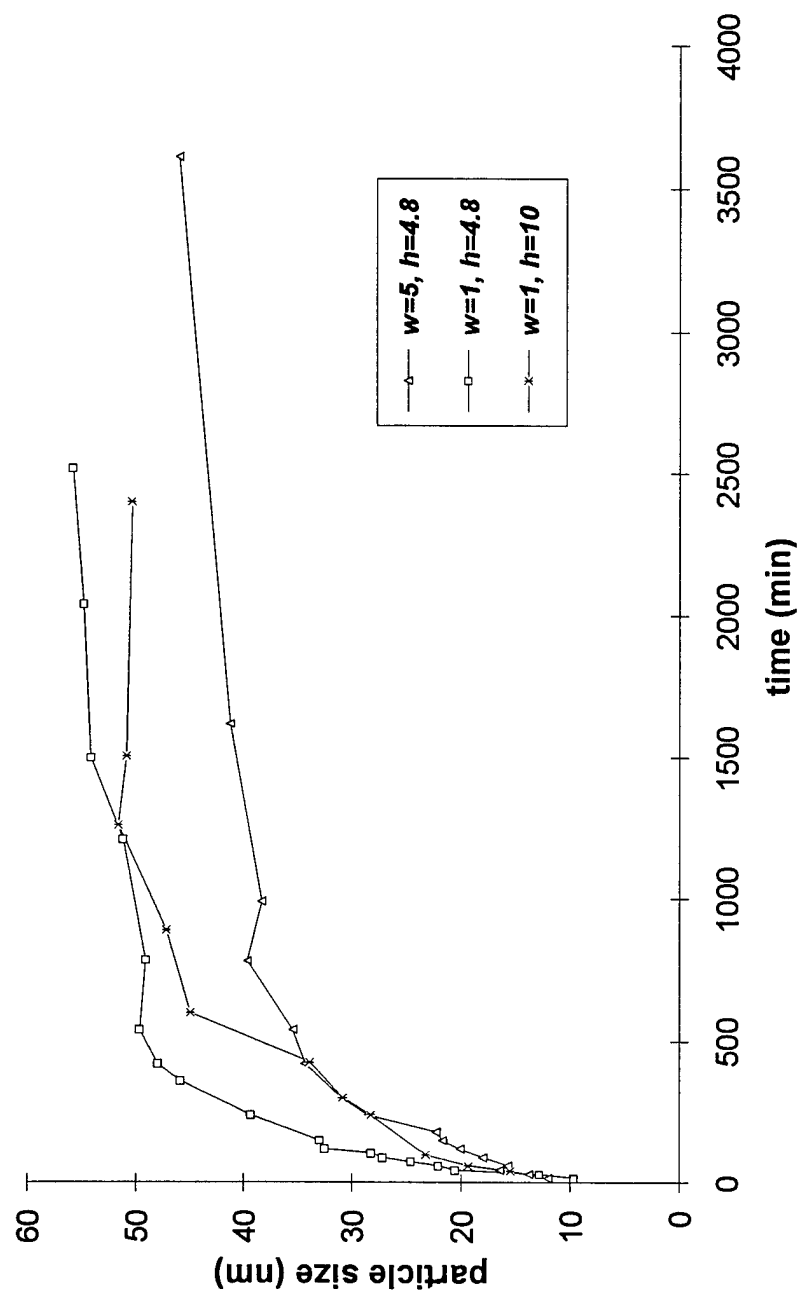
Figure 3.2.   Particle size evolution for silica sphere synthesized in Igepal CO-520 microemulsions with different values of *w* and *h*.

deviation of 4.0%.

For a constant w, increasing h decreases the growth rate and the particle size. The synthesis with $w=1$, $h=4.8$ yields 56 nm spheres, while a synthesis with $w=1$, $h=10$ yields 50 nm spheres. This contrasts to the Stöber process, where an increased h increases the hydrolysis rate and increases the particle size.[20] We find little dependence of the reaction on ammonia concentration. This differs from the Stöber process; the NH_3 concentration determines the hydrolysis rate and the particle size.

Nucleation and Growth of Large Particles

To obtain larger silica spheres we continued the growth of small monodisperse spheres by adding additional TEOS after the original growth phase. This technique is similar to that demonstrated by Unger's group for the Stöber process.[28] We probably can grow monodisperse silica spheres as large as 300 nm by this process. This process also allows us to accurately synthesize any desired particle diameter since the final diameter is determined solely by the initial size of the seed silica sphere and by the additional TEOS added which totally condenses upon the seeds, without formation of any new silica spheres. This is evident from Table 3.1 which compares the size expected to that determined for the larger silica spheres grown from the smaller silica nuclei.

Silica-CdS Sphere Composites

CdS quantum dot were incorporated in the monodisperse silica spheres were obtained by injecting microemulsions containing Cd^{2+} and S^{2-} ions into the growing silica spheres. This process involves the controlled co-precipitation of SiO_2 and CdS. As shown in Figure 3.3 different morphologies could be prepared by altering the order and timing of the injection. These morphologies include homogeneously distributed CdS quantum dots, large patches of CdS, cores of CdS, shells of CdS, CdS sandwiches and exterior bound CdS quantum dots.

Table 3.1. Results of second growth of silica colloids in Triton N-101 microemulsions.

Sample	Initial Size (nm)	No. of Particles	Additional TEOS (Mole)	Expected Size (nm)	Determined Size (nm)
SYC101RG	77±5	1.2×10^{15}	2.2×10^{-2}	134	129±6
SYC107RG1	77±4	1.2×10^{15}	1.8×10^{-2}	110	103±5
SYC107RG2	76±4	1.2×10^{15}	1.8×10^{-2}	110	112±7
SYC107RG4	76±4	1.2×10^{15}	6.7×10^{-2}	150	147±6
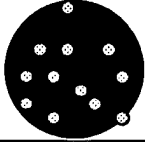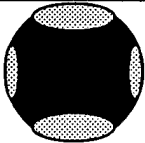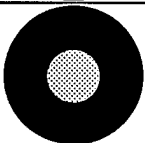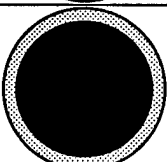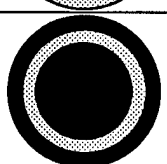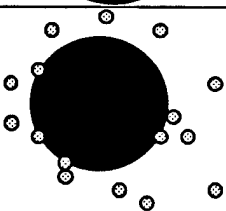
CdS distribution in SiO_2	Morphology of composite particles
CdS Homogeneous	
CdS Surface Patch	
CdS Core	
CdS Shell	
CdS Sandwich	
CdS Surface Inclusions	

Figure 3.3. Schematic illustrating the fabricated morphologies of silica-CdS composites.

51

Homogeneously distributed CdS dots (raisin bread) were prepared by pulsed injection of the Cd^{2+} and S^{2-} microemulsions with a pulsation rate proportional to the increasing volume of silica spheres. Figure 3.4 shows a TEM micrograph of silica spheres containing uniformly dispersed ca 25 Å CdS quantum dots (vide infra) at a final CdS concentration of 3 Mole%. These ca 100 nm composite silica-CdS spheres were synthesized by using 50 ml of a Triton N101 microemulsion with $w=6$, $h=6$, and $sc=4$ to grow silica sphere nuclei of 76 nm. After formation of these nuclei, 4 ml of pure TEOS was quickly injected, and two streams containing Cd^{2+} and S^{2-} microemulsions were injected in a pulsed mode over a period of 24 hr. Initially the Cd^{2+} and S^{2-} microemulsions were injected in 10 sec pulses to each deliver 5×10^{-4} Moles of Cd^{2+} and S^{2-} ions. A 40 second interval followed each 10 sec injection. Over a period of 24 hr we gradually increased the injection time to deliver an increasing amount of Cd^{2+} and S^{2-} ion during each cycle to ultimately result in a final concentration of 3 Mole % CdS inclusions in the silica spheres.

Figure 3.5 shows a TEM micrograph of silica spheres with cadmium sulfide patches on the surface and within the interior. These nanocomposite spheres were prepared by injecting a larger amount of the Cd and S microemulsions at each injection, while utilizing fewer injections.

The CdS core silica particles (Figure 3.6) were prepared by first synthesizing 6 nm CdS cores in the microemulsion with $w=3$, $h=4.8$ and subsequently growing silica spheres around the cores to a final 39 nm diameter. To synthesize the CdS cores, two Igepal microemulsions containing the Cd and S ions were slowly injected into an identical Igepal microemulsion. The total amount of Cd and S added depended upon the desired size of the CdS core. We injected a total of 2.2 mMoles of Cd and S over a period of two hours. We then added 5 ml TEOS within ten minutes. The reaction was completed over a period of 20 hrs.

Spherical shells of CdS were grown around the silica spheres by first synthesizing the silica cores followed by addition of Cd and S microemulsions, followed by another step of

50 nm

SiO$_2$-CdS
SYC107RG2
M150000
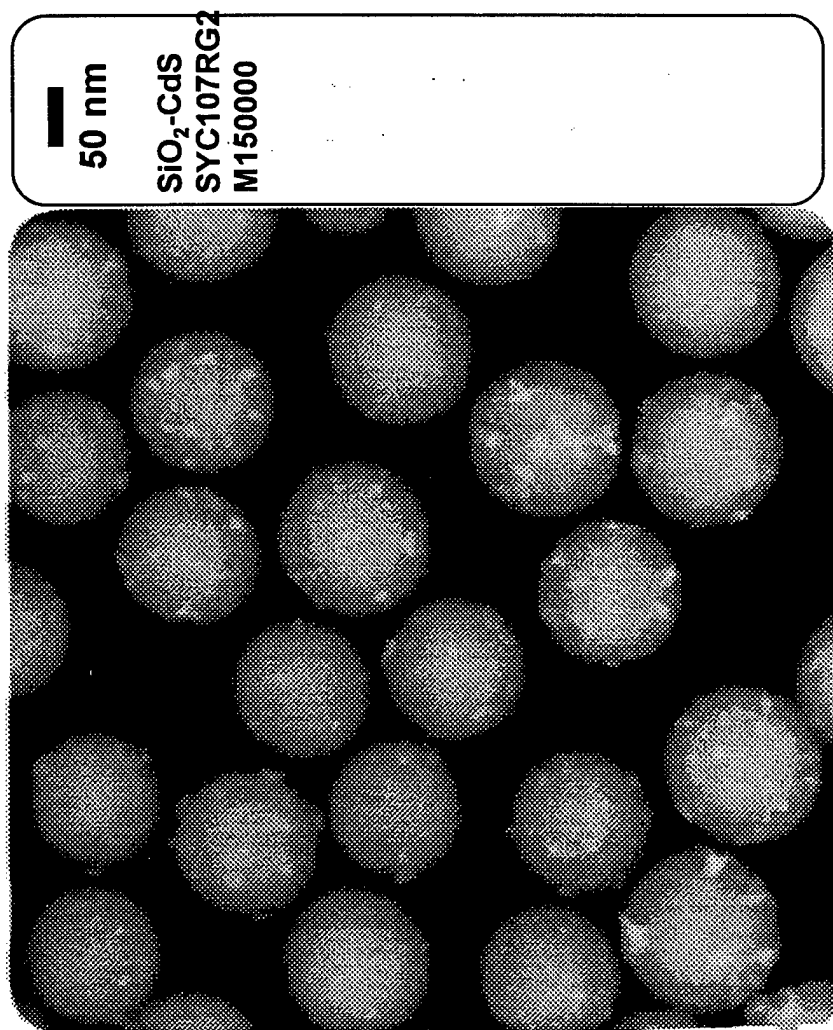
Figure 3.4.   TEM micrograph of homogeneously distribution of CdS dots in silica-CdS nanocomposite spheres.

80 nm

SYC118Q
M90288
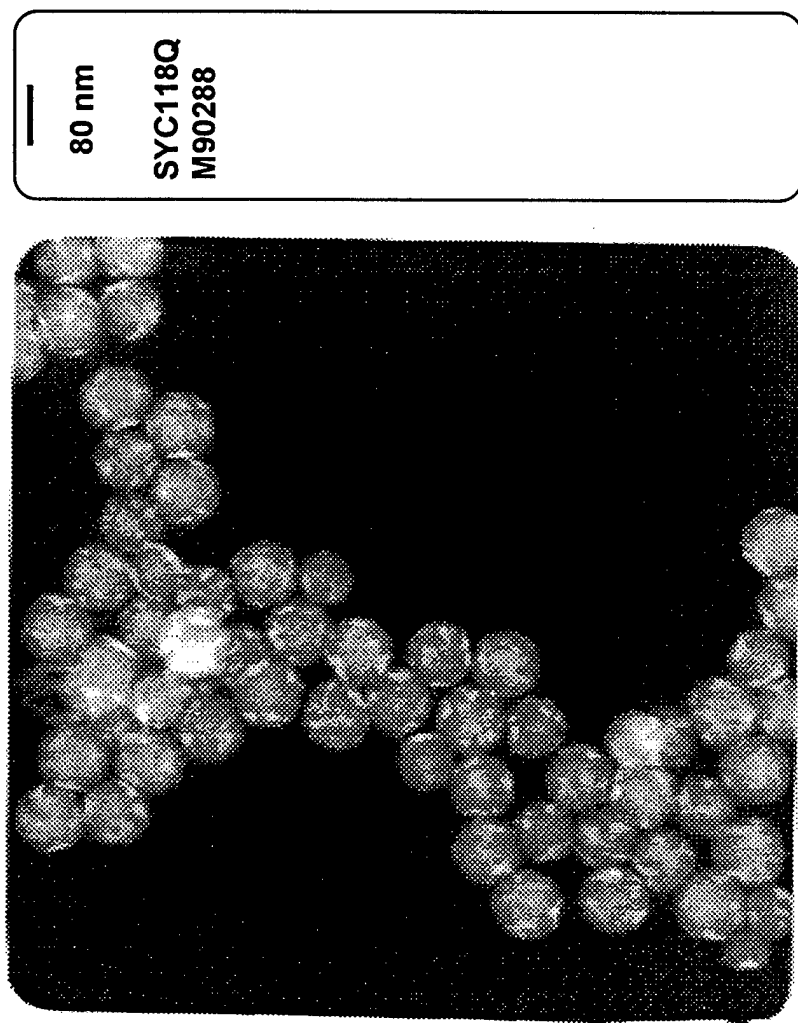
Figure 3.5.   TEM micrograph of silica-CdS nanocomposite spheres with CdS patches within and on the sphere surface.

SYC 88Q
200KV

50 nm
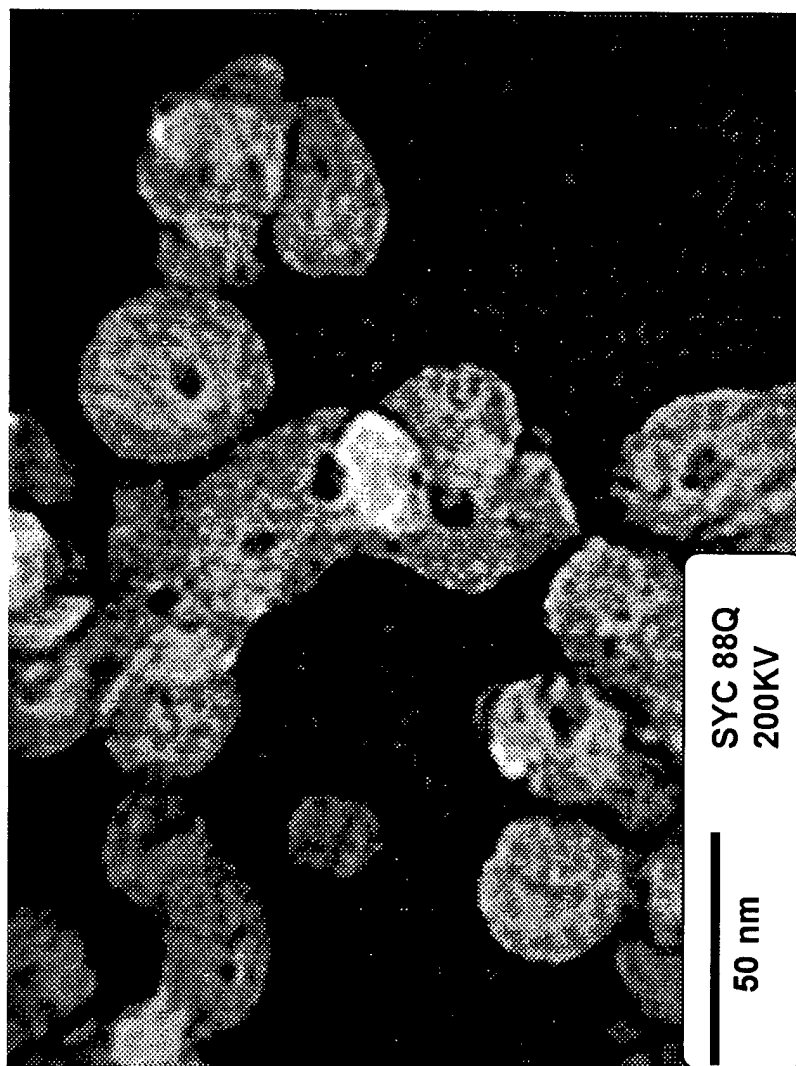
Figure 3.6. TEM micrograph of ca 39 nm silica particles with ca 6 nm CdS cores. The photograph shows these silica particles after acid dissolution of the CdS cores. This results in ca 6 nm voids at the sphere centers.

silica growth. These sandwiches can be visualized only by etching away the CdS layers as shown in the accompanying paper.[17] If desired, additional layers of CdS and TEOS can be added. In principle, numerous layered shells could be prepared using this method to allow multidecker silica-CdS sandwiches.

Silica spheres synthesized with CdS quantum dot surface inclusions were prepared by using thioacetamide, which reacts more slowly with cadmium nitrate in the water nanodroplets. For example we prepared 54 nm silica spheres with CdS particle surface inclusions of sizes ranging between 4 and 7 nm by using alcohol free Igepal microemulsions with 5 mM thioacetamide with $w=3$, $h=4.8$. The $Cd(NO_3)_2$ microemulsion was injected in a pulsed mode over a period of 24 hr.

Sphere doublets and triplets, where two or three silica spheres are joined by CdS quantum dot welds (Figure 3.7) were grown by a three-step growth process. The initial synthesis fabricated a 45 nm CdS coated silica sphere with large CdS caps on the surface. These core particles were synthesized over a period of 20 hrs in an Igepal CO-520 microemulsion with $w=3$, $h=4.8$. The initial reaction microemulsion contained 0.14 M Igepal. $Cd(NO_3)_2$ and $(NH_4)_2S$ containing microemulsions were added after an initial reaction period of 6 hrs after the TEOS injection, in order to localize the CdS patches on the surface. The Cd and S microemulsions were added by pulsed injection over a period of 14 hrs. The final CdS concentration was 5 mole % of that of the silica.

In the second step additional Igepal (0.025 Moles), TEOS (0.18 Moles) and NH_4OH solution (0.52 Moles) were added to 100 ml of the above solution in order to increase the sphere size to 75 nm. The $h=4.8$ value was maintained to be identical to that above. This reaction microemulsion was rapidly stirred for an additional 12 hrs. TEM micrographs show formation of doublets and triplets at the end of step 2.

In the third step additional Igepal (0.042 Moles), TEOS (0.022 Moles) and NH_4OH solution (0.17 Moles) were added and the reaction continued with rapid stirring for an additional 50 hrs. The final microemulsion had $w=4$. These reactions resulted in a complex

80 nm

SiO$_2$-CdS
SYC113 Step3
M90288
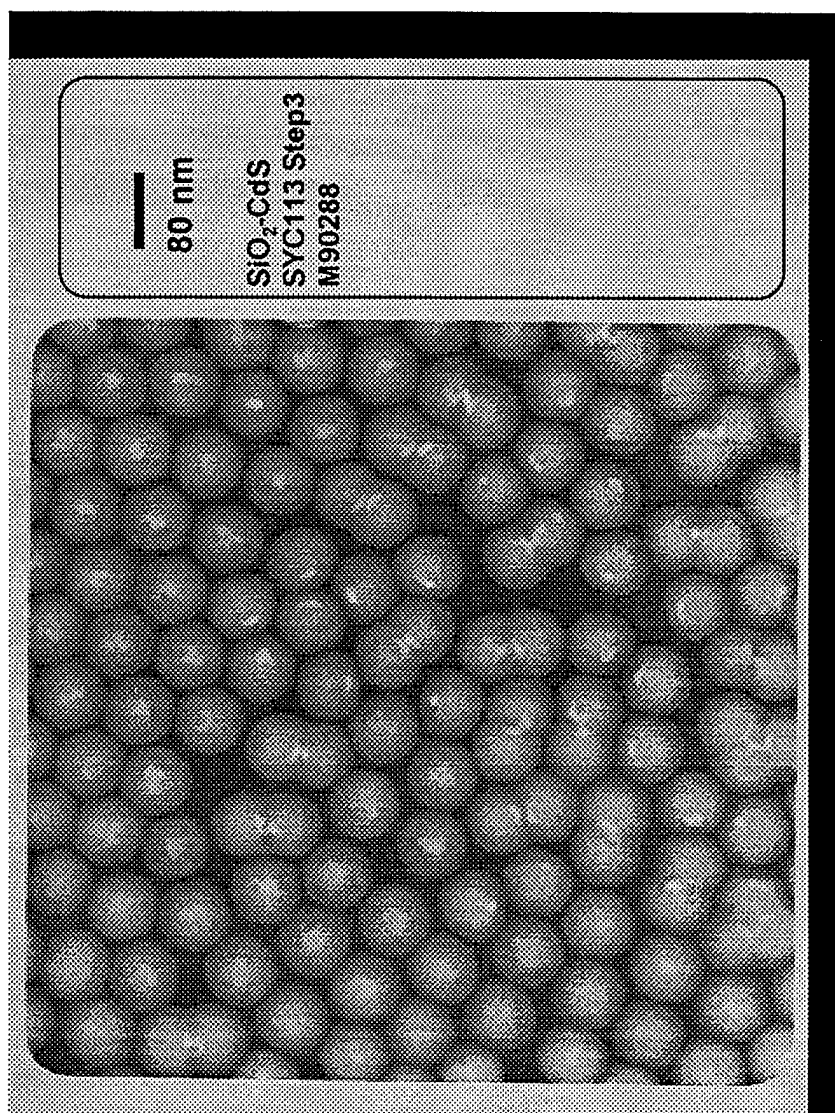
Figure 3.7.   TEM micrograph of doublet and triplet silica spheres welded by CdS inclusions.

colloid containing mainly 90 nm diameter silica spheres. However, many of the spheres formed doublets and some triplets in which the spheres were attached by CdS welds as observed in Figure 3.7.

The formation of these welded spheres during the synthesis probably occurred due to collisions between spheres with CdS patches during step 2. Since the patches are sparse most collisions were elastic and the spheres repelled one another due to their surface charge and due to constraints imposed by the microemulsion water droplet size. Collisions where the CdS patches fortuitously touched, caused adhesion. Further condensation of silica irreversibly fixed the doublets and triplets.

Chemical Composition and Structure

We determined the elemental composition of the CdS-SiO$_2$ sphere composites by using SEM/EDS. Figure 3.8 shows a typical spectrum where the separate peaks from the Si, Cd and S were used to determine the relative atomic concentrations. Table 3.2 tabulates the results for three homogeneously distributed sillica-CdS sphere composites. Good agreement is generally found between the calculated and expected CS concentrations. However, some preparations did not incorporate all of the CdS added, as indicated for sample SYC76Q where less than half of the 8 mole % originally added incorporated.

The broad x-ray diffraction of the silica spheres indicates that the SiO$_2$ is amorphous (Figure 3.9). The silica-CdS sphere composites show sharper peaks for the CdS inclusions (Figure 3.9b) which indicate that the CdS inclusions are in a cubic phase[21,22] of a Hawleyite structure.[23]

The CdS diffraction peaks are relatively broad due to the small size of the inclusions (<u>ca</u> 25 Å from the TEM micrographs). We use the Scherrer diffraction formula relating diffraction angular width, β, to the domain size, D to get an independent measure of the CdS inclusion size:

$$D = k\lambda/\beta\cos\theta$$
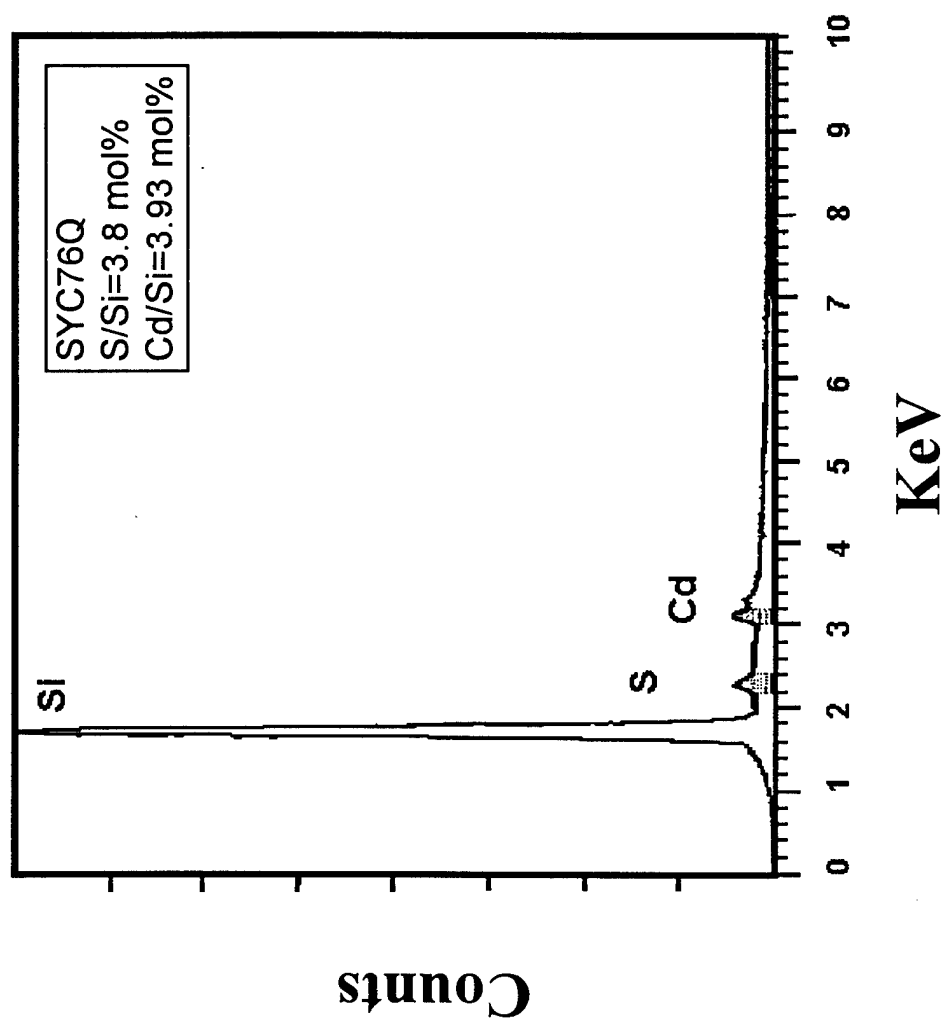
Figure 3.8.   SEM/EDS elemental analysis of silica-CdS nanocomposite.

59

Table 3.2. Result of SEM/EDS analysis on silica-CdS nanocomposites.

Sample	S/Si, mole%	Cd/Si, mole%	S/Si, mole%	Cd/Si, mole%
	determined		expected	
SYC76Q	3.8±0.2	3.9±0.1	8	8
SYC82Q	8.5±0.1	11.5±0.1	10	10
SYC92Q	8.8±0.5	8.5±0.2	7.9	7.9
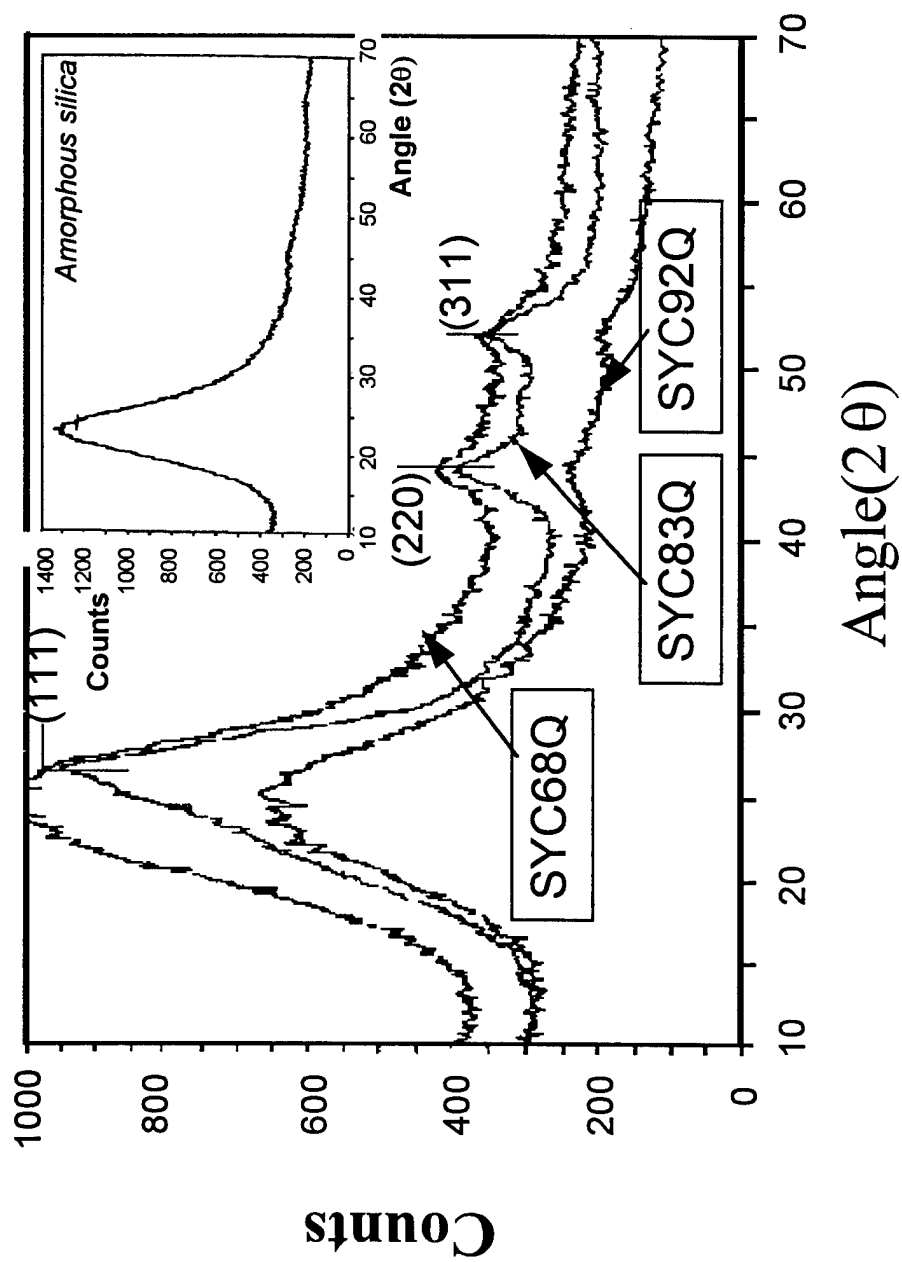
Figure 3.9.   Typical x-ray powder diffraction spectrum of silica spheres and silica-CdS nanocomposite spheres.

where $k=1$ for the CdS cubic structure, λ is the x-ray wavelength (1.541 Å), and θ is the diffraction angle. We calculate a 25 Å CdS diameter.

Particle Properties

The surface charge of the CdS nancomposites differs from that of the pure silica particles. The isoelectric point of our silica-CdS sphere composites is pH 2.5 while that of the silica spheres is 3.8.

Table 3.3 lists the BET surface area measurements of our particles. The particles show surface areas approximately two times larger than those calculated to result from their spherical outer surface areas assuming a particle density of 1.9 gm/mole.[26] There are typically large variations in the surface areas of Stöber synthesized silica spheres since the poriosity depends strongly on the preparation conditions.[24,25] Although some variation exists between our preparations, the porosities of the silica-CdS nanocomposite spheres are similar to that of the pure silica spheres.

Quantum Confinement

CdS quantum dots show blue shifts of their band edges due to quantum confinement effects associated with the small size of the particles which limit the volume occupied by the electron and the electron hole-pair formed. Figure 3.10 shows the UV-visible absorption spectrum of the pure silica spheres and the silica-CdS nanocomposite spheres. No absorption of the silica spheres is evident until $\underline{ca}$ 330 nm although some increase in scattering is evident at shorter wavelengths. For the silica-CdS composites the CdS band edge occurs at $\underline{ca}$ 430 nm; the existing experimental correlation of band edge and quantum dot size[27] can be used to estimate an inclusion size of $\underline{ca}$ 24 Å, which is close to that estimated from both the TEM photographs and the x-ray diffraction peak width measurements.

Table 3.3. BET specific surface area measurements of selected silica and silica-CdS nanocomposites.

	Sample ID	Particle diameter (nm)	Specific surface area (m^2/gm)
Plain SiO$_2$	SYC60	62	105
	SYC66	74	117
	SYC98	60	78
	SYC89	61	82
SiO$_2$-CdS nanocomposite	SYC68Q	62	104
	SYC83Q	46	112
	SYC99Q	71	113
	SYC92Q	62	183
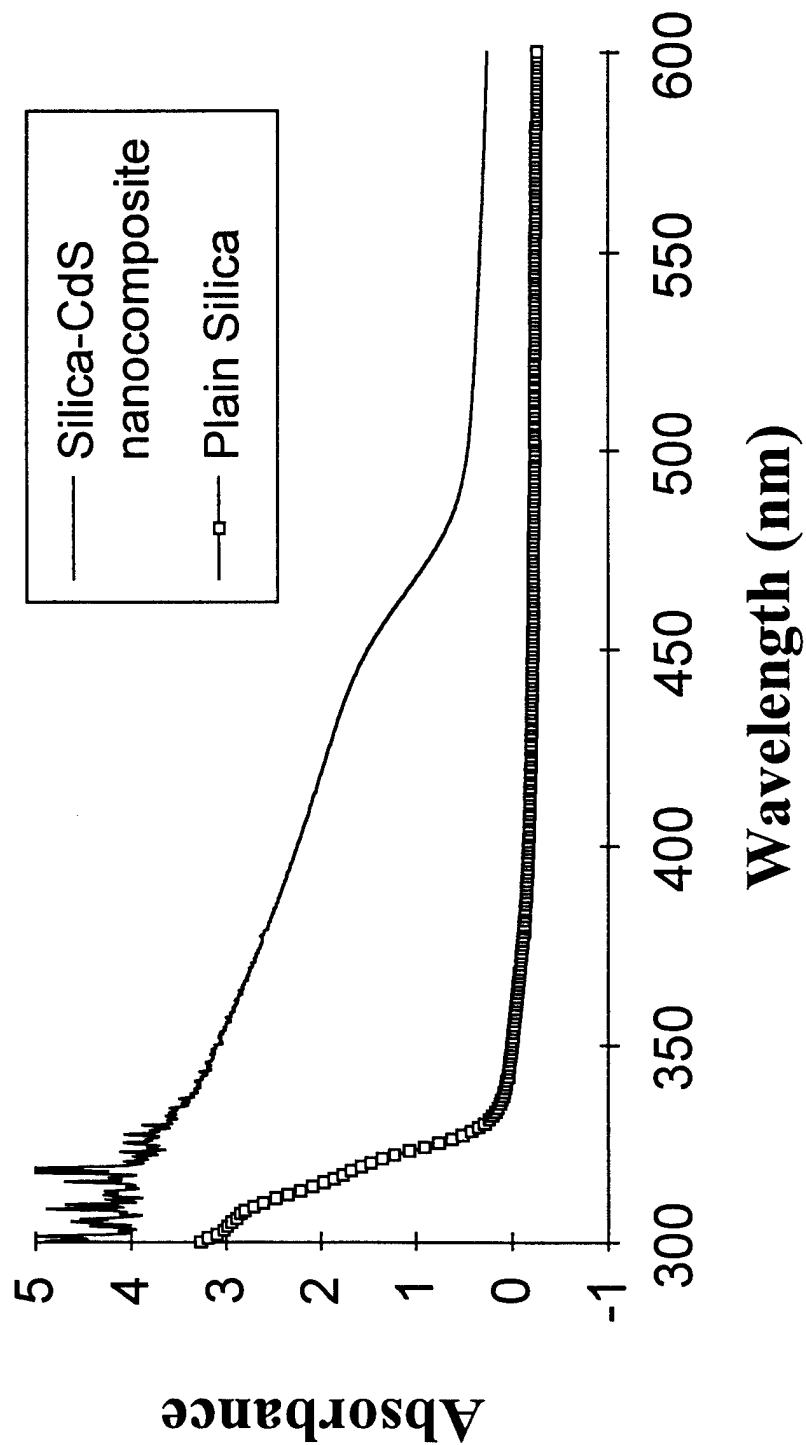
Figure 3.10.   UV-visible absorption spectrum for pure silica and silica–CdS nanocomposite spheres.

3.5 Conclusions

We have demonstrated new methods to grow silica-CdS sphere nanocomposites which allow us to produce particles with a variety of morphologies. We can easily modify the recipe to synthesize silica particles of various sizes. This process for forming monodisperse silica spheres between 30-150 nm is superior to the Stöber process because the uniformity is better and larger spheres can be grown by continuing the growth of previously grown small monodisperse silica spheres.

This synthesis in a water-in-oil microemulsion can be combined with the precipitation of other materials to form complex nanocomposites with complex morphologies. We demonstrate the production of homogeneously dispersed CdS quantum dot-silica sphere composites, as well as other composites where the CdS inclusions are larger and are situated either at the particle center or on the surface. In addition, the CdS particulates can be used to weld together the silica spheres to form dimers and trimers. The quantum dot composites are designed to be useful as new highly nonlinear optical materials. Our intention is to incorporate them into crystalline colloidal arrays for optical switching.

These nanocomposites can be further modified by the application of additional processing. The accompanying paper demonstrates the fabrication of new class of high surface area topologies in silica particles made by the etching removal of the CdS inclusions. These porous materials will be useful as a matrix for catalysis support applications.

3.6 References

1.   (a) Kroto, H. W.; Heath, J. R.; O'Brien, S. C.; Curl, R. F.; Smalley, R. E. *Nature* **1985**, *318*, 162. (b) Krätschmer, S.; Lamb, L. D.; Fostiropoulos, K.; Huffman, D. R. *Nature* **1990**, *347*, 354-358. (c) Krätschmer, W.; Lamb, L. D.; Fostiropoulos, K.; Huffman, D. R.; Mackay, A. L. *Ibid* **1990**, 336-337.

2.   Rossetti, R.; Brus, L. E. *J. Phys. Chem.* **1982**, *86*, 4470.

3.   Pileni, M. P.; Petit, C.; Zemb, T. *Chem. Phys. Lett.* **1985**, *118*, 414.

4.   Wang, Y.; Herron, N. *J. Phys. Chem.* **1991**, *95*, 525.

5.   Lianos, P.; Thomas J. K. *Chem. Phys. Lett.* **1986**, *125*, 299.

6.   Weller, H.; Schmidt, H. M.; Koch, U.; Fojtik, A.; Henglein, A.; Kunath, W.; Weiss, K. *Chem. Phys. Lett.* **1986**, *124*, 557.

7.   Tsaur, S. L; Fitch, R. M. *J. Coll. Int. Sci.*, **1987**, *115*, 450.

8.   El-Aasser, M. S.; Fitch, R. M. "Future Directions in Polymer Colloids", Nato ASI Series, Nijhoff Publishers, Dordrecht, **1987**.

9.   Matijevic, E. *Pure & Appl. Chem.* **1988**, *60*, 1479.

10. Asher, S. A. U.S. Patent # 4,627,689, **1986**, U.S. Patent # 4,632,517, **1986**.

11. Haacke, G.; Panzer, H. P.; Magliocco, L. G.; Asher, S. A. U.S. Patent # 5,266,238, **1993**.

12. Flaugh, P. L.; O'Donnell, S. E.; Asher, S. A. *Appl. Spectrosc.* **1984**, *38*, 847-850.

13. Asher, S. A.; Flaugh, P. L.; Washinger, G. *Spectroscopy* **1986** *1*, 26-31.

14. Rundquist, P. A.; Photinos, P.; Jagannathan, S.; Asher, S. A. *J. Chem. Phys.* 1989, *91*, 4932-4941.

15. Rundquist, P. A.; Kesavamoorthy, R.; Jagannathan, S.; Asher, S. A. *J. Chem. Phys.* **1991**, *95*, 1249-1257, 8546-8551.

16. Asher, S. A.; Kesavamoorthy, R.; Jagannathan, S.; Rundquist, P. SPIE Vol. 1626 Nonlinear Optics III, **1992**, 238-241.

17. Chang, S.-Y.; Asher, S. A. *J. Am. Chem. Soc.* **1994**, submitted.

18. Osseo-Asare, K.; Arriagada, F. J. *Colloids and Surfaces* **1990**, *50*, 321.

19. Stöber, W; Fink, A.; Bohn, E. *J. Coll. Int. Sci.* **1968**, *26*, 62.

20. Bogush, G. H., Tracy, M. A.; Dickstein, G. L.; Lee, P.; Zukoski, K. C.; Zukoski, C. F. *J. Non-Crys. Solids* **1988**, *104*, 95.

21. Wang, Y.; Suna, A.; McHugh, J.; Hilinski, E. F.; Lucas, P. A.; Johnson, R. D. *J. Chem. Phys.* **1990**, *92*, 6927.

22. Herron, N.; Wang, Y.; Eckert, H. *J. Am. Chem. Soc.* **1990**, *112*, 1322.

23. Smith, J. V. "X-Ray Powder Data File", Am. Soc. for Testing & Materials, **1967**, Philadephia.

24. Border, T. J.; Dubois, P. D. U. S. Patent 4,983,369, **1991**.

25. Van Helden, A. K.; Jansen, J. W.; Vrij. A. *J. Colloid Surface Sci.* **1981**, *81*, 354.

26. Jelinek, L.; Dong, P.; Rojos-Pazos, C.; Taibi, H.; Kovats, E. *Langmuir*, **1992**, *8*, 2152.

27. Weller, H.; Schmidt, H. M.; Koch, U.; Fojtik, A.; Baral, S.; Henglein, A; Kunath, W.; Weiss, K. *Chem. Phys. Lett.*, **1986**, *124*, 557.

28. Unger, K.; Giesche, H.; Kinkel, J. U.S. Patent # 4775520, **1988.**

4.0 Creation of Templated Complex Topological Morphologies in Colloidal Silica

4.1 Executive Summary

We have developed a new method to create complex monodisperse silicon dioxide particles which contain voids with unique morphologies. These particles are prepared from monodisperse silica spheres (ca 100 nm) which contain CdS inclusions organized as large patches on the silica sphere surfaces, or as small quantum dots within the spheres, or as interior spherical shells, or as the central cores of the silica spheres. We create voids with the identical morphology as the CdS inclusions by etching out the CdS inclusions with strong acid. The silica sphere-CdS composite particles are prepared within a microemulsion reaction medium as described in the accompanying paper. The etched silica particles have either craters on their surface, 2.4 nm diameter spherical voids dispersed within the silica spheres, hollow cores, or hollow shells separating silica shells from silica cores. In addition, we have formed unique ellipsoidal cavities within doublets of silica spheres. These doublets were formed through the attachment of silica spheres by CdS patches on the silica surfaces. A silica shell was subsequently grown around the sphere doublets. Etching away the CdS results in ellipsoidal caverns connecting the two spheres of each doublet. These high surface area materials have geometrically tailorable voids and may prove useful as novel catalyst support media.

4.2 Introduction

One major frontier of chemical synthesis is the development of novel methodologies to create tailor-made complex morphologies within macromolecular complexes. The argument is that these complex morphologies can be used for creating sophisticated chemical processes where an assembly line of chemical reactions can be linked within connected regions of

macromolecular entities. In the accompanying paper[1] in this issue we described the microemulsion synthesis of ca 40-300 nm monodisperse silica-CdS colloids, where the CdS inclusions were incorporated within porous silica spheres. These inclusions were synthesized to be either quantum dots uniformly dispersed in the silica spheres, or as large surface caps, or as surface quantum dots, or as cores of CdS surrounded by silica shells, or as a set of concentric spherical shells of silica, CdS, silica, *etc.*, i.e. multidecker sandwiches.

We describe here a method to further process these nanocomposite spheres in order to form complex voids within the silica colloids. This processing forms voids identical in shape and volume to the original CdS inclusions by quantitatively etching out the CdS inclusions. For the homogeneously dispersed quantum dots, this results in numerous small (ca 2.5 nm) spherical voids, while the CdS core-silica sphere composites yield silica spheres with spherical voids at their centers. More complex annular voids are formed from the silica-CdS shells, while craters are formed from the silica spheres with surface CdS patches.

Numerous other research groups are also developing approaches to create complex nanostructure morphologies in various materials. For example, a number of groups have prepared hollow inorganic powders by dehydration and decomposition of aerosol particles, or through the removal of solvent from the interior of particles. However, these approaches do not permit careful control of the void sizes and shapes.[2-4] Matijevic's group has prepared hollow particles by the thermal decomposition of the polymer cores of particles prepared such that a polymer core was overcoated by a shell of thermally stable inorganic material.[5]

Our approach described here[1] allows us to create these voids at room temperature; in addition, our silica particles contain voids within pure silica cavities. These cavities can be further modified using the standard chemical approaches for silica surfaces. We expect that the approach outlined here, is of general utility, and can easily be extended to other materials such as titania and alumina, for example. We expect that these porous materials with well

defined voids will find utility in areas of technology such as catalysis, for example.

4.3 Experimental

The detailed procedures for preparing the CdS-silica nanocomposites are given in the accompanying paper.[1] Typically, a reaction utilized a 250 ml microemulsion containing 0.127-0.184 M of NH_3, 0.086-0.537 M of Igepal CO-520 or Triton N-101, 0.053-0.179 M of tetraethyl orthosilicate (TEOS, Fluka) with the remainder of the reaction mixture consisting of cyclohexane and hexanol.

Nanocomposite colloids of silica-CdS were synthesized using either Igepal or Triton microemulsions containing Cd^{2+} and S^{2-} ions. The CdS inclusions were implanted through the precipitation of CdS during the simultaneous condensation of silica due to the simultaneous injection of TEOS. The resulting yellow nanocomposites were solvent exchanged into water and washed several times with concentrated nitric acid until the yellow CdS inclusions were completely dissolved and the turbid solution became white. The final product was a pure colloidal silica suspension. Surface areas were measured by using the BET nitrogen absorption method (Automatic Surface Area Analyzer 4200, Beta Scientific Corp.).

4.4 Results and Discussion

As indicated in the preceding paper,[1] CdS inclusions can be incorporated in monodisperse silica spheres in a variety of morphologies. These morphologies are determined by the timing and the precipitation rate of the CdS during the growth of the silica spheres in the microemulsion reaction medium. As indicated schematically in Figure 4.1, the CdS inclusions can be prepared as large patches on the surface, or as uniform quantum dot inclusions within the spheres, or as the cores of the silica particles, or as annular shells within a silica-CdS sandwich arrangement, or as small quantum dots on the surface.
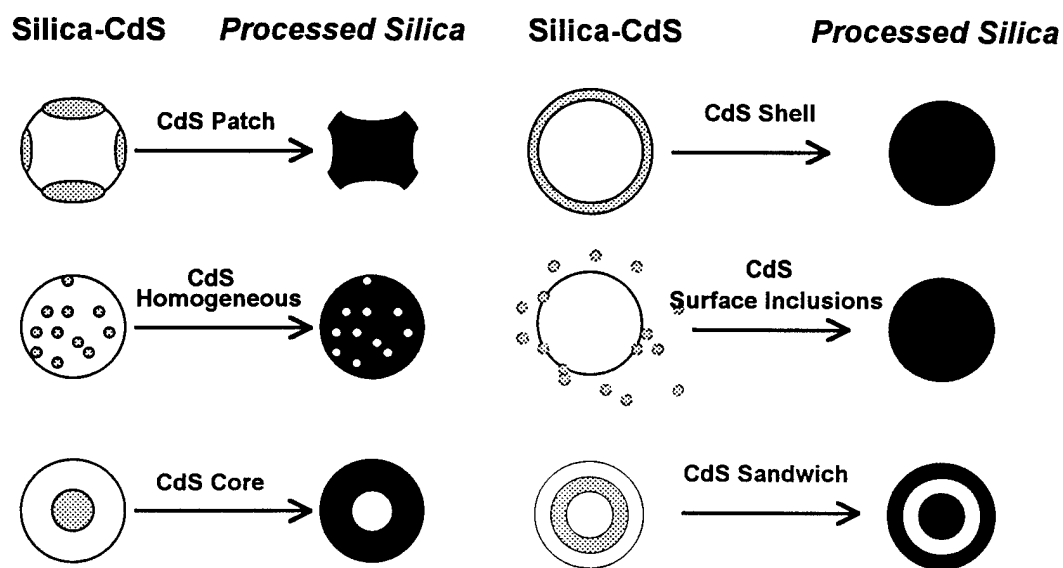
Figure 4.1.   Schematic diagram illustrating the various silica-cadmium sulfide nanocomposites

that can be synthesized, and the resulting particle formed after the acid etching removal of

the CdS inclusions.

Pure silica does not react with strong acids except for HF. In contrast, CdS is very soluble in strong acids, which readily dissolve the CdS inclusions. Figure 4.2a and 4.2b show a CdS-silica nanocomposite with CdS patches on the surface before and after acid etching; acid etching forms craters on the surface.

Figure 4.3 shows a TEM micrograph of ca 50 nm CdS-silica nanocomposite spheres with homogeneously dispersed CdS quantum dots after acid etching. The figure demonstrates numerous dimples on the surface. It is difficult to clearly visualize the interior small 2.5 nm voids by TEM. However, the fact that the sample is no longer yellow, indicates that the interior CdS inclusions have been removed. Further, the BET surface area measurements discussed below demonstrate that the particles contain numerous ca 2.5 nm diameter spherical cavities.

Acid etching of ca 30 nm silica colloids which originally contained 4-8 nm CdS cores results in central voids. Our acccompanying paper shows a TEM photograph of this preparation after acid etching. The dark central spots result from the small hollow spherical voids. We also can create larger spherical cavities. Figure 4.4 shows hollow ca 90 nm particles with ca 30 nm diameter holes. We can easily construct silica colloids with diameters as large as 300 nm with hollow cores of any size desired.

Figure 4.5 shows acid etched doublets of silica spheres. These doublets were formed through the attachment of silica particles by welds of CdS surface patches. Subsequently a silica shell was formed around the sphere doublets. Acid etching results in ellipsoidal cavities where the CdS welds between the spheres were removed to form ellisoidal caverns joining the spheres.

We directly measured the increase in the sample surface area by BET nitrogen absorption measurements after acid etching. Table 4.1 shows the measured surface areas and that calculated using simple models for samples SYC121Q and SYC122Q where the CdS was

80 nm

Silica-CdS
M90288

b.

a.
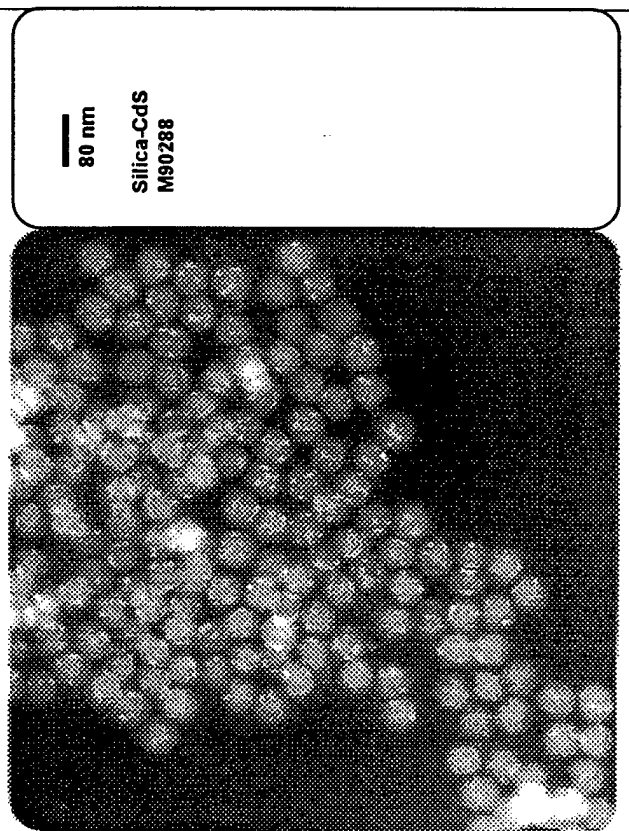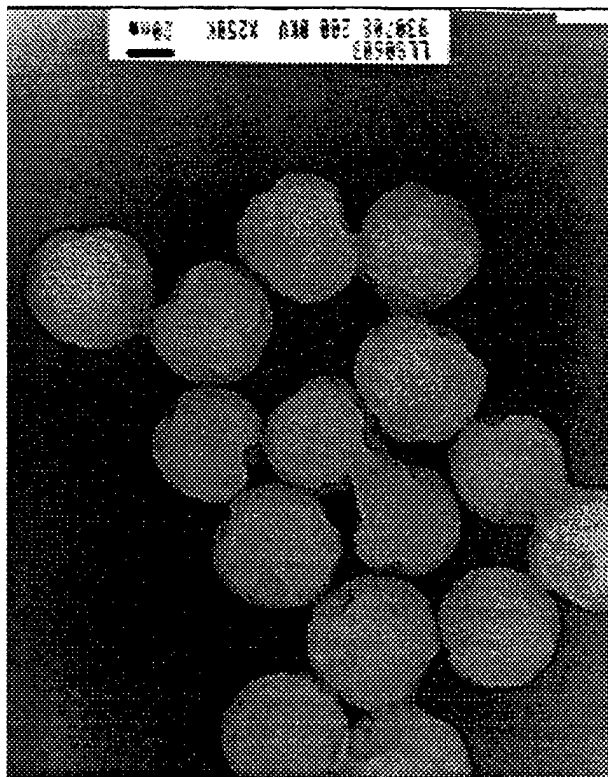
Figure 4.2.   a) TEM micrographs of nanocomposite particles with cadmium sulfide surface patches before nitric acid etching. b) TEM micrographs after etching: the bare silica particles show craters on the surface where the cadmium sulfide patches were removed.
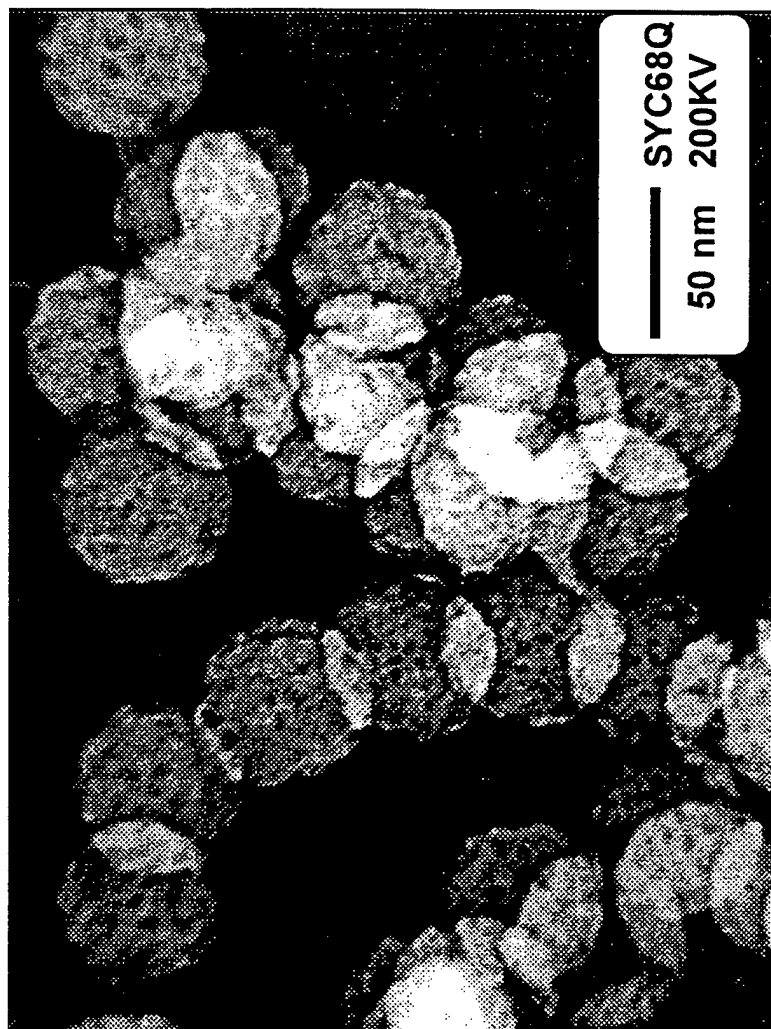
Figure 4.3. TEM micrographs of nanocomposite particles with cadmium sulfide quantum dots homogeneously distributed after etching; the bare silica particles show dimples where the cadmium sulfide quantum dots were removed on the surface. The interior voids cannot be clearly visualized.
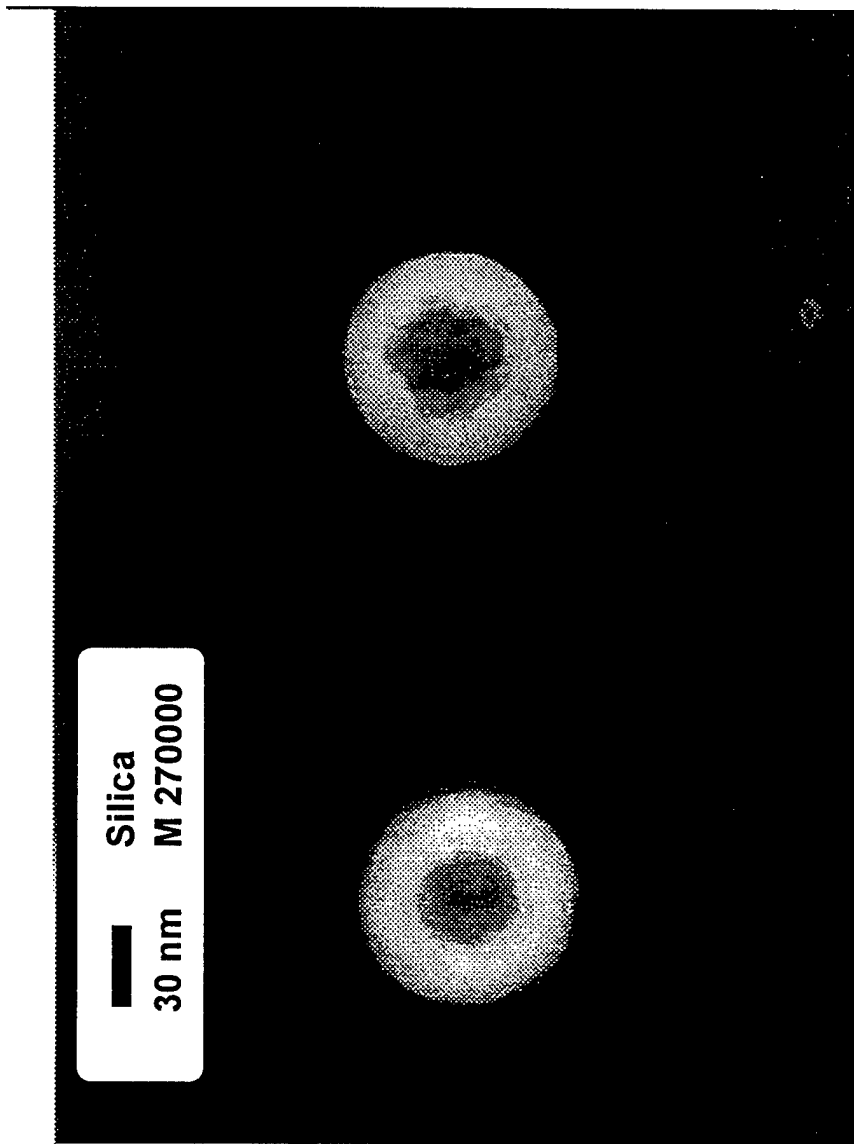
Figure 4.4.   TEM micrograph of spheres where large <u>ca</u> 30 nm CdS cores were removed by acid etching to leave large spherical voids.
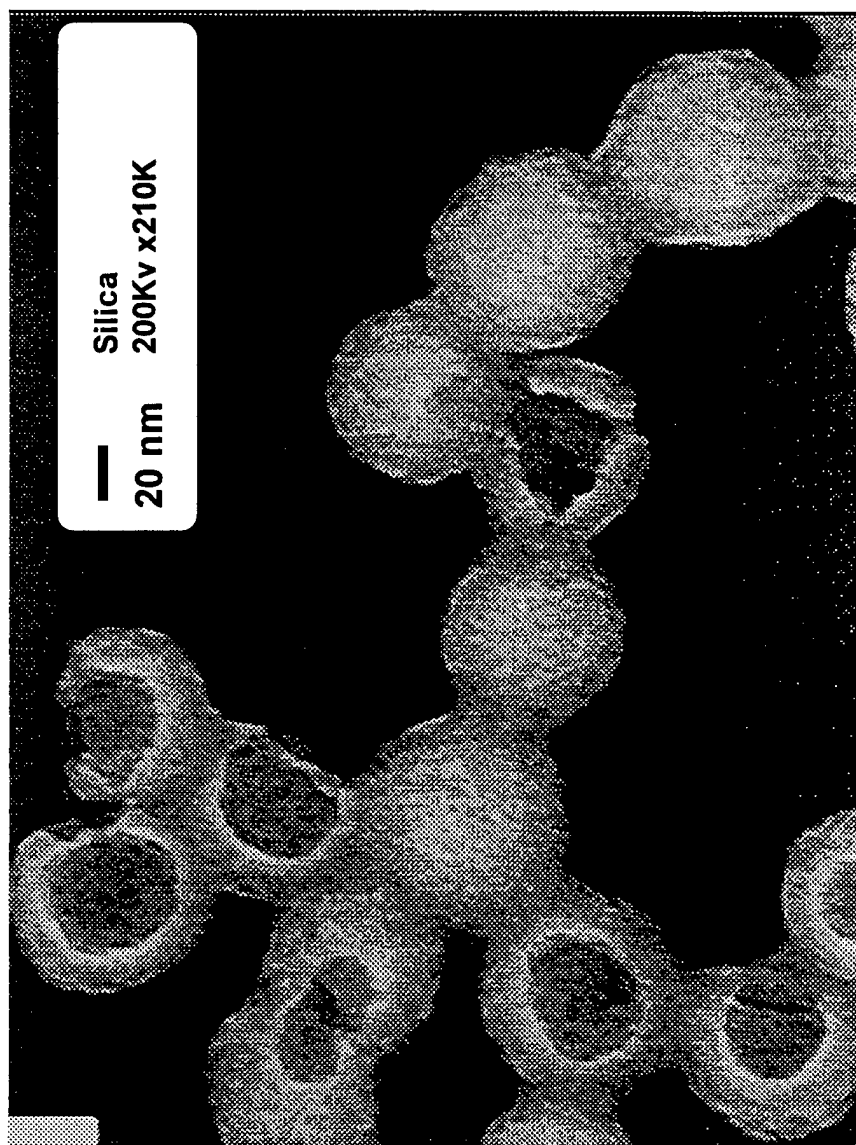
Figure 4.5.   TEM micrograph of silica sphere doublets after acid etching. These doublets were formed during the synthesis of silica spheres with CdS patches.1 The doublets are attached at CdS welds and the doublets are overcoated with silica shells.   Acid etching of the doublets resulted in ellipsoidal caverns joining the sphere doublets.

Table 4.1. Calculated and measured BET surface areas for silica-CdS composite spheres before and after acid etching.

sample	particle morphology	particle size (nm)	surface area (m²/g)			
			measured, before etching	measured, after etching	calculated, before etching[*]	calculated, after etching[*]
SYC121Q	shell, +doublets and triplets	80	61	232	39	169
SYC122Q	shell, +doublet and triplets	84	76	208	37	179
SYC68Q	raisin bread	62	104	152	51	102

[*] Ignoring aggregates and assuming density of 1.9 g/cm³.

formed as annular rings within the silica spheres and sample SYC68Q where CdS quantum dots were homogeneously distributed in the silica spheres. The samples with the CdS annular shells had large concentrations of doublet and triplet spheres.

If the spheres are non porous we can calculate that he surface area, A (m²/gm) of the silica sphere-CdS composites is simply the surface area of the spherical particles.

$$A = 6000 \, W/d \, \rho$$

where W is the weight of the sample (1.0 gm), d is the sphere diameter (nm) and ρ is the density (gm/cm³) of the silica-CdS sphere composites.

We see that prior to etching the area measured is approximately two-fold greater that calculated. The larger surface area of the sample probably results from pores within the silica spheres; silica colloids made by the Stöber process are often highly porous[1,6] with porosities as large as 11-15%. However, varying the preparation conditions can dramatically decrease the porosity.[7,8] The silica-CdS composite spheres prepared here appear to be much less porous than the highly porous Stöber silica spheres. The surface areas associated with the pores can be very large, depending on the pore diameters. For example, 10% porous 80 nm silica spheres with 0.4 nm diameter pores are calculated to show surface areas greater than 600 m²/gm. Our silica-CdS composite samples show silica sphere internal surface areas ten-fold smaller. However, our silica-CdS composite spheres are at least somewhat porous since the entire particle volume is readily accessible to chemical reagents such as nitric acid which dissolves the CdS.

After etching the surface area increases three to four-fold for samples SYC121Q and SYC122Q and by 50% for sample SYC68Q. For samples SYC121Q and SYC122Q we modeled the increase in surface area to be that associated with the surface area of the void shell that originally contained CdS. For sample SYC68Q the surface area increase calculated was that which resulted from the 2.4 nm spherical voids formed by removal of the CdS quantum

dots in the spheres.

$$A_c = 6000 \; W \; R \; / \rho_c \; d_c.$$

where A_c is the surface area which results from the voids created by removal of the CdS quantum dots, R is the weight ratio of CdS to silica (R=0.105 for sample SYC68Q), ρ_c is the density of CdS, and d_c is the diameter of the voids (2.4 nm).

The measured increases in surface are very close to that calculated from the simple models. This result supports the idea that we have tailored voids in the silica spheres which are geometrically well defined in size and shape and in their location within the silica spheres.

4.5 Conclusions

We have demonstrated a new method to form silica particles with voids of a variety of morphologies. The relative amounts, sizes and positions can be easily and accurately controlled. These monodisperse silica spheres are porous and additional chemistry can be used to further modify the cavity surfaces. These materials will be useful for catalyst support applications and for novel other applications where it is important to carry out chemical reactions in separate small chambers.

4.6 References

1. Chang, S. Y.; Liu, L.; Asher, S. A. *J. Am. Chem. Soc.* **1994**, *116*, 6739.

2. Roth, C. and Kobrich, R. *J. Aerosol Sci.* **1988**, *19*, 939.

3. Durand-Keklikian, L.; Partch, R. E. *J. Aerosol Sci.* **1988**, *19*, 511.

4. Ramamurti, M.: Leong, K. J. *J. Aerosol Sci.* **1987**, *18*, 175

5. Kawakashi, N.; Matijevic, E. *J. Colloid Int. Sci.* **1991**, *143*, 103.

6. Bogush,G. H.; Tracy, M. A.; Dickstein, G. L.; Lee, P.; Zukoski, K. C. ; Zukoski, C. F. *J. Non-Crys. Solids* **1988**, *104*, 95.

7. Border, T. J.; Dubois, P. D., U. S. Patent 4,983,369, **1991**.

8. Van Helden, A. K.,; Jansen, J. W.; Vrij, A. *J. Colloid Int. Sci.* **1981**, *81*, 354.

5.0 Polymerized Crystalline Colloidal Arrays

5.1 Executive Summary

We demonstrate a technique to create solid submicron periodic materials called polymerized crystalline colloidal arrays (PCCA). Monodisperse colloidal particles synthesized with numerous surface ionizing groups form macroions when dispersed in polar media such as water, methanol, etc. The electrostatic repulsions between particles, that occur at high particle concentrations, cause these concentrated colloidal dispersions to self assemble into a face centered or a body centered cubic periodic lattice known as a crystalline colloidal array (CCA). These CCA efficiently Bragg diffract light and have recently been utilized for optical devices such as band rejection filters. We demonstrate here a new method to permanently polymerize the CCA lattice ordering into an ordered hydrogel network. The polymerized CCA is rugged and can be used for frequency agile filters. This solidified array can also be chemically modified to create rigid solid periodic materials for different applications.

5.2 Introduction

We wish to report the development of a method for creating new submicron periodic materials. These materials will have numerous applications in various areas of technology. This periodic material is composed of a body centered cubic (BCC), face centered cubic (FCC) or random hexagonal stacked array of spherical particles in which the periodicity is locked into a hydrogel polyacrylamide network.[1] The lattice constant of this array can be varied between ca 10 nm to greater than 1 μm. The particles are generally monodisperse polymer or

inorganic spheres with diameters smaller than the lattice constant of the array. The volume

percent of particles can be made as large as ca 75% or smaller than 1%.

The periodic array forms through the electrostatic self assembly of charged colloidal

particles. It is well known that submicron periodic ordered structures called crystalline

colloidal arrays (CCA) will self-assemble from monodisperse colloidal spheres containing

surface functional groups that ionize in solution.[2-5] If these spheres are dispersed in a polar

medium such as water, the surface groups ionize to form spherical macroions which are

surrounded by a diffuse counterion cloud. If the solution medium is pure and contains few

other ionic species the repulsive interaction between spherical macroions can be significant

over macroscopic distances greater than 1 μm.[6-8] For high particle concentrations

($> 10^{13}$/cm^3) significant interparticle repulsion occurs at the average interparticle spacing; the

minimum energy configuration for the assembly of spherical macroions is a BCC or FCC

crystal structure.

Monodomain CCA arrays can be made very large; these well ordered crystalline arrays

efficiently Bragg diffract light.[2] Our group has developed techniques to grow large, thin

single crystals of these arrays for use as Bragg diffraction devices.[2,9] For example, Figure 5.1

shows diffraction from a CCA composed of 150 nm polystyrene spheres with a particle

concentration of 9.4×10^{13} spheres/cc, which corresponds to a volume fraction of 8.3%. These

spheres were made by emulsion polymerization of styrene with divinyl benzene as a cross

linker and 1-allyloxy-2-hydroxy propane sulfonate (COPS-1) as an ionic monomer. Each

sphere contains 7600 ionizing sulfonate groups. The Bragg diffraction at 525 nm occurs in the
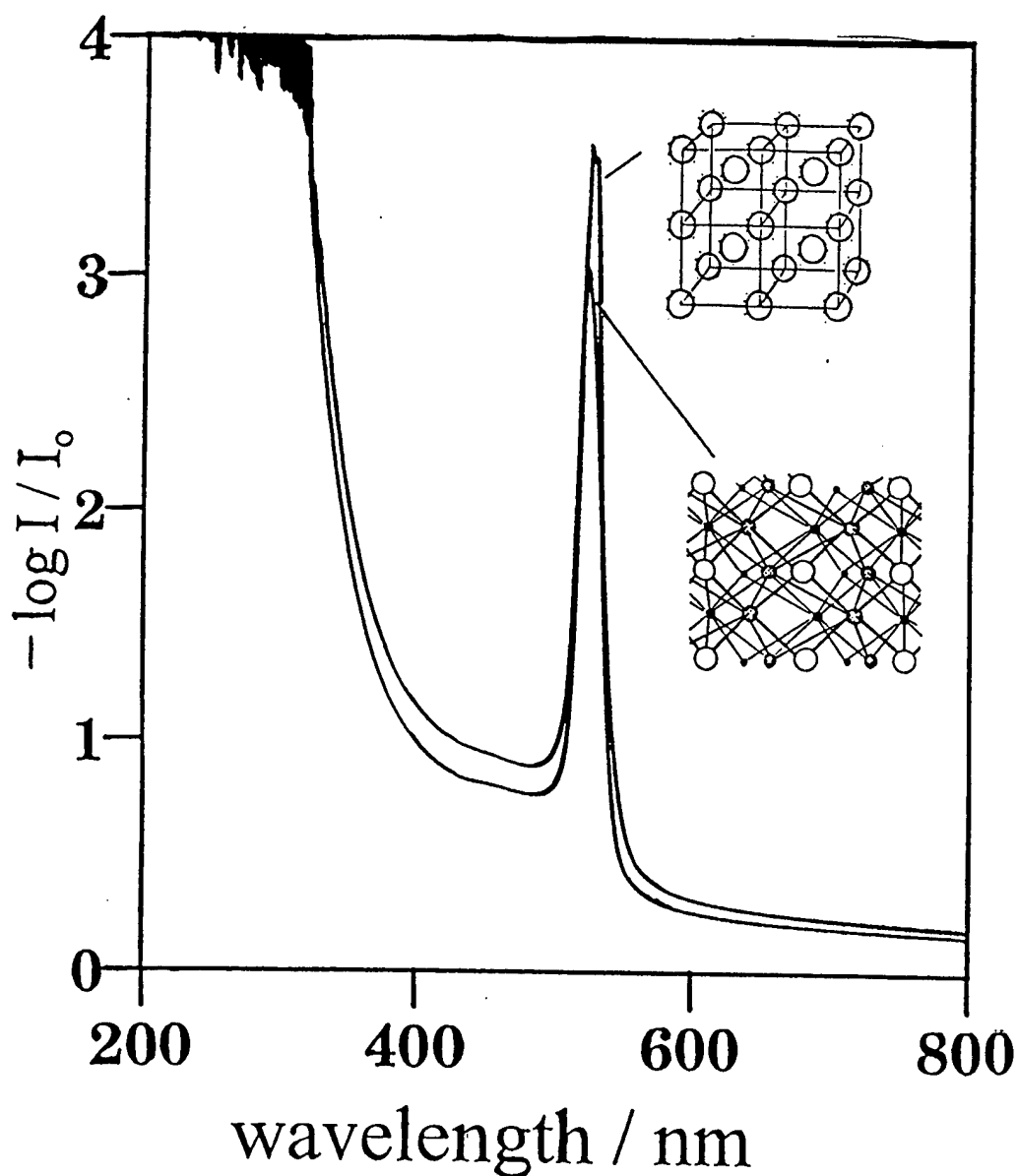
Figure 5.1. Extinction spectra of a liquid crystalline colloidal array (CCA) and a polymerized crystalline colloidal array (PCCA). The CCA and PCCA were composed of 150 nm polystyrene spheres with surface sulfonate groups in a liquid medium containing 50% N-vinyl pyrrolidone, 17% acrylamide, 4.5% N,N' methylene bisacrylamide and 1% benzoin methyl ether. The similarity of the diffraction peaks of the CCA and the PCCA indicate that little disturbance of the array occurred upon polymerization. The refractive index of the system is ca 1.44.

dynamical diffraction regime and almost follows the classical Bragg's law:[9]

$$\lambda_o = 2 \, n \, d \sin \theta$$

where λ_o is the wavelength of light in vacuum, n is the refractive index of the medium, d is the plane spacings and θ is the Bragg glancing angle.

These liquid phase CCA are stable, but will transiently disorder under shock. The CCA will also disorder upon introduction of ionic impurities which screen the interparticle repulsive interactions. Thus, their long term stability depends upon cleanliness of their environment and their containers.

5.3 Experimental

We have developed an approach to permanently lock in the CCA array ordering in a solid matrix. We introduce into the CCA highly purified nonionic polymerizable monomers that can form a hydrogel network around the CCA spheres. For example, we form a solid CCA matrix by introducing highly purified acrylamide, N,N'-methylene bis acrylamide and N-vinylpyrrolidone into the CCA solution, and use UV light to excite benzoin methyl ether to initiate the polymerization.

A typical recipe for polymerizing the array is as follows:

        3.00 g of diffracting colloidal suspension
        3.00 g N-vinyl pyrrolidone (monomer)
        1.30 g of acrylamide (monomer)
        0.34 g N,N' methylene bis acrylamide (crosslinker)
        0.07 g benzoin methyl ether (photoinitiator)

The monomers are added one at a time to the difracting colloidal suspension. Ion exchange resin is added, and the mixture is shaken until diffraction reappears. The initiator is added

last, and the mixture is injected into a cell consisting of two quartz plates separated by a parafilm spacer 150-300 μm thick. The cell is then exposed to UV radiation for 10 minutes.

5.4 Results

This liquid polymerized CCA (PCCA) forms a solid hydrogel which locks in the CCA periodic order; the CCA will remain stable in the presence of these polymerizable species provided that the monomers do not contain ionic impurities. The CCA polymerization results in only modest changes in the CCA ordering as evidenced by the modest alterations of the diffraction peak (Fig. 5.1). The hydrogel film is very stable; addition of solute does not perturb the array ordering since the lattice order no longer depends upon electrostatic interactions between spheres.

The PCCA hydrogel film formed is elastic and contains 30% vol water. Stretching the gel causes the diffraction peak wavelength to decrease in response to a decrease in the layer spacing;[10] the layer spacing along the film normal decreases as the film is stretched (Fig. 5.2).

The water medium in the film can be replaced by other materials without changing the CCA ordering. For example, in our work[11] on developing optical limiters we have used benzyl alcohol to refractive index match a PCCA made from polymethylmethacrylate spheres and hydrogel network above. Although the periodic order is maintained, the refractive index-matched system does not Bragg diffract light. However, any perturbation which alters the relative refractive index between the spheres and the medium causes the array to diffract light; the device becomes an optical limiter.

The liquid medium of the PCCA can also be replaced by a polymerizable monomer or
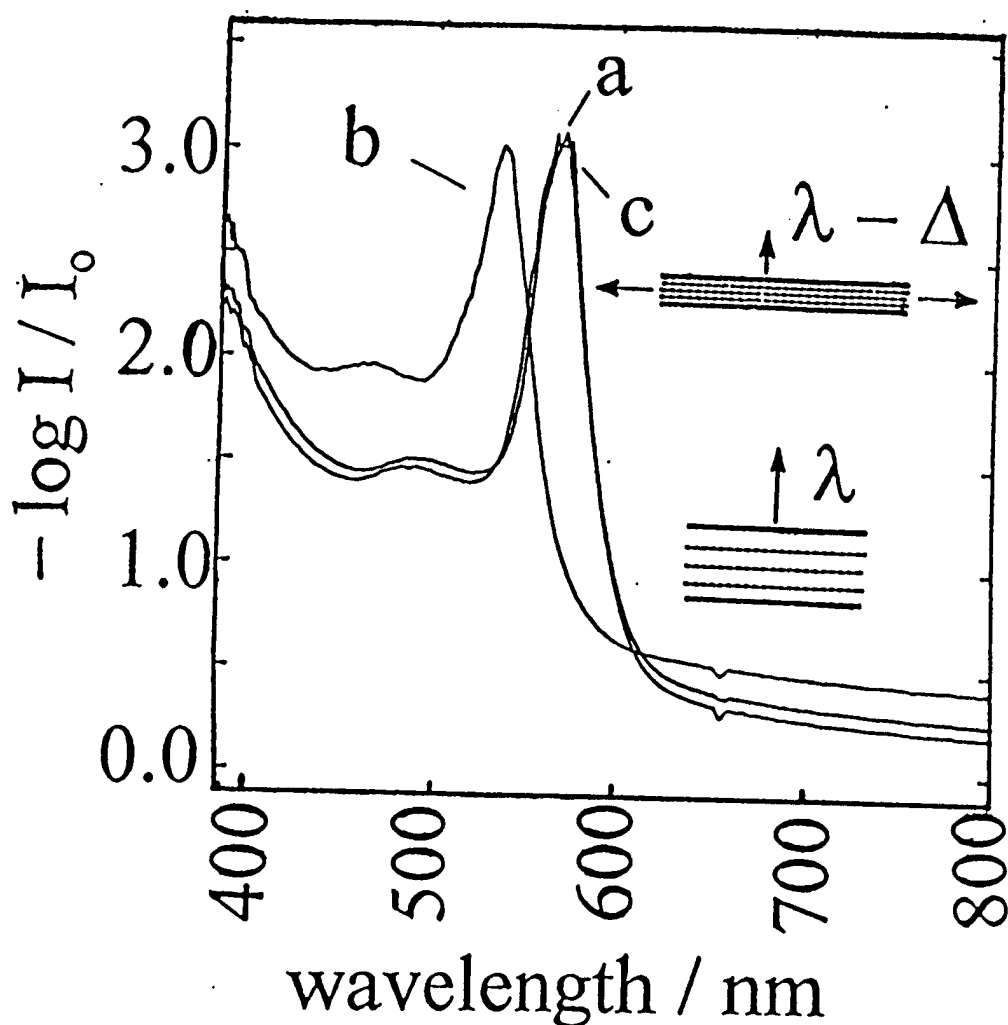
Figure 5.2. (a) Extinction spectra of a polymerized crystalline colloidal array (PCCA) composed of 170 nm colloidal particles polymerized in a hydrogel composed of 50% N-vinyl pyrrolidone, 6% acrylamide, and 1% N,N' methylene bisacrylamide. The PCCA shows a diffraction maximum at 573 nm. (b) Extinction spectrum of the PCCA during a uniaxial strain in the plane of the film; the diffraction maximum shifts down to 538 nm due to the decrease in the interplane distances. (c) Extinction spectrum of the PCCA after the stress was relieved. The PCCA again shows a diffraction maximum at 573 nm.

inorganic glass precursor. Polymerization or condensation of this system results in a rigid film which contains the submicron periodic structure. The shape remains identical to that of the original PCCA film.

5.6 Discussion

The work here demonstrates a motif for preparing solid submicron periodic systems out of a variety of materials. The only requirement is that the spherical particles must be monodisperse and possess numerous surface ionizing groups. Monodisperse spheres can be prepared from both organic and inorganic materials. Emulsion polymerization can be used to synthesize monodisperse polymer spheres from polystyrene, polymethylmethylmethacrylate and fluorinated polymer materials, etc.[12] Monodisperse inorganic materials can synthesized using techniques such as the Stöber process[13] and microemulsion synthesis.[14] Electrostatic self assembly creates a CCA periodic array with a wide variety of possible lattice constants from colloidal particles with a wide variety of particle diameters.

5.7 Conclusions

These systems will have numerous applications in technology. For example, they will be useful as optical filters[2a] and optical limiters[11a,11b] and variable mechanically controlled wavelength rejection filters.[10]

5.8 References

1.   Asher, S. A.; Jagannathan, S. U.S. Patent No. 5,281,370 (1994).

2.   (a) Asher, S. A. U.S. Patents Nos. 4,627,689 and 4,632,517; (b) Kesavamorthy, R.; Jagannathan, S.; Rundquist, P. A.; Asher, S. A. *J. Chem. Phys.* **1991**, *94*, 5172-5179; (c) Rundquist, P. A.; Kesavamoorthy, R.; Jagannathan, S.; Asher, S. A. *J. Chem. Phys.* **1991**, *95*, 1249-1257; (d) Kesavamoorthy, R.; Tandon, S.; Xu, S.; Jagannathan, S.; Asher, S. A. *J. Coll. Int. Sci.* **1992**, *153*, 188-198; (e) Rundquist, P. A.; Jagannathan, S.; Kesavamoorthy, R.; Brnardic, C.; Xu, S.; Asher, S. A. *J. Chem. Phys.* **1990**, *94*, 711-717; (f) Carlson, R. J.; Asher, S. A. *Appl. Spectrosc.* **1984**, *38*, 297-304; (g) Asher, S. A.; Flaugh, P. L.; Washinger, G. *Spectroscopy* **1986**, *1*, 26-31; (h) Flaugh, P. L.; O'Donnell, S. E.; Asher, S. A. *Appl. Spectrosc.* **1984**, *38*, 847-850.

3.   (a) Krieger, I. M.; O'Neill, F. M. *J. Am. Chem. Soc.* **1968**, *90*, 3114; (b) Hiltner, P.A.; Krieger, I. M. *J. Phys. Chem.* **1969**, *73*, 2386-2389; (c) Hiltner, P. A.; Papir, Y. S.; Krieger, I. M. *J. Phys. Chem.* **1971**, *75*, 1881-1836.

4.   (a) Clark, N. A.; Hurd, A. J.; Ackerson, B. J. *Nature* **1979**, *281*, 57-60; (b) Ackerson, B. J.; Clark, N. A. *Phys. Rev. Lett.* **1981**, *46*, 123; (c) Aastuen, D. J. W.; Clark, N. A.; Cotter, L. K.; Ackerson, B. *J. Phys. Rev. Lett.* **1986**, *57*, 1733; (d) Hurd, A. J.; Clark, N. A.; Mockler, R. C.; O'Sullivan, W. *J. Phys. Rev. A.* **1982**, *26*, 2869.

5.   Monovoukas, Y.; Gast, A. P. *J. Colloid Interface Sci.* **1989**, *128*, 533-548.

6.   (a) Derjaguin, B.; Landau, L. *Acta Physicochim URSS* **1941**, *14*, 633; (b) Verwey, E. J. W.; Overbeek, J. G. *Theory of the Stability of the Lyophobic Colloids,*; Elsevier, Amsterdam, 1948.

7.   (a) Russel, W. B.; Saville, D. A.; Schowalter, W. R. *Colloidal Dispersions*; Cambridge Univ. Press: Cambridge, 1989; (b) Hiemenz, P. C. *Principles of Colloid and Surface Chemistry*; Marcel Dekker: New York, 1986.

8.   Sood, A. K. In *Solid State Physics*; Ehrenreich, H.; Turnbull, D., Eds., **1990**, *43*, 1.

9.   Rundquist, P. A.; Photinos, P.; Jagannathan, S.; Asher, S. A. *J. Chem. Phys.* **1989**, *91*, 4932-4941.

10.   Haacke, G.; Panzer, H. P.; Magliocco, L. G.; Asher, S. A. U.S. Patent No. 5,266,238 (1993).

11.   (a) Asher, S. A.; Kesavamoorthy, R.; Jagannathan, S.; Rundquist, P. *SPIE Vol. 1626 Nonlinear Optics III*, **1992**, 238-241; (b) Kesavamoorthy, R.; Super, M. S.; Asher, S. A. *J. Appl. Phys.* **1992**, *71*, 1116-1123.

12.   Matijevic, E. *Langmuir* **1986**, *2*, 12.

13.   Stöber, W.; Fink. A; Bohn, E. *J. Coll. Int. Sci.* **1963**, *26*, 62.

14.   Chang, S.-Y.; Liu, L.; Asher, S. A. *J. Am. Chem. Soc.* **1994**, *116*, 6739.

6.0 Synthesis of Dyed Monodisperse Poly(methyl methacrylate) Colloids for the Preparation of Submicron Periodic Light Absorbing Arrays

6.1 Executive Summary

We have developed a method to synthesize highly charged, monodisperse <u>ca.</u> 100 nm poly(methyl methacrylate) (PMMA) colloidal particles containing covalently linked absorbing dyes. We acylate these dyes with methacryloyl chloride and add these functionalized dyes during an oil-in-water emulsion polymerization of the PMMA colloids. The high charge was obtained by copolymerizing with the ionic sulfonated surfactant COPS-1. After purification these monodisperse colloids spontaneously self-assemble into crystalline colloidal arrays (CCA). We utilize this colloid to fabricate an ordered array of absorbing colloidal spheres locked into a hydrogel matrix. We exchange the water in the medium to approximately match the real part of the array refractive index. This forms a novel submicron periodic system where a BCC array of absorbers interact with electromagnetic radiation with little scattering or diffraction of the incident light.

6.2 Introduction

Monodisperse colloidal particles have many applications in numerous areas of technology and the physical and biomedical sciences. They are used as calibration standards for electron microscopy, as model systems in light scattering and small angle neutron scattering, and for studies of rheology of dispersions and aerosol research. Monodisperse latex particles have also been extensively employed in various diagnostic tests, in vitro immunoassays, bone marrow transplantations, drug delivery systems, flow cytometry standards, and media for cell and protein separations.[1-3]

Numerous synthetic methods have been described to prepare monodisperse charged particles of organic polymers such as polystyrene[4-7] and poly(methyl methacrylate) (PMMA)[8-10] and inorganic

colloids such as silica.[11-12] Numerous other approaches exist to form monodisperse colloids of unique shapes for a variety of applications.[13]

Our interest in monodisperse colloidal particles is centered on using their novel self-assembly processes to form crystalline colloidal arrays (CCA) which Bragg diffract light.[14-18] Highly charged monodisperse colloids strongly electrostatically repel one another when their spacings occur within a Debye layer length (<1 μm). Concentrated colloidal dispersions (>10^{13} particles/mL) in deionized water show interaction potentials greater than kT; the lowest energy state of the system is where the particles self-assemble into a CCA which is in a BCC or FCC crystal structure. The spacing of the array is comparable to visible and near IR light and, thus, strong Bragg diffraction occurs from the arrays. We have utilized these CCA as Bragg diffraction filters for spectroscopic applications.[19,20]

We have proposed that these CCA can be used for optical switching and optical limiting applications. The idea is to match the real part of the refractive index of nonlinear colloidal particles such that at normal light intensities no scattering or Bragg diffraction occurs from the array.[21,22] However the particles in the array are synthesized to have large optical nonlinearities, and at high light intensities the refractive index of the particles diverges from that of the medium; the CCA array "pops up" to diffract the high intensity incident light. We have calculated that refractive index differences as small as 0.01 would permit the switch to operate efficiently.

The required colloidal particle nonlinearities exceed that of most known materials. Two possible approaches exist. We can utilize the large nonlinearities of cadmium sulfide (CdS) quantum dots[23] or we can use the larger nonlinear phenomena associated with thermal processes. We recently theoretically investigated the utility of using absorbing spheres to transfer energy from an intense

incident beam to heat the colloidal particles to alter the particle refractive index.[21]   Our calculations

indicate that nanosecond switching should occur for incident powers of 10 MW/cm^2.

In the work here we describe a general method to synthesize highly charged, monodisperse <u>ca</u>

100 nm poly(methyl methacrylate) (PMMA) colloidal particles containing covalently linked absorbing,

nonfluorescent dyes. This work follows our earlier studies of polystyrene colloids physically mixed with

the disazo dye Oil Red O to study photothermal compression[24], thermal diffuse scattering[25] and

collective diffusion[26] of CCA. However, our application required the covalent dye linkage because the

nonlinear colloids are in a more hydrophobic medium than water where the physisorbed dyes are

soluble and would partition out of the spheres into the medium.

Other examples have been reported for covalent attachment of dyes to monodisperse particles.

For example, Bhattacharyya and Halpern[2] reported the covalent attachment of fluorescent moieties to

monodisperse latex particles without providing experimental details. Winnik and coworkers[27] prepared

fluorescent-labeled PMMA latexes by semi-continuous emulsion polymerization.   These dyes

possessed either vinyl or methacryloyl groups. Peterson[28] was issued a patent for the process of

copolymerizing acrylamide with a pH-indicating dye such as phenol red to form a macroscopic

hydrophilic copolymer. Lyophilized polystyrene spheres were then mechanically mixed with the dried

dyed polyacrylamide spheres to fabricate fiber optic pH probes.

6.3 Experimental

The dyes 4-[ethyl(2-hydroxyethyl)amino]-4'-nitroazobenzene (Disperse Red 1, Colour Index

(CI) 11110), and 1,4-bis(pentylamino)-9,10-anthraquinone (Oil Blue N, CI 61555) were obtained from

Aldrich Chemical Company and used as received (Figure 6.1). The dye acylation procedure followed

that of Loucif-Saïbi, et al..[29] A mixture of 0.30 g of dye, 5 mL of triethylamine (Mallinckrodt) and 5

92

mL of dry THF were cooled to 0 °C and 0.23 g of distilled methacryloyl chloride (Aldrich) was added

dropwise while stirring. The mixture was stirred for 2 h at 0 °C and then at room temperature for 16 h.

The product was washed with excess distilled water, filtered and dried at room temperature in vacuo.

Successful acylation was confirmed by thin layer chromatography, NMR, and UV-visible

spectroscopies. The structures of the dyes before and after acylation are shown in Figure 6.1.

The two stage PMMA emulsion polymerization reaction was modified from the procedure of

Brnardic[30] and Wolfe and Scopazzi.[10] Table 6.1 shows a typical recipe. In the first stage, 225 mL of

deionized water (Barnstead Nanopure water purification system) and sodium dodecyl sulfate (SDS,

Sigma Chemical) detergent were added to a 500 mL reaction kettle (Ace Glass) equipped with a

mechanical stirrer, reflux condenser, nitrogen inlet and thermometer. The kettle was placed in a

heating mantle which was connected to a temperature controller (Ace Glass, Model 12106). The

stirred mixture was thermostatted at 83 ± 2 °C and bubbled with nitrogen at a low rate for 60 min. The

nitrogen tube was lifted above the reaction mixture and a low rate of gas flow was maintained during

the reaction. Methyl methacrylate (MMA) and divinylbenzene (DVB) (both from Aldrich) were

deinhibited by a column of activated aluminum oxide (Aldrich). A mixture of 12.00 g MMA and 1.12

g DVB was injected over a 30 minute period via a syringe pump. The ionic comonomer sodium 1-

allyloxy-2-hydroxypropane sulfonate (COPS-1) $CH_2=CH-CH_2-O-CH_2-CH(OH)-CH_2-SO_3^- Na^+$ in 40

% aqueous solution was obtained from Rhône-Poulenc and was used as supplied. 0.927 g of COPS-1

diluted with 5 mL water was simultaneously injected by using a separate syringe pump. The sodium

persulfate initiator (Aldrich) was dissolved in water and added after the first stage monomer addition

was complete. When the polymerization began, the temperature rose from 83 °C to 88 °C and dropped

to 83 °C after 15 min. After 40 min of polymerization, a mixture of 35.90 g MMA and 3.35 g DVB
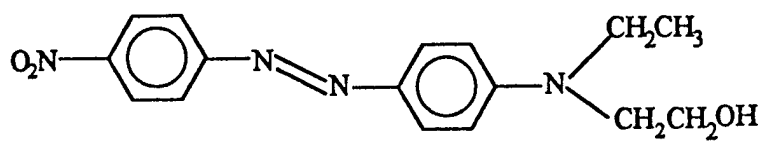
Disperse Red 1
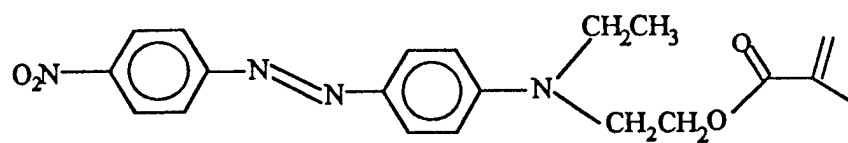
Acylated Disperse Red 1
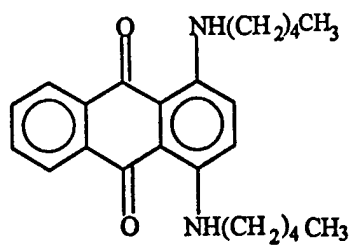
Oil Blue N
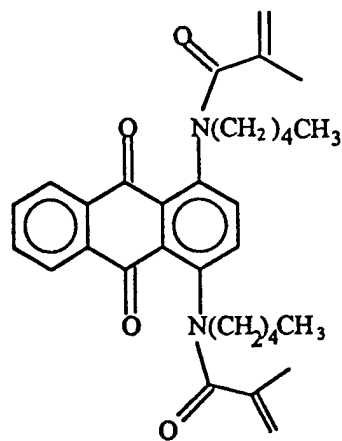
Acylated Oil Blue N

Figure 6.1 Structures of Disperse Red 1 and Oil Blue N before and after methacryloyl chloride acylation.

Table 6.1. Recipe for Emulsion Polymerization of Dyed PMMA Colloid

First stage:

Water	225 mL
MMA	12.00 g
DVB	1.12 g
COPS I	0.927 g / 5 mL water
SDS	0.057 g to 0.150 g
$Na_2S_2O_8$	0.120 g / 3 mL water

Second stage:

MMA	35.90 g
DVB	3.35 g
Acylated Dye	0.075 g to 1.750 g

containing the acylated dye was injected over a period of 60 min. The reaction was continued for 1 h and 50 min to ensure complete reaction of the monomers for a total reaction time of 3.5 h.

The polymerization was followed by removing ca 2 mL of sample from the kettle at different time intervals to determine the percent conversion, particle size and size distribution. Hydroquinone (Fisher Scientific) was used to stop the polymerization. An aliquot was dried in the presence of ca 1 % hydroquinone in an oven at 105 °C for 2 h to determine the degree of conversion.

The reaction product was filtered through glass wool to remove any coagulum. The iridescence of the colloidal crystals could be observed even before purification by shaking the samples with ion exchange resin for 30 min. Typically, the colloidal samples were dialyzed against deionized water for 2 weeks using 50,000 MWCO Spectra / Por 6 dialysis tubing (Fisher Scientific) with the water changed every 24 h. Subsequently, the dialyzed suspension was shaken with Bio-Rad AG 501-X8 mixed bed ion exchange resin for 48 h using a mechanical shaker.

The particle diameter was determined by quasi-elastic light scattering (QELS) and by transmission electron microscopy (Zeiss EM 902A). QELS measurements were performed at 90° scattering angle with a Malvern Zetasizer 4. The cumulant technique was used to determine the light scattering z average mean diameter and the index of polydispersity (Q) of the particle size distribution. In the cumulant analysis, the logarithm of the normalized correlation function is fitted by a second order polynomial after removal of the baseline over time t

$$\log\{(G(t) / <N>^2) - 1\} = L + Mt + Nt^2$$

where G(t) is the second order autocorrelation function, $<N>$ is the baseline intensity and L, M and N are the regression coefficients of the cumulant fit. M gives the z average mean size and Q, defined as

N / M^2, measures the variance of the particle size distribution. Q is zero for monodisperse spheres and is typically 0.02 to 0.05 for latexes with narrow distributions.

After vigorous cleaning, the surface charge density of the dyed spheres was determined by conductometric titration with 0.01 N sodium hydroxide solution. 12 g of the latex sample containing ca 6 % solids was titrated and the specific conductivity was measured by a conductance meter (YSI model 35). The shapes of the titration curves are typical of those found in titrations of a strong acid with a strong base. The molar absorptivites were determined by dissolving the dyes in spectrophotometric grade acetonitrile (Mallinckrodt) to a concentration of 0.31 mM and the transmission spectra obtained with a Perkin-Elmer Lambda 9 UV-Visible-Near IR spectrophotometer.

The dye concentration in the latex was determined by UV-visible spectroscopy. To minimize the scattering from the colloidal particles, the particles were refractive index matched by adding methyl phenyl sulfoxide (MPSO) (Aldrich) which is a high refractive index (n = 1.58), water-miscible solvent. In a typical procedure, 0.10 g dyed latex was diluted with 0.58 g water and 2.00 g MPSO to give a refractive index of 1.51. The refractive index of the suspension was measured by an Abbè refractometer (Bausch and Lomb) thermostatted at 23 °C.

We used a procedure modified from that of Asher et al.[31] to polymerize the dyed spheres within polyacrylamide hydrogels. In a typical preparation, 93.6 mg acrylamide monomer, 14.6 mg N,N'-methylenebisacrylamide crosslinker (both Fluka electrophoresis grade), 20.0 mg N-vinyl-2- pyrrolidone comonomer (Aldrich) and 10.0 mg of a solution of 50 % 2,2-diethoxyacetophenone photoinitiator (Aldrich) and 50 % dimethyl sulfoxide (Fisher Scientific) by volume were mixed with 1.5 mL of dyed PMMA colloid and shaken with ion exchange resin until the iridescence returned. The mixture was degassed under vacuum, injected slowly into quartz cells and polymerized under a 365 nm UV lamp

(Blak Ray B-100Y) for 4 h. The strength and porosity of the hydrogel films were controlled by varying the N,N'-methylenebisacrylamide and N-vinyl-2- pyrrolidone concentrations.

6.4 Results and Discussion

Acylation of Dyes.

Since no oil-soluble, non-fluorescent dyes with polymerizable vinyl groups are commercially available, we introduce vinyl groups into the dyes by acylation using methacryloyl chloride. The azo dye Disperse Red 1 was chosen for acylation because it absorbs in the yellow/orange/red areas. The UV-visible spectra of Disperse Red 1 in acetonitrile before and after acylation (Figure 6.2) show that acylation of the terminal OH group results in blue shifts of the 485 nm and 287 nm bands to 474 nm and 283 nm, respectively. The molar absorptivities remained essentially identical ($\varepsilon = 3.4 \times 10^4 \, M^{-1} \, cm^{-1}$ at 474 nm). NMR spectra of the acylated Disperse Red 1 showed the presence of the C=C double bond from methacryloyl chloride and aromatic rings from the dye.

We have also utilized the 1,4-disubstituted anthraquinone Oil Blue N dye which absorbs in the 600 to 650 nm region and is compatible with acrylic polymers.[32] The absorption spectrum of Oil Blue N shows two peaks of similar intensities at 640 nm and 594 nm which may be due to an underlying Franck-Condon progression. Strong absorption also occurs for a UV band at <u>ca</u> 260 nm. Acylation of the two secondary amino groups by methacryloyl chloride results in a blue shift of the visible bands to a single broad peak with a maximum at 515 nm. The absorptivity decreases by 60 % while the absorbance of the UV bands increases (Figure 6.3). This type of wavelength shift has been reported for the acylation of substituted anthraquinone dyes with methacryloyl chloride.[33] It may result from a decrease in the conjugation of the anthraquinone ring by reduction of the two carbonyl groups to form
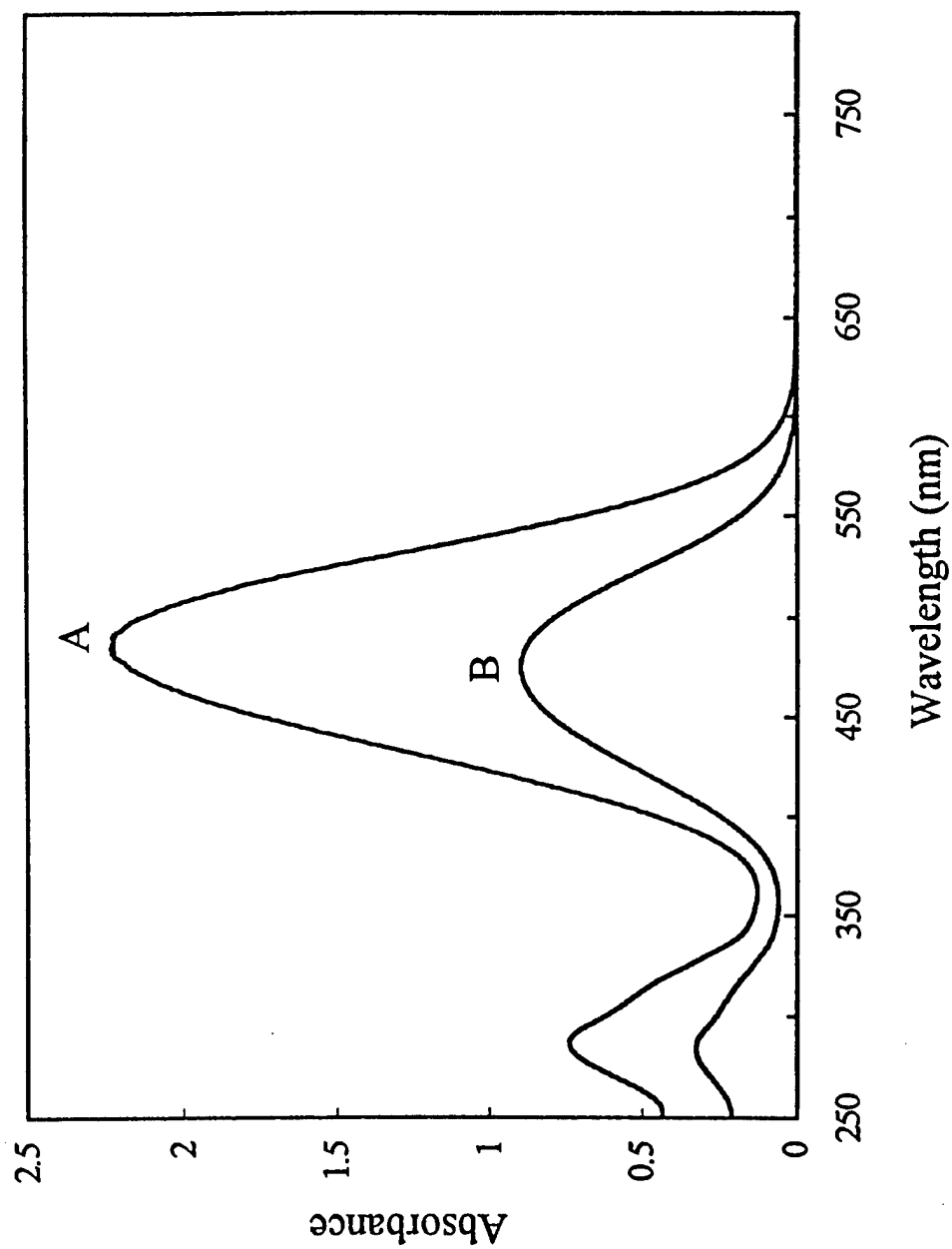
Figure 6.2 Absorption spectra of 0.31 mM Disperse Red 1 in acetonitrile; (A) before and (B) after acylation with methacryloyl achloride. Pathlength = 0.2 cm.

99

Figure 6.3 Absorption spectra of 0.31 mM Oil Blue N in acetonitrile; (A) before and (B) after acylation with methacryloyl chloride. Pathlength = 0.2 cm.

Table 6.2. Molar Absorptivities of Dyes before and after Acylation[a]

Dye	λ_{max} (nm)	ε (M^{-1} cm^{-1})
Disperse Red 1		
before	485	3.6×10^4
	287	1.2×10^4
after	475	3.4×10^4
	283	1.3×10^4
Oil Blue N		
before	640	1.6×10^4
	594	1.4×10^4
	256	2.8×10^4
after	515	0.7×10^4
	318	0.9×10^4
	250	4.2×10^4

[a] λ_{max} = absorption wavelength maximum; ε = molar absorptivity.

hydroxy groups. Table 6.2 shows the absorption maxima and molar absorptivities of the two dyes before and after acylation.

Dyed PMMA Latexes.

The first stage of the emulsion polymerization utilized 25 % of the monomers and the ionic comonomer COPS-1 to generate the seed particles, while in the second stage, the remaining 75 % of the monomers with the dissolved dye was continuously injected into the kettle to permit the particles to grow to the desired size. With this semi-continuous emulsion polymerization technique, we could synthesize dyed monodisperse PMMA particles with any size between 60 and 210 nm by varying the SDS concentration.

The time course of polymerization was followed for the reaction using 0.060 g SDS and 0.105 g acylated Disperse Red 1. For the first stage polymerization the conversion was 72 % of the amount added and the size was 122 nm within 10 min of reaction, showing that the reaction is fast. The conversion reached 91 % and the size was 129 nm at the end of the first stage in 40 min. The full conversion-time curve and the size-time curve including both stages are shown in Figures 6.4 and 6.5, respectively where the conversion percentage was normalized to the total amount of monomer added. The size at the end of the reaction was 205 nm at 99 % conversion. It is interesting to note the similar shapes of the two curves.

The polydispersity index by QELS at different time intervals ranged from 0.02 to 0.07. This indicates that the particles were monodisperse throughout the reaction. The particle concentration (n_p) in the suspensions was calculated from the % solids and the particle diameter (d)

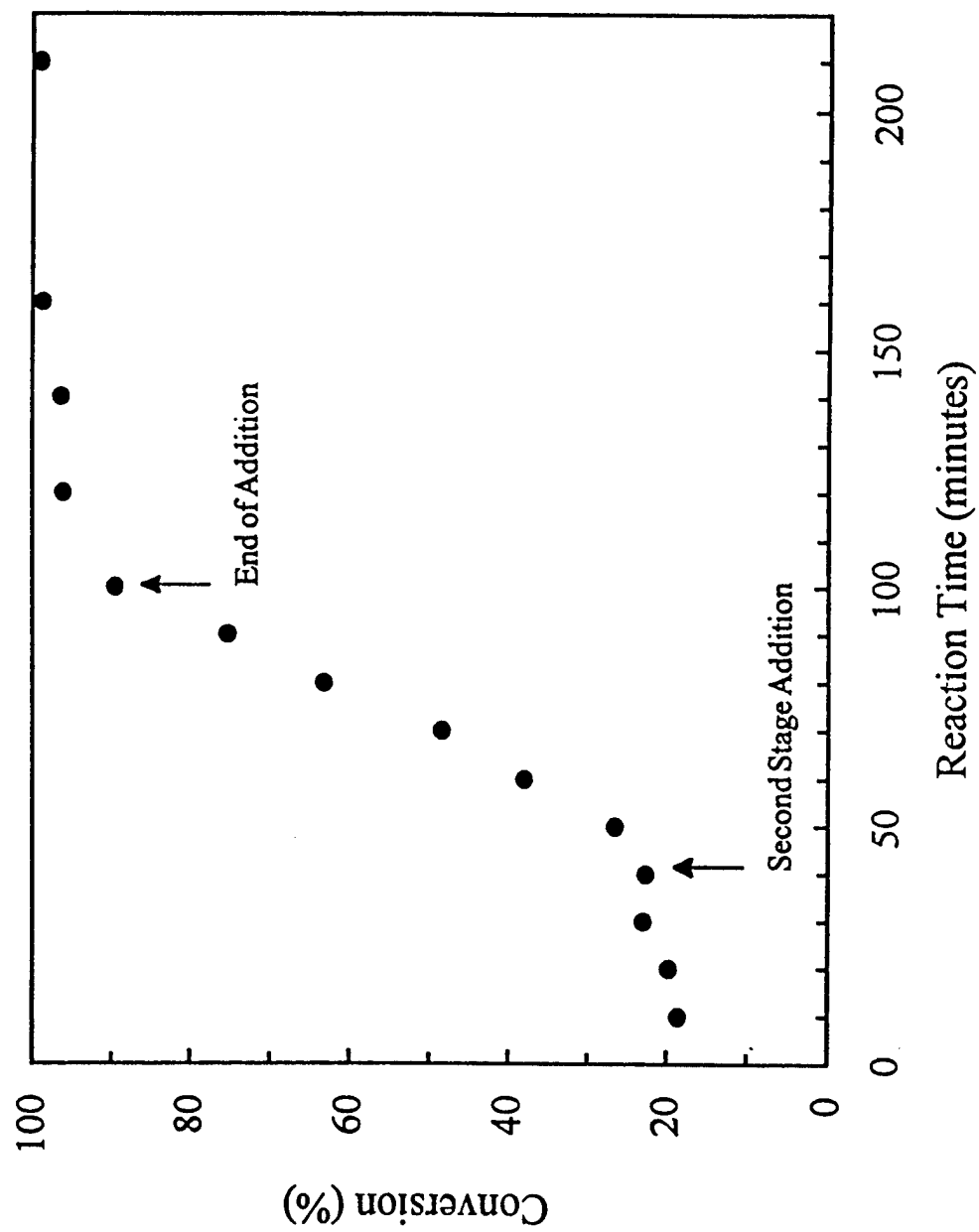$$n_p = (\% \text{ solids} / 100) (\text{latex density}) / (\pi d^3 \rho / 6)$$

Figure 6.4 Conversion-time curve of emulsion polymerization of MMA with Disperse Red 1.
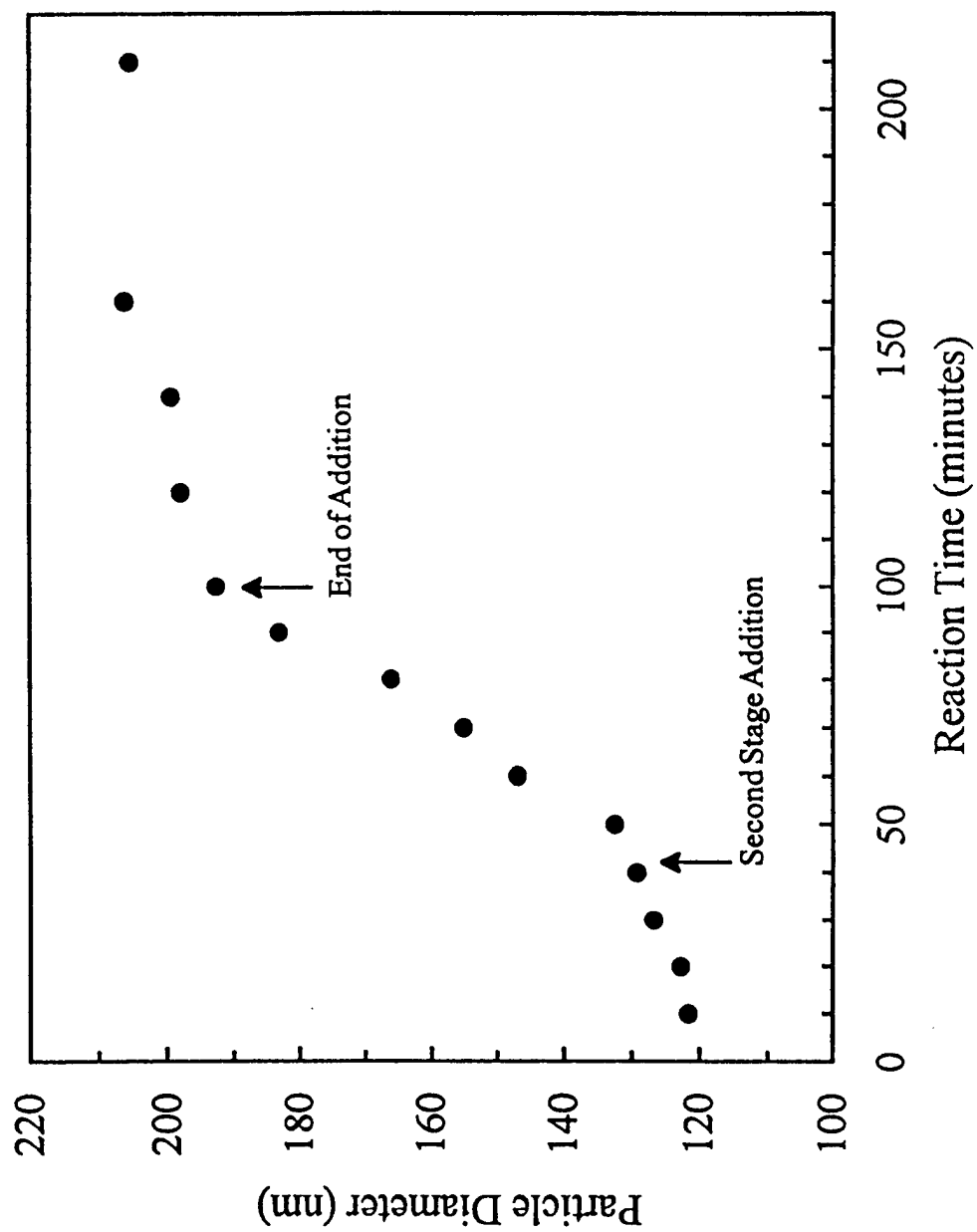
Figure 6.5 Size-time curve of emulsion polymerization of MMA with Disperse Red 1.

where ρ is the density of PMMA and is 1.118 g/mL. The density of the crosslinked latex was determined to be 1.15 g/mL. The average number of particles was $3.8 \pm 0.3 \times 10^{13}$ per mL and remained constant throughout the rest of the reaction. Apparently nucleation was complete within the first 10 min and few new nuclei formed in the second stage.

Figure 6.6 shows a transmission electron micrograph of PMMA with Disperse Red 1 covalently attached to it. The particles were spherical and monodisperse with an average size of 92 ± 2 nm which is significantly smaller than the value of 123 nm as measured by QELS. This smaller size is probably due to the partial shrinkage of the particles in the electron beam by the free radical chain depolymerization of PMMA.[9] Tables 6.3 and 6.4 list the properties of PMMA-Disperse Red 1 and PMMA-Oil Blue N colloids, respectively. The particle size ranges between 100 to 200 nm with low polydispersities. The particle number density is ca 10^{13} per mL. The surface charges of the colloids are derived from both the sulfate groups from the initiator and sulfonate groups from the COPS-1. The charge density of the colloids is on the order of 1.0 $\mu C/cm^2$ which is about 8000 charges per particle for a 190 nm particle size. The charge densities are comparable to those of PMMA colloids prepared with the same recipe without dye.

The dye concentration in the latex was determined by absorption measurements of the refractive index matched spheres. The refractive index of the PMMA spheres with 9.3 wt % DVB crosslinker (n =1.57) is 1.51 which is higher than the value of 1.49 for pure PMMA. At the index matched point of n = 1.51, no scattering from the colloid occurs and the absorbance measured is only due to the dye absorption. Here, we assume that the molar absorptivity of the dye bound to the PMMA particles is identical to the acylated dye. The dye concentrations range from 0.4 mM to 6.5
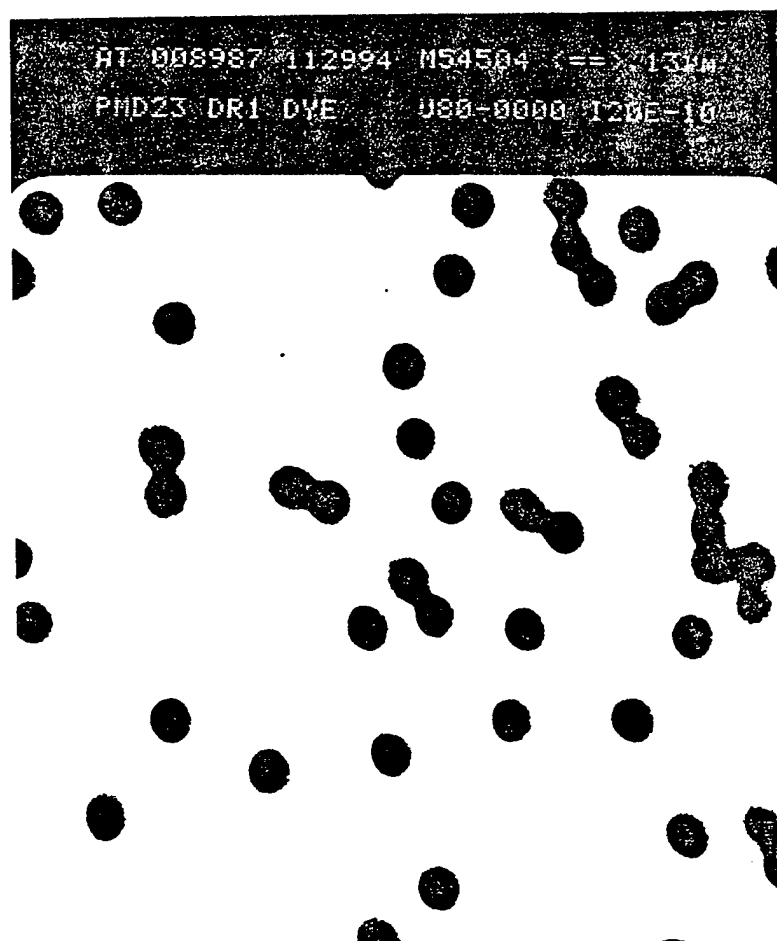
Figure 6.6 Transmission electron micrograph of PMMA colloid with Disperse Red 1.

Table 6.3. Properties of PMMA Colloid with Disperse Red 1[a]

% solids	d (nm)	Q	n_p (mL^{-1})	S (μC/cm^2)	c (mM)	σ_p (cm^2/part.)	σ_p (cm^2/part.)
15.9	123	0.043	16.0 x 10^{13}	0.9	2.2	8.3 x 10^{-13}	1.2 x 10^{-10}
10.2	141	0.043	6.8 x 10^{13}	1.2	6.5	58.0 x 10^{-13}	1.6 x 10^{-10}
17.6	186	0.029	5.1 x 10^{13}	1.0	0.4	7.1 x 10^{-13}	2.7 x 10^{-10}
17.0	205	0.032	3.7 x 10^{13}	0.9	1.0	4.0 x 10^{-13}	3.3 x 10^{-10}

[a] d = z Average mean diameter ; Q = polydispersity index; n_p = number density of particles; S = charge density; c = dye concentration in colloid; σ_a = particle absorption cross section; σ_p = particle cross sectional area.

Table 6.4. Properties of PMMA Colloid with Oil Blue N[a]

% solids	d (nm)	Q	n_p (mL^{-1})	S (μC/cm^2)	c (mM)	σ_a (cm^2/part.)	σ_p (cm^2/part.)
10.7	131	0.014	8.9×10^{13}	1.1	2.3	4.2×10^{-13}	1.3×10^{-10}
18.5	194	0.057	4.8×10^{13}	1.0	0.7	2.5×10^{-13}	3.0×10^{-10}

[a] d = z Average mean diameter; Q = polydispersity index; n_p = number density of particles; S = charge density; c = dye concentration in colloid; σ_a = particle absorption cross section; σ_p = particle cross sectional area.

mM or 0.071 to 1.2 wt % of the colloids (Tables 6.3 and 6.4). The absorption cross section (σ_a) of

the dyed particles at the refractive index matched point was calculated using the equation

$$\sigma_a = A / (0.434\, n_p\, b)$$

where A is the absorbance and b is the pathlength. The absorption cross sections of the dyed colloidal

particles are all on the order of 10^{-13} cm^2. The actual cross section of a PMMA sphere without dye is

of the order of 10^{-10} cm^2. Thus the absorption cross section is ca 0.1 % of the physical area of a

PMMA particle.

To prove that the dye was covalently attached to the PMMA, we tried to extract the dye from

the colloid. The PMMA-Disperse Red 1 colloid was dried at 105 °C for 2 h, cooled and extracted with

different organic solvents. For ethylene glycol the solvent remained colorless and the colloid red-

colored. There was a slight extraction by dimethyl sulfoxide and MPSO. This could be due to the

presence of traces of unreacted dye. Similar results were observed for PMMA-Oil Blue N spheres. As

a control we also added Disperse Red 1 dye to the PMMA colloids. The dye partitions into the

PMMA spheres, but is easily extracted with organic solvents such as ethylene glycol or benzyl alcohol.

Hydrogel Crystalline Colloidal Arrays of Dyed PMMA.

After removal of ionic impurities these highly charged dyed monodisperse PMMA spheres

spontaneously self-assemble due to electrostatic interactions into BCC or FCC structures called

crystalline colloidal arrays (CCA). Diffraction from these well-ordered CCA almost follows

Bragg's law[16]

$$\lambda_0 = 2nd \sin \theta$$

where λ_0 is the wavelength of the light in vacuum, n is the refractive index of the system, d is the

plane spacing, and θ is the Bragg angle. In general, the extinction (E = -log (transmission)) of
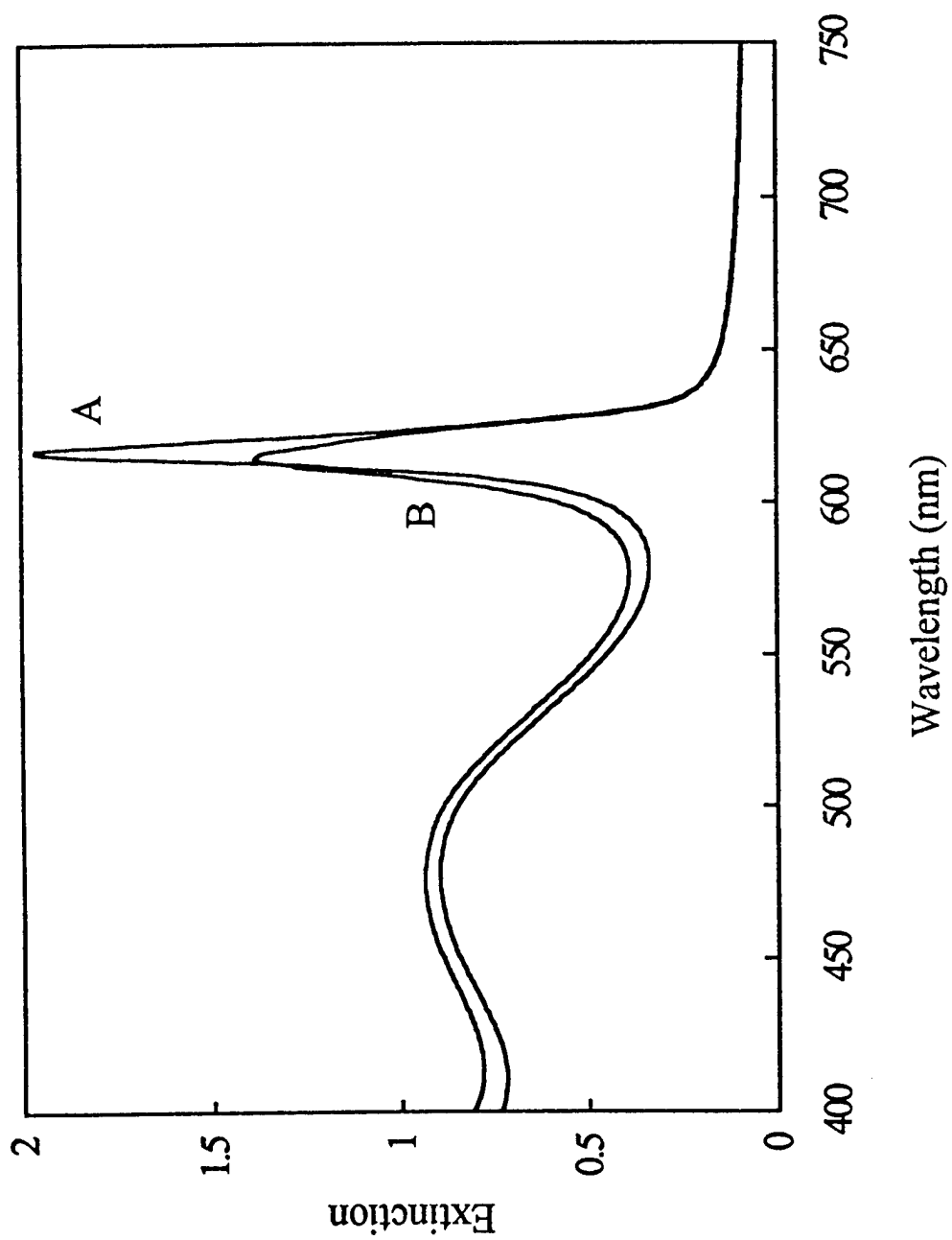
Figure 6.7 UV-visible spectra of (A) a 0.22 mm thick liquid CCA of PMMA-Disperse Red 1 before gelation and (B) the polymerized CCA.

110

0.22 mm thick CCA ranges from 1 to above 5 depending on the CCA ordering, on the colloid size and the refractive index mismatch between the colloidal spheres and the medium.

Figure 6.7A shows the extinction spectrum of a CCA prepared from the 123 nm PMMA-colloids containing Disperse Red 1. The CCA medium consists of a mainly aqueous medium which contains polymerizable monomers and the photoinitiator. The peak at 617 nm is due to the CCA Bragg diffraction while the broad peak at 475 nm is due to dye absorption. After illumination with UV light, a hydrogel forms to lock in the CCA particle ordering.[34,35] Figure 6.7B shows the extinction spectrum of this polymerized CCA. The extinction of the diffracting peak decreased from 1.9 to 1.4 after gelation. There was a slight peak shift to 614 nm. The broad dye absorption peak at 478 nm was not affected by gelation. The similarities of the two diffraction peaks indicates that the lattice was little disturbed upon polymerization.

The medium of the CCA hydrogel can be exchanged by adding other solvents such as MPSO to change the refractive index mismatch between the spheres and the medium. This will dramatically alter the CCA diffraction intensity since it depends linearly upon the refractive index mismatch between the spheres and the medium

$$E \propto |m^2 - 1|$$

where $m = n_s / n_m$; n_s and n_m are the refractive indices of the spheres and the medium, respectively.[36] Figure 6.8 shows the spectra of a 0.44 mm thick hydrogel CCA of 184 nm PMMA colloids containing covalently linked Oil Blue N with a medium containing various concentrations of water and MPSO. For pure water, the refractive index mismatch is $\Delta n \sim 0.28$, and the extinction of the diffraction peak at 640 nm is above 4 ($\Delta n \sim 0.04$, Figure 6.8A). There is a large decrease in extinction to 0.76 when the medium refractive index increases to 1.475 (Figure 6.8B). The peak also blue shifts to 543 nm due to
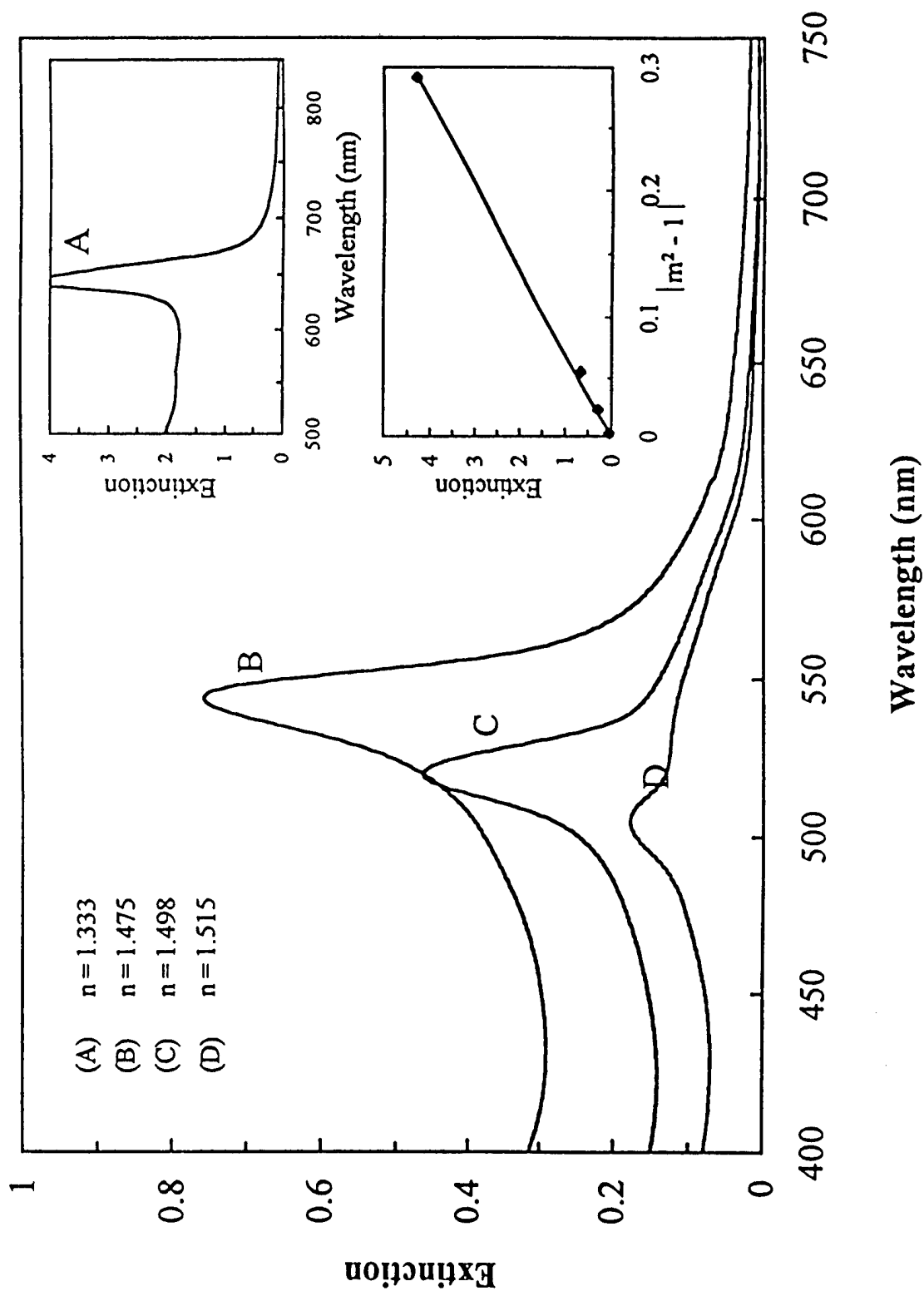
Figure 6.8 UV-visible spectra of 0.44 mm thick polymerized CCA of PMMA-Oil Blue N in water/MPSO solutions of different refractive indices; (A) 0 wt. % MPSO, (B) 62 wt % MPSO, (C) 71 wt % MPSO and (D) 76 wt % MPSO.

the shrinkage of the hydrogel with the addition of MPSO. When the real part of the array refractive index is approximately matched with the medium at n = 1.515, the extinction maximum is 0.18 and the peak position shifts to 508 nm (Figure 6.8D). The underlying broad peak, which is most evident in Figure 6.8D, results from the absorption of acylated Oil Blue N which has a maximum at 515 nm. The refractive index matching also results in a significant decrease in the background diffuse scattering of the CCA and the hydrogel matrix. The inset in Figure 6.8 demonstrates that the diffraction extinction is linear with $|m^2 - 1|$.

Alterations of the diffracted wavelength results from a change in the wavelength of light in the medium which should shift the observed peak to the red; for λ_0 / n to stay constant when n increases, λ_0 must also increase. The observed diffracted wavelength blue shift results from a gel shrinkage due to the changing properties of the medium. In the case here the lattice spacing contracts. This turns out to be a useful independent method for varying the diffraction wavelength. Unfortunately for these gels some disordering of the lattice begins to become evident as the refractive index matching condition begins to be met. This decreases the Bragg efficiency somewhat from that expected. This becomes serious at higher refractive indices where the medium refractive index becomes greater than that of the colloids.

The hydrogel array appears to be in either a FCC lattice or a mixed FCC BCC array, or in a random stacked hexagonal array. The quality of the Kossel rings makes it difficult to determine the crystal structure in the refractive index matched gels.

6.5 Conclusions

We have created an ordered array of absorbers locked in a hydrogel matrix. The absorbers are contained in ca 150 nm colloids arrayed in a lattice. The absorbers are relatively dilute within the colloidal particles to give each colloidal particle a cross section of 10^{-13} cm^2, which is almost 1000-fold smaller than that of the colloidal particle cross sectional area. This system may be useful for nonlinear optical switching and limiting applications.

6.6 References

(1) *Future Directions in Polymer Colloids*, El-Aasser, M. S.; Fitch, R. M., Eds.; Martinus Nijhoff: Dordrecht, 1987.

(2) Bhattacharyya, B. R.; Halpern, B. D. *Polymer News* **1977**, *4*, 107.

(3) *Scientific Methods for the Study of Polymer Colloids and Their Applications*, Candau, F.; Ottewill, R. H., Eds.; Kluwer Academic: Dordrecht, 1990.

(4) Kamel, A. A.; El-Aasser; Vanderhoff, J. W. *J. Dispersion Sci. Tech.* **1981** *2*, 183.

(5) Tsaur, S. L.; Fitch, R. M. *J. Colloid Interface Sci.* **1987** *115*, 450.

(6) Kim, J. H.; Chainey, M.; El-Aasser, M. S.; Vanderhoff, J. W. *J. Polym. Sci. Polym. Chem. Ed.* **1989** *27*, 3187.

(7) Sunkara, H. B.; Jethmalani, J. M.; Ford, W. T. *J. Polym. Sci. Polym. Chem. Ed.* **1994** *32*, 1431.

(8) Ono, H; Saeki, H. *Colloid Polym. Sci.* **1975** *253*, 744.

(9) Fitch, R. M.; Tsai, C. H. In *Polymer Colloids*, Fitch, R. M., Ed.; Plenum: New York, 1975; p 73.

(10) Wolfe, M. S.; Scopazzi, C. *J. Colloid Interface Sci.* **1989**, *133*, 265.

(11) Stöber, W.; Fink, A.; Bohn, E. *J. Colloid Interface Sci.* **1968**, *26*, 62.

(12a) Chang, S. Y.; Liu, L.; Asher, S. A. *J. Am. Chem. Soc.* **1994**, *116*, 6739.

(12b) Chang, S. Y.; Liu, L.; Asher, S. A. *J. Am. Chem. Soc.* **1994**, *116*, 6745.

(13) Matijevic, E. *Pure and Appl. Chem.* **1988**, *60*, 1479.

(14) Carlson, R. J.; Asher, S. A. *Appl. Spectroscopy* **1984**, *38*, 297.

(15) Flaugh, P. L.; O'Donnell; Asher, S. A. *Appl. Spectroscopy* **1984**, *38*, 847.

(16) Rundquist, P. A.; Photinos, P.; Jagannathan, S.; Asher, S. A. *J. Chem. Phys.* **1989**, *91*, 4932.

(17) Kesavamoorthy, R.; Jagannathan, S.; Rundquist, P. A.; Asher, S. A. *J. Chem. Phys.* **1991**, *94*, 5172.

(18) Kesavamoorthy, R.; Tandon, S.; Xu, S.; Jagannathan, S.; Asher, S. A. *J. Colloid Interface Sci.* **1992**, *153*, 188.

(19) Asher, S. A. U. S. Patent No. 4 627 689 and 4 632 517, 1986.

(20) Asher, S. A.; Flaugh, P. L.; Washinger, G. *Spectroscopy* **1986**, *1*, 26.

(21) Kesavamoorthy, R.; Super, M. S.; Asher, S. A. *J. Appl. Phys.* **1992**, *71*, 1116.

(22) Asher, S. A.; Kesavamoorthy, R.; Jagannathan, S.; Rundquist, P. In *SPIE Nonlinear Optics III*; Fisher, R. A.; Reintjes, J. F., Eds.; International Society for Optical Engineering: Bellingham, Washington, 1992; pp 238-242.

(23) Chang, T. Y. *Optical Engineering* **1981**, *20*, 220.

(24) Rundquist, P. A.; Jagannathan, S.; Kesavamoorthy, R; Brnardic, C.; Xu, S.; Asher, S. A. *J. Chem. Phys.* **1991**, *94*, 711.

(25) Rundquist, P. A.; Kesavamoorthy, R.; Jagannathan, S.; Asher, S. A. *J. Chem. Phys.* **1991**, *95*, 1249.

(26) Rundquist, P. A.; Kesavamoorthy, R.; Jagannathan, S.; Asher, S. A. *J. Chem. Phys.* **1991**, *95*, 8546.

(27) Sosnowski, S.; Feng, J.; Winnik, M. A. *J. Polym. Sci. Polym. Chem. Ed.* **1994**, *32*, 1497.

(28) Peterson, J. I. U.S. Patent 4 194 877, 1980.

(29) Loucif-Saïbi, R.; Nakatani, K.; Delaire, J. A.; Dumont, M.; Sekkat, Z. *Chem. Mat.* **1993**, *5*, 229.

(30) Brnardic, C. M.S. Thesis, University of Pittsburgh, 1992.

(31) Asher, S. A.; Holtz, J.; Liu, L.; Wu, Z. *J. Am. Chem. Soc.* **1994**, *116*, 4997.

(32) Gordon, P. F.; Gregory, P. *Organic Chemistry in Colour*; Springer-Verlag: Berlin, 1985.

(33) Vlyazlo, R. I.; Voloshin, G. A.; Grivnak, L. M.; Boldyrev, B. G.; Kozlov, L. V.; Zavalishchina, L. M. *Zh. Prikl. Khim. (Leningrad)* **1975**, *48*, 152.

(34) Haacke, G.; Panzer, H. P.; Magliocco, L. G.; Asher, S. A. U.S. Patent 5 266 238, 1993.

(35) Asher, S.A.; Jagannathan, S. U.S. Patent 5 281 370, 1994.

(36) Hiltner, P. A.; Papir, Y. S.; Krieger, I. M. *J. Phys. Chem.* **1971**, *75*, 1881.

7.0 Conclusion

We have examined the self assembly process in CCAs, and demonstrated that self-assembling colloidal particles can be fabricated from a variety of materials. The physical, and especially the optical, properties of these colloidal particles can be precisely controlled. We are able to control the morphology of the CdS / silica nanocomposite particles and produce a wide variety of novel colloidal materials. By etching away the CdS, we were able to create silica with complex, tailored pore structure. We will to use this material to fabricate non-linear optical limiters, where the silica is index matched to the suspending medium. This system will pass low intensity visible light; however, high intensity light will interact with the CdS quantum dots, causing the array to "pop up" and diffract the incident light. As an offshoot of this work, we have created a novel material consisting of porous silica colloids with tailored voids. This material may be useful as a new, high surface area, catalytic support.

We also developed a method to incorporate CCAs of any monodisperse, charged colloidal particles into a hydrogel matrix (PCCA). The resulting PCCA is impervious to ionic impurities and thermal or physical shocks, which normally disorder the liquid CCA. The PCCA is a superior mesoscopically periodic material for optical device fabrication due to its stability and ease of fabrication.

We are also able to fabricate highly charged PMMA particles that self-assemble into CCAs. These materials may have covalently attached dyes, and be useful for non-linear optical limiters using the large thermal n_2 density non-linearities described previously by Professor Asher's group. These self assembling colloidal systems are a unique class of materials with mesoscale periodicities that can be tailored for numerous applications.

117